# III-V-based Low-dimensional Structures

DSc Theses of HAS

**Ákos Nemcsics**

Hungarian Academy of Sciences
Research Institute for Technical Physics and Materials Science
and
Óbuda University, Kálmán Kandó Faculty of Electrical Engineering
Institute for Microelectronics and Technology

Budapest, 2011

# Contents

**Bibliography**

**Closing remarks**

# 1. Chapter

# Introduction

The application of low-dimensional (2D, 1D, 0D) structures is revolutionized all branches of technology including electronics [1, 2, 3, 4]. A structure is called low dimensional, when at least one of its dimensions fall into the nanometer range and appears to have quantum confinement (Fig. 1.1). The applications of these structures are numerous [5, 6, 7, 8].

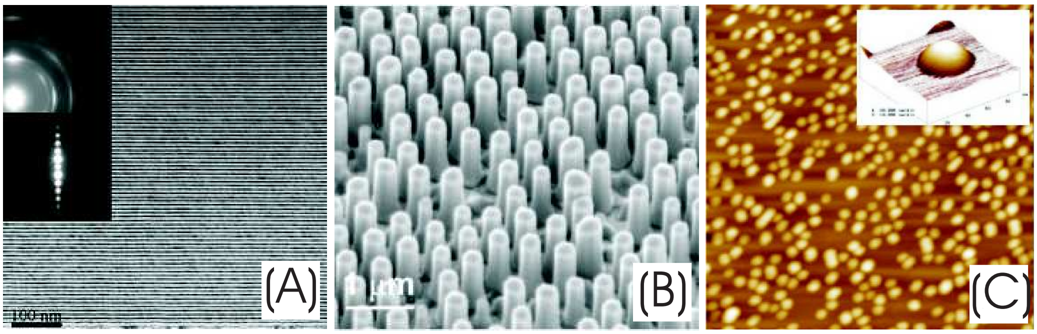

1.1. Fig. Three different low-dimensional semiconductor structures: (A) TEM (transmission electron microscopy) image of a super lattice structure (or quantum wells); (B) SEM (scanning electron microscopy) image of nano-whiskers (or nano-wires); (C) AFM (atomic force microscopy) image of nano-dots (or quantum dots).

These applications can be demonstrated for instance by solar cells (see the references e.g. in [9, 10, 11] and Fig. 1.2). The efficiency of commercial solar cells ranges between 5 and 15%. A simple pn-junction GaAs solar cell - which material is very suitable for solar energy conversion - has an efficiency of less than 30%. We can fabricate an almost continuously varying band gap solar cell with the help of quantum mechanical effect (this is called band gap tailoring in the literature). Our aim is to prepare quantum wells (QWs) with various widths (2D). The efficiency of a multi quantum well GaAs-based solar cell can exceed 40% (Fig. 1.2). By embedding quantum dots (QDs) in the solar cell material (0D), we produce a so-called intermediate band inside of the band gap. With the help of suitably chosen intermediate band, solar cells can achieves efficiency over 60% (Fig. 1.2). Metal induced nano-wires (1D) can also be grown by MBE, where the structure efficiency can improve by many orders of magnitude (Fig. 1.2). The solar cells are typical samples for the application of low-dimensional structures. These nano-structures can revolutionize electronics and computing technology (quantum computing) as well [12, 13, 14].

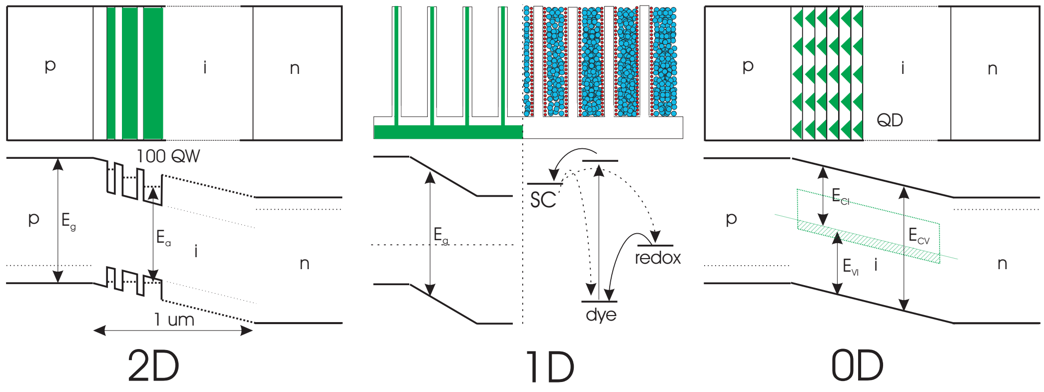

1.2. Fig. Enhancement of solar cell efficiency with the help of different low-dimensional structures. (2D): Solar cells with super lattices are the so called multi-quantum well solar cells. (1D): left part: solar cells with coaxial nano-wires; right part: dye sensitized electrochemical solar cell with bulk junction. (0D): Solar cells with quantum dots are the so called intermediate-band solar cells.

Here, we deal with growth kinetics and properties of the low-dimensional nano-structures. The technology used for the growth determines the size, shape and the elementary distribution of the developing structures. These physical parameters are very important in both theoretical and practical point of view. This work is dealing with III-V-based low-dimensional structures, grown by molecular beam epitaxy (MBE). MBE is a top technology, where different structures can be grown under controlled conditions and in-situ observation. In this work, we investigate structures in growth made of GaAs and related semiconductor materials. The kinetics of the growth is investigated in-situ by using Reflection High-Energy Electron Diffraction (RHEED). The measuring method of RHEED is also the subject of investigation, because some of the results produced by it are not quite clear and needs interpretation. The developed structures were investigated by using Atomic Force Microscopy (AFM), Transmission Electron Microscopy (TEM) and Photo Luminescence (PL) spectroscopy and the conclusions were drawn from these results.

The low-dimensional nano-structures, mentioned above, are produced by the MBE technology with high controllability. The growth is carried out under ultra high vacuum (UHV) and the growth process is monitored by using in-situ RHEED. RHEED is a widely used monitoring technique in MBE growth. The quality and reconstruction of the grown surface can be monitored by the RHEED technique. The intensity of the RHEED pattern oscillates under these conditions during the growth process. In order to produce layers of atomic dimensions and nano-structures of accurate dimensions and specific shapes (low dimension structures) we have to know the growth kinetics and the ongoing, exact physical process of the monitoring RHEED. In spite of being able to produce perfect structures there are some unexplained phenomena associated with the growth kinetics and the interpretation of the RHEED results. The III-V materials subjected to the so called homolog epitaxy which provide some possibilities in the device technology and also for basic research. During the growth, the band gap can be varied with the help of the composition of these III-V compound materials. The lattice constant can be also variable. The different lattice constants can result in strained layer in the layer structure and misfit the epitaxial growth. The RHEED intensity oscillations can also be used to determine accurately the threshold layer thickness at two-dimensional growth. With the use of lattice strain relaxation, Quantum Dots (QDs) can be grown. These nano-structures are called strain induced QDs. The materials, which can be used for growing QD-s in this way, are limited by their lattice parameters. An alternative way of growing QD-s is droplet epitaxy. In this case the lattice constant is not the limiting factor and GaAs QD can be grown on GaAlAs. By using this method not only QD-s but also Quantum Rings (QR) and other nano-structures can be grown. There are a number of unknown factors in the growth of these structures.

In the first part of this work, we give a short theoretical and technological introduction of the III-V-based nano-structures. In section 2, we are dealing with the scientific and technological background of low-dimensional structures. We show, how can we drastically increase the yield of an electronic device with the use of nano-structures. Here, we give an overview of the bulk- and surface properties of the III-V compounds. In this section, we are deling with the MBE, the equipment, and the growth kinetics. In an extra subsection, we are deling with RHEED. The RHEED has fundamentally importance in the investigation of the growth kinetics. This technique is a versatile tool for in-situ monitoring, in spite of the fact that we do not know some of the details of its nature. A number of the properties and behaviour of patterns of the oscillations are not yet fully understood. Here we give explanation for some particular behaviour of the RHEED during the growth of GaAs/GaAs, GaAs/InGaAs and GaAs/LT-GaAs. After that, we are dealing with different low-dimensional structures. Section 3 deals with 2D structures, section 4 with 1D structures and section 5 with 0D structures. In this last section, we are dealing with droplet epitaxy and will show some new development in this field, which will probably revolutionise the semiconductor device technology.

# 2. Chapter

# Scientific and Technological Background

## 2.1. Physics of Low-dimensional structures

The nano-technology is dealing with the manipulation of materials in few atomic and molecular scale, where the constructed structure sized - at least in one dimension - is between one and one-hundred nanometer. This technology allows to fabricate novel materials and electronic devices, where, the quantum mechanical effects (e.g. quantum confinement) are very significant. The most conventional device fabrication is the so called top-down approach. Here, smaller device is created from the larger material block with, material removal. These material removals should be different depending on the object. This removal can be mechanical like carving, milling, etching etc. In microelectronics, photolithography is a well known method to fabricate the required structure. In this technology, we can mark parts of the surface with a mask. We can also remove selectively parts from the thin film or from the substrate material. This method is widely used in the silicon technology to fabricate devices like integrated circuits. Another fabrication method, which matches nano-technology, is the so called bottom-up approach. Here, we arrange large number of smaller components into very complex assemblies, where the typical technology is epitaxial growth. We can grow in the bottom-up way quantum wells, quantum wires and quantum dots. Here, we exploit the self-organizing or self-assembling properties, which is - under special conditions - inherent to the materia. The self-assembly is a process, where structures form without external influence. This is the most typical example of self-assembling system, from the physics of non-equilibrium processes, like the molecular epitaxial growth, detailed latter.

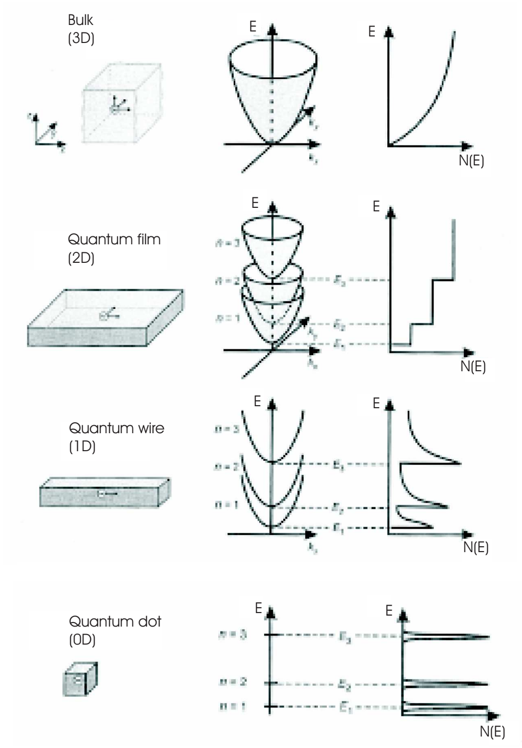

2.1. Fig. The bulk and three different low-dimensional semiconductor structures. Left part: The geometry; Middle part: The dispersion relation; Right part: Distribution of the density of states.

The quantum wells, quantum wires and quantum dots are two, one and zero dimensional structures, respectively. These low-dimensional structures have such properties, that carry novel possibilities in science and technology. That way, we can fabricate entirely new electronic and optoelectronic devices. Quantum confinement originate in structure, which confine electrons to regions comparable to their de Broglie wavelength. In free space, the electron can be move in all of the three directions of space. An unconfined electron (can move x-, y-, z-directions) is described by the Schrödinger equation. Where the solution of this equation is $\varphi_k(r) = [1/(2\pi)^3]e^{ikr}$. Where $k$ is the wavevector. The relative energy is as follows: $E = h^2k^2/2m =$

$h^2/2m(k_x^2 + k_y^2 + k_z^2)$.

The density state of a three-dimensional free electron gas calculated as follows $g(E) = 1/2\pi^2(2m/h^2)^{3/2}E^{1/2}$.

The diagram is shown in Fig. 2.1. When confinement occurs in one direction in space, and the restriction on the motion of the electron is in the z-direction. then the free motion is possible only in x- or y-direction, when it is called two-dimensional (2D) structure or 2D electron gas. The energy of 2D electron gas is $E = h^2k^2/2m = h^2/2m(k_x^2 + k_y^2)$ From this formula, the density state is constant, therefore independent of energy, $g(E) = m/\pi h^2$.

This is the description of the strictly a 2D structure. The confinement in z-direction tends to be zero. In practice, we regard a system quasi 2D, where the restriction is finite but small, (see Fig. 2.1). When the confinement is in two directions (y and z), with the free motion in x-direction then the structure is one-dimensional (1D) structure or 1D electron gas. The energy of the 1D motion electron is given below $E = h^2k^2/2m = h^2/2m(k_x^2)$ Here, the expression of the density state from this calculation given as $g(E) = 1/\pi(2m/h^2)^{1/2}1/E^{1/2}$.

This density function in a quasi 1D case is shown in Fig. 2.1. When the confinement is in x-, y-, and z-directions, the nit is a zero-dimensional (0D) electron gas. In this case we can neglect the interactions between electrons. An ideal 0D electron is one that exists in a single state of fixed energy $E = E_0$. The density state is given by the Dirac delta-function $g(E) = \delta(E - E_0)$.

A quasi 0D character is shown in Fig. 2.1. The realization of the described low-dimensional structures are detailed later [2, 3, 5, 8].

## 2.2. Material Scientific Background

### 2.2.1. Properties of the GaAs and Related Materials

In this section, the bulk properties of an artificial material, namely the III-V compounds will be discussed. In the middle of the twenties century the semiconducting properties of the III-V compounds was discovered by H. Welker [15, 35]. At that time it could not predicted, what a fruitful field of semiconductor physics and its practical application would be opened up by this discovery. The experimental results and the theoretical calculations show that the III-V compounds have similar semiconducting properties to that of germanium and silicon. The III-V compounds are formed from elements of groups III and V of the periodic table. The first investigated material was the InSb. It was impossible to imagine that these III-V materials would have very remarkable properties, e.g. extremely high electron mobility, more higher than the values observed at previously known semiconductors. Since then the major emphasis of the scientific investigations of the III-V compounds has shifted quickly into the device technology of these semiconductors.

Here, mostly the GaAs as a sample material of the III-V compounds will be treated. The III-V materials crystallize mostly in the so called zinc-blende structure. This structure is formed in the same way as the well know diamond lattice, except that the two nearest neighbor lattice point are occupied by different elements, as cation and anion. The structure is shown in the Fig. 2.2. The diamond and also the zinc-blende lattices can be considered as two interpenetrating face-centered cubic lattices. For the diamond lattice, such as germanium, all the atoms are the same. In the case of zinc-blende structure, e.g. GaAs, one sublattice is Ga and the other one is As. The two sublattices are oriented parallel to each other and are displaced from one another by quoter of the body diagonal of the elementary cube of the face-centered lattice (Fig. 2.2) [16, 17, 18, 29, 30, 31, 33, 34, 213].

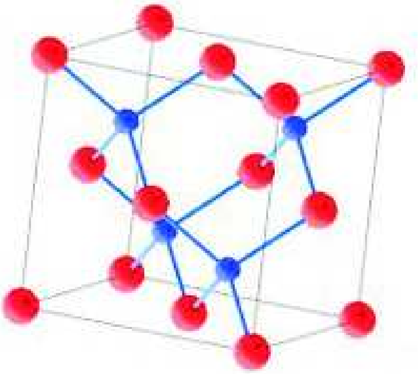

2.2. Fig. The zinc-blende crystal structure for GaAs.

In the diamond and the zinc-blende lattices every atom is surrounded by its four nearest neighbors. In the case of the diamond lattice, the atoms have four valence electrons. The chemical bound between the nearest neighbor atom is formed by two valence electrons with opposite spin. In the case of zinc-blende lattices, the neighbors have unequal number of valence electrons, but the sum of the valence electrons of two nearest neighbors is always eight. Each atom, on the average, still has four valence electrons available for bound formation. It can be described quantum mechanically by $sp^3$-hybrid wave functions. In the case of III-V materials, two kind of bonds can exist. Here, III-V compounds have primarily covalent bound, with only a small ionic bound contribution. In principle, the band structure of a solid is defined by the Schrödinger equation. In practice, because of the calculation difficulties, suitable approximations and number crunching are required. The shape of the energy bands, the location of the band extrema within the Brillouin-zone is found in the literature [17, 35]. Most of the III-V compounds e.g. GaAs have direct band transition opposite to the elementary semiconductors e.g. Si, which has indirect transition (Fig. 2.3).

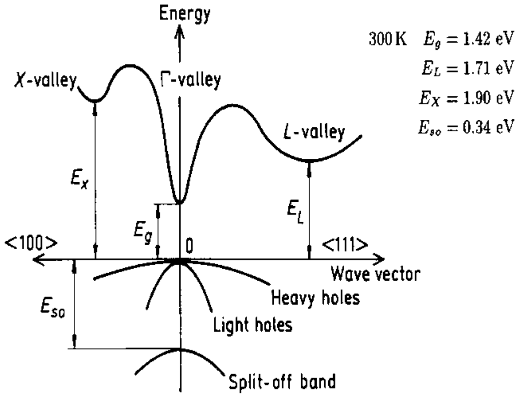

2.3. Fig. Simple energy band structure for GaAs.

The III-V compounds are not only binary compounds, but they can also form ternary and quaternary compounds. With the change of the composition, the band structure e.g. band gap changes as well. The function of the band gap v.s. lattice constant for the different III-V compounds are shown in Fig. 2.4.

It is important to talk about the phase diagram of these compounds [18, 19, 23, 24]. The basis of the ingot growth, the liquid phase epitaxy and also the droplet epitaxy is the control of the liquid-solid phase system. The phase diagram of the Ga-As system is described in Ref. [23, 25, 213, 28]. The phase rule states that the number of degrees of freedom in a system $(f)$ is given by $f = c - p + 2$, where $c$ is the number of components and $p$ is the number of phases. For a binary system e.g. GaAs, and pressure

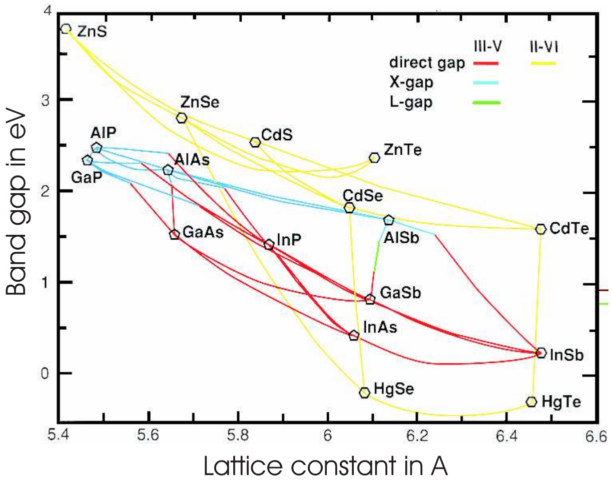

2.4. Fig. Band gap versus lattice constant for different compound semiconductors.

variations are neglected, when $c = 2$, $p = 2$, then $f = 1$. In the case of ternary (quaternary) system $c = 3$ (or 4), and $f = 2$ (or 3). The phase diagram for a ternary (or quaternary) system are more complex than for a binary one. A simple model and its variants have been used sucessfully to interpolate existing ternary and quaternary phase diagram data. For further information, we refer to the literature [18, 23, 25, 22, 27].

These materials have very advantageous optical, charge carrier transport and other technological properties. The direct band gap made it possible to produce different optical devices such as light emitting diodes or laser diodes. The very high electron mobility make it possible to fabricate various high-ferquency devices in the microwave range. The special electronic structure make it possible to produce a bulk device for microwave oscillator (Gunn diode). These materials can be produced by different epitaxial processes (liquid phase epitaxy (LPE), vapour phase epitaxy (VPE), and molecular beam epitaxy (MBE)). The properties of these materials allow us to grow layers and other structures with different composition on over each others. This property is so called homolog epitaxy. The lattice mismatch make it possible the production of the strain-induced nano-structures. The compound state give us the possibility for the droplet epitaxial method to produce different nano-structures (e.g. quantum dots (QDs) and rings (QRs)).

### 2.2.2. Surface Reconstruction of the III-V Materials

In this section we are dealing with the special structure of the surface, which is called surface reconstruction. The surface reconstruction means modified geometric and energy structure when compared to bulk properties. The kinetics of the grown layer and other structure depends strongly on the surface reconstruction of the substrate. For our discussion, the sample material will be the GaAs, because, GaAs (001) has become the archetype for the study of reaction kinetics, growth mechanism of III-V compounds. The surface reconstruction plays an important role in the homo- and heretoepitaxy to this family of materials [36, 38, 39, 40, 43, 91, 197].

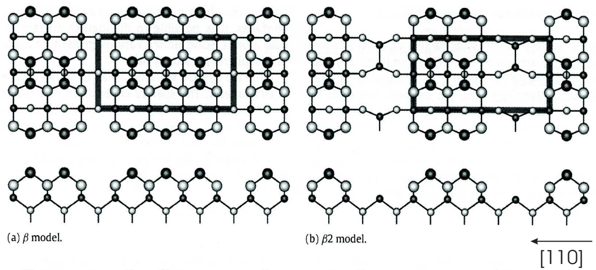

(a) $\beta$ model.

(b) $\beta2$ model.

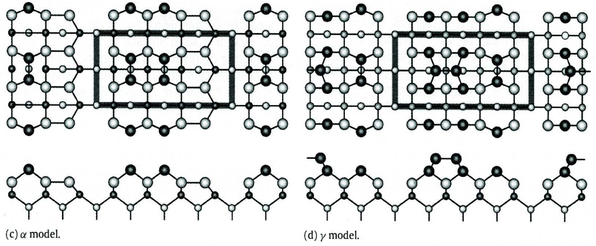

(c) $\alpha$ model.

(d) $\gamma$ model.

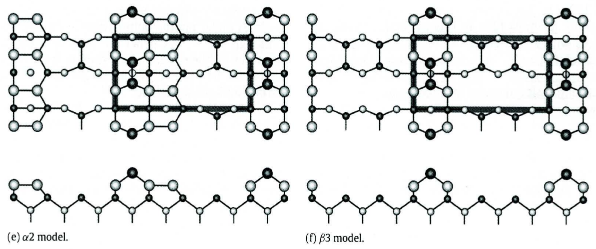

(e) $\alpha2$ model.

(f) $\beta3$ model.

2.5. Fig. Structure of (2x4) reconstruction for arsenic rich GaAs (001) surface. The dark circles represent As and the bright circles are Ga atoms.

The surface is always different from the bulk material, because it tries to relax by getting to an energy minimum state and involving various surface reconstructions [36, 38, 39, 40, 41, 42, 197]. The atomic structure at the surface is much more complex than in the bulk material. The co-ordination number of the top most atoms is reduced. This means that a number of the so called dangling bonds are left unsaturated at the ideally terminated surface. In some crystallographic direction, like (001) and (111) the up and down sides are not the same. In contrast the (110) surface is non-polar and the atomic arrangement at the surface only involves relaxation. The (001) and (111) surfaces are terminated either by anions or by cations. These polar surfaces are electrostatically unstable. As a consequence, the atoms at the surface are rearranged to generate an electrostatic potential. This potential fluctuates around zero with increasing distance into the crystal [43, 44]. The rearrangement of the surface atoms causes strain in the subsurface atomic layers closest to the surface, which are deformed. The reconstruction is not limited to the top most layer, thought the atomic displacements in the following layers are relatively small.

The reconstructions are also sensitive to temperature and the surface stoichiometry. These reconstructions can be understood since hybrid orbitals cannot form a bound at surfaces. Thus unreconstructed surfaces have unsaturated, that is partially filled dangling bonds, which are energetically unfavourable. The GaAs (001) surface can be terminated either As (see Fig. 2.5) or Ga atoms (see Fig. 2.27). We can observe two dangling bonds for each surface atom. In order to eliminate these dangling bonds, the surface undergoes complex reconstructions. In the case of the GaAs (001) surface, relative to the same surface of elemental semiconductors, the stoichiometry of the surface is especially significant. Here the chemical composition strongly influences the surface periodicity. In case of the stable surface, the dangling bonds of the electro-negative element (As) is occupied, and the dangling bonds of the electro-positive element (Ga) is empty [66, 269]. When these conditions is are satisfied, then the surface will be semiconducting, whereas partially filled dangling bonds may lead to a metallic surface.

The reconstructions depend on the surface stoichiometry. Technological, this means that the reconstructions are dependent on the substrate temperature and the flux of the components. The reconstructions have very complicated phase diagrams for each material and for different orientations of the surface. Rich variety of reconstructions are formed depending on surface stoichiometries. In first approximation there are two reconstruction phases to be taken into account. The first phase is when As rich surface forming at lower temperature, the second is when a surface, rich in Ga, forming at higher tem-

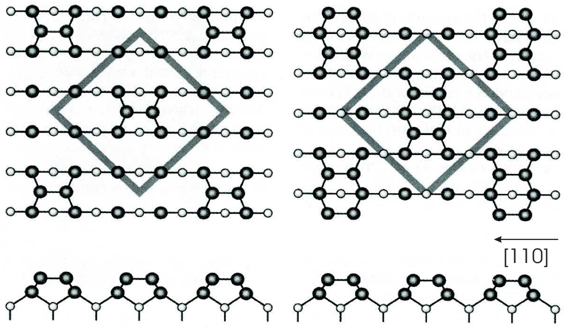

(a) One As–As dimer model. (b) Two As–As dimer model.

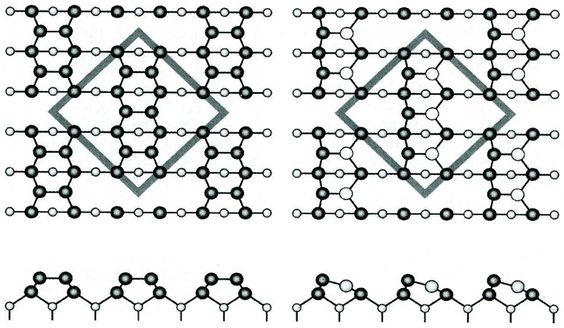

(c) Three As–As dimer ($\beta$) model. (d) Three Ga–As dimer ($\alpha$) model.

2.6. Fig. Structure of c(4x4) reconstruction for arsenic rich GaAs (001) surface. The dark circles represent As and the bright circles are Ga atoms.

perature. In case of GaAs the As rich formations are (2x4) (Fig. 2.5), c(2x8), c(4x4) (Fig. 2.6) or the Ga-rich are (4x2), c(8x2) (Fig. 2.7), (6x6), (4x6). Between them there are transitory reconstructions such as (3x1), (1x6). Due to the symmetry, one particular reconstruction may represent different atomic arrangements. The exception is the case of the (2x4) reconstruction, where the well-established models have been questioned, and new structure model has been proposed, where the views of the c(4x4) surface are different. One author regards it Ga-rich and another as As-rich [38, 63, 258].

For growing GaAs, the most widely used kind of reconstruction is the $\beta$2(2x4), which in the direction of [$\bar{1}$10] forms lines, made up of As dimer pairs with trenches between them with depleted Ga. This surface is called As terminated, after this particular structure. During growth, this represents a perfect surface with maximum reflectivity, although the surface is

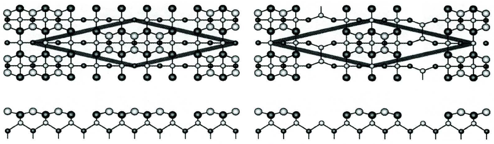

(a) $\beta$ model. (b) $\beta2$ model.

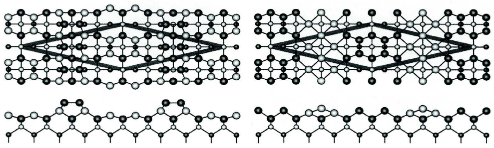

(c) Skala et al. (d) Jones et al.

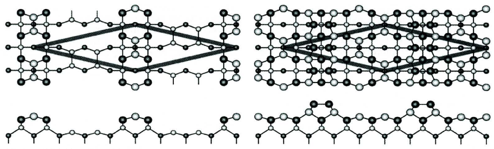

(e) $\beta3$ model (Ohkouchi et al.). (f) Torrelles et al.

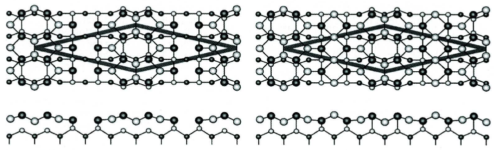

(g) $\zeta$ model (Lee et al.). (h) $\zeta$ model (Kumpf et al.).

2.7. Fig. Structure of c(8x2) reconstruction for GaAs (001) surface. The dark circles represent As and the bright circles are Ga atoms.

obviously not flat. For the Ga induced growth the starting surface is (2x4), formed in an As atmosphere [48, 91]. As the layers are grown one after the other, the surfaces of the successive layers become rougher, the oscillation decays and the specular spot intensity drops to minimum. In that case the Ga rich surface shows (4x2) reconstruction [48]. Tempering the surface, for reaching the maximum intensity, is carried out by heat-treatment in As rich atmosphere. With the increase of the secular spot intensity the (2x4) reconstruction reappeares again [36, 48, 91]. The various surface reconstructions are associated with different surface stoichiometry, which is closely linked to the RHEED intensity [63]. Although a large amount of information has already been compiled on the subject of surface reconstruction and its effect on the intensity and growth, there are still no acceptable comprehensive explanation of the whole phenomenon.

## 2.3. Growth of Low-dimensional Structures

### 2.3.1. Some Aspects to the Growth Kinetics

In this section, we review the relevant microscopic processes taking place on the crystal surface. The morphology of the interface is determined by the interplay between deposition, desorption and surface diffusion (Fig. 2.8).

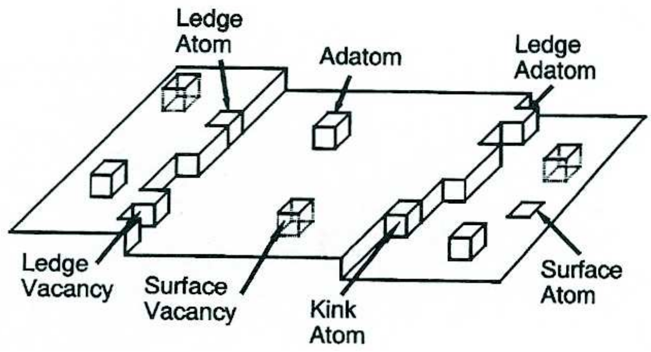

2.8. Fig. Schematic illustration of several defects that may occur on a crystal surface.

The deposition, if an atom from the environment arrives at a random position on the surface, create bonds with the surface atoms, and sticks. An effect competing with deposition process is the desorption. During desorption, some atoms deposited on the surface leave the interface. The probability of the desorption depends on how strongly the atom is bonded to the surface. When an atom is deposited on the surface, it forms bonds that must be broken before the desorption can occur. The strength of the bonds depends either on the type of atom or on the local geometry of the surface where the atom sticks. The lifetime of the deposited species is to measure the average time $\tau$ spent by this particle on the surface from deposition to desorption, which can be calculated with Arrhenius law $\tau = \tau_0 \exp(E_D/kT)$. Where $E_D$ is the characteristic desorption energy. The desorption can be neglible for many materials under typical MBE conditions. The deposited atoms diffuse on the crystal surface, searching for the energetically most favorable position. The diffusion length can be quite large, and depends on the temperature and the binding energies [72, 76, 77]. When a diffusing atom meets an island where the interface height increases by one atom, it exhibits a sticking preference for atoms located on the edge of the step. There is an additional potential barrier at the edge of the island that the atom must pass in order to jump off. This additional potential is called Erich-Schwöbel barrier [72, 76].

## 2.3.2. The Growth Modes

The structure growth can be classified in the following three modes: Layer-by-layer or Frank - van der Merve (FM), island or Volmer - Weber (VW) growth, and an intermediate mode (layer-plus-island) or Stranski - Krastanov (SK) mode (Fig. 2.9) [72, 76]. In the FM mode the interaction between the neighboring atoms in the layer is weaker than that with the substrate atoms. In the case of FM growth, islands of monolayer (ML) height coalesce before a new layer can nucleate on top of them. In the VW mode, the situation is opposite. In VW growth, growth proceeds to many atomic layers at discrete islands before these islands merge. In the SK mechanism, the growth is initiated in a layer-by-layer fashion, but islanding commences after the growth a certain thickness. In all but few situations, layer-by-layer growth is desirable because of the need for multilayered structures with flat interfaces and smooth surfaces. This requires that the nucleation occur as a single even, on the substrate. In the case of SK, the lattice mismatch between the grown layer and the substrate material is the most common case. The deformation undergone by the even layer to match the lattice of the substrate. In this case, elastic energy is generated in the structure, which deforms mainly the lattice of the layer. When this deformation energy overcomes a critical value, it can be relaxed in two ways. One possible way is to nucleate nano-sized islands on the even layer, which layer is called as wetting layer. The absence of the lateral contains allow the atomic planes to laterally relax reducing the elastic energy in the structure. The another way is to introduce misfit dislocations at the interface. According the first mentioned way, so called strain-induced QD can be grown [197].

The nucleation is an important part of the growth. The nucleation can be understand with the help of the simple homogeneous nucleation process. Homogeneous nucleation corresponds to direct condensation out of the gas phase, in absence of a substrate surface. This nucleation may proceed if a condition of supersaturation exists, meaning that the partial pressure of the nucleating species exceeds the equilibrium vapor pressure over the solid phase. Under a condition of supersaturation, embryos will form the vapor

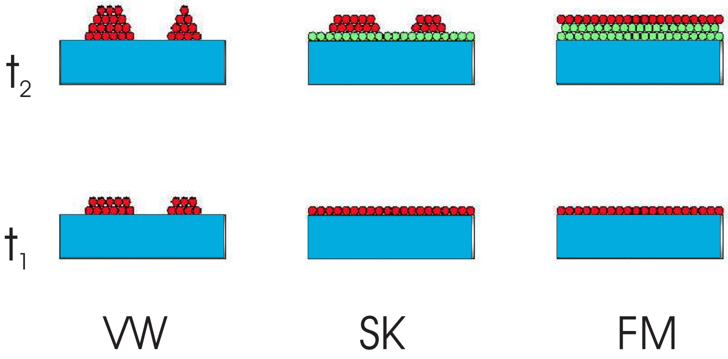

2.9. Fig. Schematic illustration of the three growth modes. VW: Island growth or Vollmer - Weber growth mode; SK: Layer-plus-island growth or Stranski - Krastanov growth mode; FM: Layer-by-layer growth or Frank - van der Merve growth mode.

phase. Some embryos will grow by the inclusion of additional material from the vapor phase, if they are large enough so that their growth reduces the overall free energy of the system. Other embryos will be less than the critical embryo size and will shrink by reevaporation.

The heterogeneous nucleation is close to the nucleation in epitaxial and in heteroepitaxial growth. Heterogeneous nucleation takes place in the presence of a surface. This nucleation mode may be considered from macroscopic point view, in fashion paralleling the treatment of the homogeneous case. The presence of a surface tends to increase the nucleation rate. This is because the nuclei may wet the substrate, greatly changing their geometry. The epitaxial material will not wet the substrate, because this would be accompained by an overall increase in free energy of the system. The epitaxial deposit will spread out to maximize the area of the interface. For all other situations, consideration of partial wetting with a contact angle $\theta$, where $\gamma_s = \gamma_i + \gamma_e \cos\theta$.Where $\gamma_e$ and $\gamma_s$ represent the surface free energies of epitaxial crystal and substrate, respectively, and $\gamma_i$ is the interfacial free energy. There are three types of situations: no wetting, partial wetting, and complete wetting. These situations correspons with FM, SK, and VW growth modes [76].

### 2.3.3. The Molecular Beam Epitaxy

The evaporation under ultra-high vacuum (UHV) is a classical method for preparing thin film [70]. Depending on conditions, the deposited films can also be crystalline. In this case the preparation method is called MBE [69, 71, 72, 73, 74, 75, 76, 77]. When the crystalline film grows on a substrate different from that of the deposited material, so the process called heteroepitaxy. MBE technology is based on the controlled interaction of beams of atoms and molecules on a heated crystalline surface under UHV conditions. MBE is the most versatile method for preparing well defined surfaces, interfaces, layer structures and different nano-structures of elemental- (Si, Ge) and compound semiconductors (GaAs, InAs etc.). MBE method allows also growth of film structures with sharp doping profiles and different chemical composition (e.g. AlGaAs) different lattice constant (e.g. GaAs/InGaAs junction). Multilayer structures with alternating doping or alternating band gap can be growth. A new field of band-gap-engineering was made possible by the development of MBE. Furthermore, QW, QD and other quantum structure can be grown with the help of MBE.

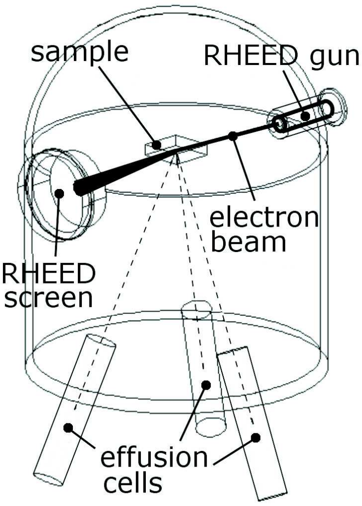

2.10. Fig. Scheme of a simplified UHV growth chamber for MBE.

As we mentioned before, MBE is a kind an UHV deposition technique, that involves the impingement of atomic or molecular beams onto a heated crystalline substrate where the epitaxially layer grow (Fig. 2.10). The source of the molecular beams originate from effusion (Knudsen evaporation) cells (or gas-source crackers). These can be opened and closed very abruptly by shutters (or valves), providing atomic layer abruptness. Because MBE process takes place in a UHV environment, it is possible to employ a number of in-situ characterization tools based on electron (or ion) beams. These provide the crystal grower with immediate feedback, and improved control of the growth process. An MBE reactor chamber involves a number of source cells arranged radially in front of the substrate holder. The source cells supply all atoms necessary for the growth (and also for the doping) of the required semiconductor layers or of other nano-structures.

The mean free path for an evaporated atoms or molecule may be estimated if it assumed that all other particles in the system are at rest. If we suppose, that the evaporated particle is moving with velocity $c$, and all particles have around cross section with diameter $\sigma$. Two particles that pass at a distance of $\sigma$ or less will collide. Therefore, each particle can be considered to have a collosion cross section of $\pi\sigma^2$, and the collosion volume swept out by a particle in time $dt$ is $\pi\sigma^2 cdt$. If N is the volume concentration of particles then the collosion frequency will be $f = N\pi\sigma^2 cdt$ and the mean free path will be $\lambda = c/f = (N\pi\sigma^2)^{-1}$. The free path can be calculated as a function of pressure: $\lambda = kT/(\sqrt{2}\pi\sigma^2 p)$. Typical value of the cross section diameter is about 2 Å, so the free path is about $10^3$ cm at $10^{-5}$ Torr. This pressure represents the upper limit for the background pressure during the growth process. The requirement on the background pressure is considerably more stringent and is set by purity requirements. So, the base pressure to have about $10^{-10}$ Torr.

Different MBE variants have been developed. They are solid-source MBE (SS-MBE), gas-source MBE (GS-MBE), metalorganic MBE (MOMBE) etc. The MBE chamber is equipped with pump system that give the above mentioned base vacuum pressure in the range of $10^{-10}$ (or $10^{-11}$) Torr. This UHV condition is required to reduce the back ground contaminant and it can be hinder the contamination of the deposited structure. (Because the UHV environment quarantee the collosion-free path of the atoms and molecules from the source to the target.) GaAs and other related materials can be grown by MBE. These materials are most often grown on GaAs substrates (oriented mainly (001) direction). However, heteroepitaxy on Si, InP substrates has been investigated intensively with the goal of integrating AlGaAs devices with those from these other material systems. InGaAs is usually grown heteroepitaxially on InP or GaAs substrates.

### 2.3.4. The Jointed MBE Research Laboratory in the KFKI Campus

Our jointed MBE Research Laboratory of MFA and BMF (Legal successor today is ÓE.) was established in year 2008 [78, 79, 80]. The laboratory with the MBE equipment is located in Csillebérc, in KFKI Campus. Our MBE equipment is for growth of III-V compounds. The experimental setup described here is the only one presently in the whole country (Fig. 2.11).

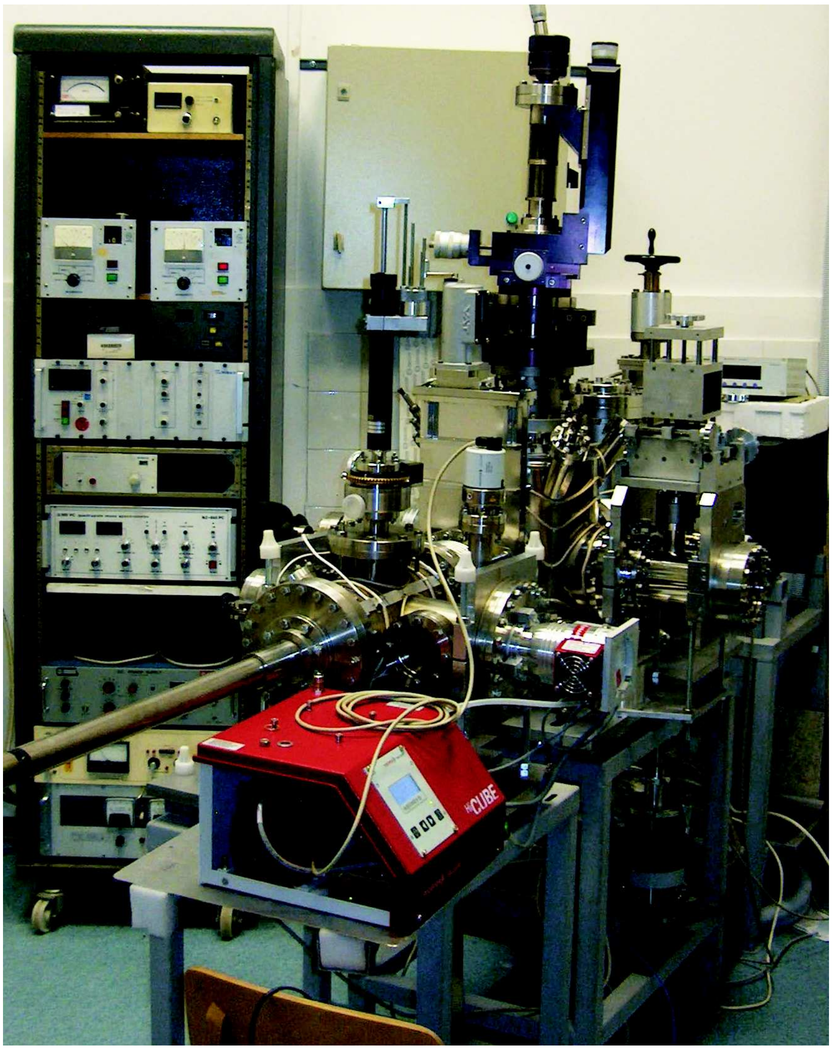

2.11. Fig. View of our MBE equipment in the jointed laboratory.

This equipment consists of three UHV chambers. One of them is the reactor or main chamber for sample preparation. The main chamber has a heatable sample holder mounted on a precision manipulator. The sample is mounted on the Mo holder by liquid indium. In front of the sample holder, four Knudsen cells are located. Knudsen-type crucible are used as effusion cells for the evaporation. Our molecular sources are arsenic, Ga, In and Al. These cells are tubular crucibles made from pyrolytic boron nitride. The crucibles are mounted within spiral Ta heater windings which are themselves enclosed within Ta-foil radiation shields. A requirement for the source oven and the whole unit is a very low production of impurities in the molecular beam. The oven set-up is therefore surrounded by a water cooled panel on which shutters are mounted which can close and open one or the other effusion cell. Also the space between sources and the sample is shielded by a cooling shield at liquid nitrogen (see Fig. 2.13.). This chamber has also a 12 keV RHEED equipment (type Riber CER 606-ACE 1010) for monitoring of the sample during the growth (Fig. 2.12). A fluorescent screen is located in opposite of the RHEED electron gun. Our MBE has a home made Faraday cup to measure directly the electron current (the explanation see later). A quadrupole mass spectrometer (QMS) (type: Pfeffer QME 220) is also mounted on the chamber to investigate the environment during the growth process. The measuring range is to 300 amu. The vacuum can be measured also with a vacuum gauge.

Another chamber of the equipment is the loading chamber. This chamber has an two-axes manipulator with sample holder for places of five samples, a load-lock window, an magnetic rod for the sample transport. This chamber is pumped by a turbo molecular pump (type: Pfeiffer HiPace 80). The pressure is measured by a vacuum gauge (type: Pfeiffer IKR 270). The third chamber is an additional chamber for vacuum pumps, they are a turbo molecular pump (type: Balzers TPU 520) and an iongetter pump (type: Varian Diode). Both pumps can be separated from the chamber with the help of gate valves (type: VAT 160 CF). Further Vacuum valves are between the chambers.

The MBE growth needs very high requirements with the equipment. So we have to use a reliable and precise control [82, 123]. Before the crystal growing procedure started the equipment need to be heated up, following a specific temperature characteristics to evaporate different contaminating materials and clean the vacuum chamber (see Figure 2.13.). In our case, the UHV condition means $10^{-10}$ - $10^{-11}$ Torr pressure. After the closing of the system, we need the outheating of the chambers to achieve this vacuum level.

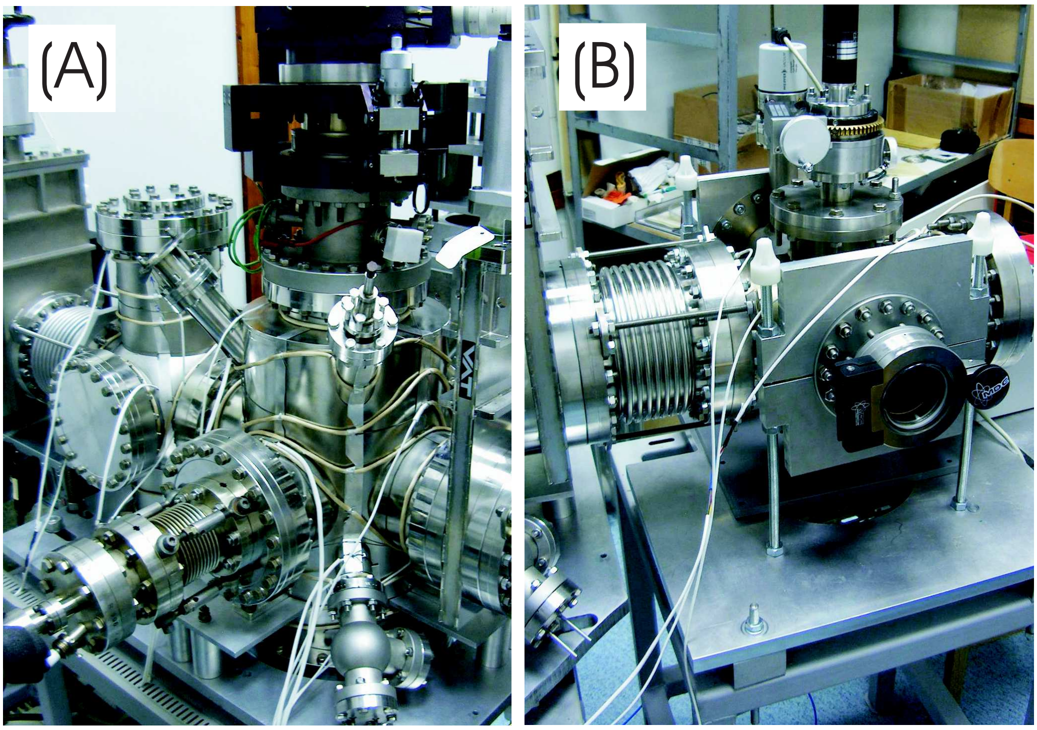

2.12. Fig. Our equipment; (A) The view from the RHEED gun; (B) The view of the window of the load-loch chamber.

The outheating needs slow control without overshoot. The temperature is measured at 10 different points and around 10 heating wires are controlled. The closed loop heat control is done by the Simatic S7 PLC which runs PI control algorithms to ensure error free tracking of the temperature setpoint [82, 84, 85].

For the sample preparation and its investigation, we need also very accurate control of the MBE equipment (Fig. 2.12). We have to control not only the heating out system of the vacuum chambers, but the control of the furnace of the molecular sources (Knudsen cells) and the control of the moving of the shutters. In the view-point of the electronics, the control is slow. The growth rate ranges between 0.1 - 1 ML/sec. In the case of the shutter movement, we need less slow control, because the shutter have to close before the next ML begin to growth. The heating of the effusion cells and the sample holder are also relatively slow processes because we need processes also free from overshoot. Because of the reliability, we use also PLC system for the control of the MBE.

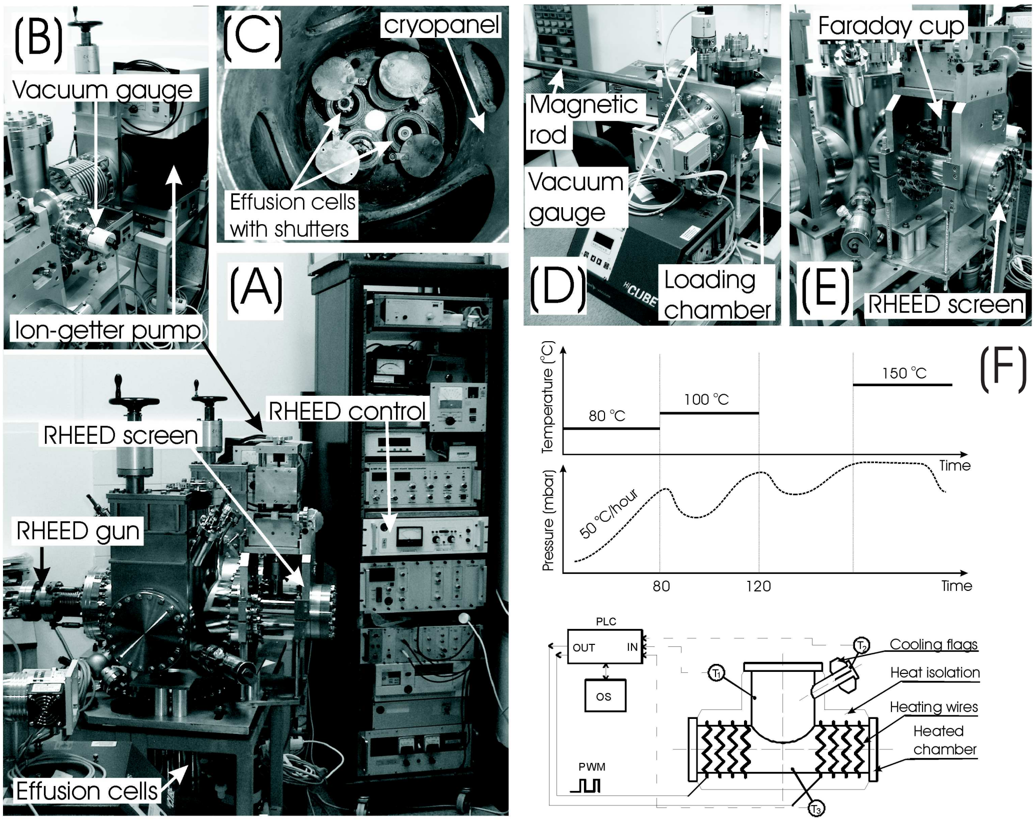

2.13. Fig. Some pictures about the MBE system during the installation. (A): the main chamber with the electronics, (B): the additional chamber with the ion-getter pump, (C): inside of the reactor chamber, (D): the loading chamber, (E): the RHEED diagnostics (F): Heating control using PLC and OS.

The whole system is operated from a PC operator station (OS). The OS reads and writes the process variables of the PLC and, displays the system state (see Figure 2.13.). The temperature characteristics and other functions such as the sequential control of the molecular sources can be parameterized on the OS (and controlled by the PLC).

As we mentioned before, we use Faraday cup for intensity measurement of the electron beam. The RHEED pattern and oscillation intensities are recorded usually by video camera focused on the fluorescent screen. The fluorescent film on the window and the camera have non-linear behaviour in the intensity, which can deform the observed intensity distribution. If we want to investigate the real intensity and their accurate relation, we must measure the electron current directly. The direct measurement is possible by means of a Faraday cup. This cup has three pinholes along a line of decreasing diameters (0.5, 0.3, 0.1 mm) in order to obtain good angular resolution and suppression of the electron background. This cup is attached to an extra precision manipulator [86, 87].

## 2.4. In-situ Investigation of the Growth

### 2.4.1. Basic Concept of the RHEED

The RHEED is a widely used monitoring technique in the MBE growth [72, 77, 208]. This technique is applicable for surface structural analysis that is simple to implement, requiring only an electron gun and a fluorescent screen in the UHV chamber. RHEED has proved to be very versatile tool for growth and surface studies of semiconductor layer and other nanostructures prepared by MBE. The arrangement of MBE in which the atomic and molecular beams are incident ca. normally on the substrate plane enables diffraction features to be monitored continuously during the growth process. This investigation technique is based on the interaction of the electron beam and the studied surface, where beam energy is ranged typically between 1 - 3°. The operation principle is illustrated in the Fig. 2.14.

The incoming electrons with $\bar{k}_\circ$ wavevector have grazing incidence with respect to the surface plane. Therefore, they will mainly scattered from the top layer of the sample. The scattered wave vector of the electron beam $\bar{k}_1$ differ by a reciprocal-lattice vector of the surface $\bar{G}$: $\bar{k}_1 - \bar{k}_\circ = \bar{G}$. When considering only elastic scattering, which means $| \bar{k}_1 |=| \bar{k}_\circ |$ this diffraction condition can be cast into geometrical construction of the Ewald sphere in reciprocal space. Where the arrow of $\bar{k}_\circ$ is attached to reciprocal-lattice point. The sphere around the origin of $\bar{k}_\circ$ with radius of $| \bar{k}_\circ |$ defines the Ewald sphere. Reflections can occur for all $\bar{k}_1$ connecting the origin of this sphere and a reciprocal-lattice point on sphere (Fig. 2.14).

Because of its small penetration depth, owing to the interaction between the incident electron beam and surface atoms, RHEED is sensitive to the

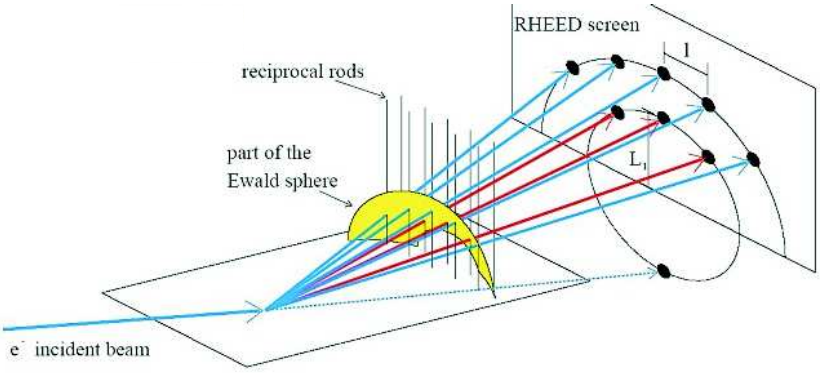

2.14. Fig. Ewald sphere construction and diffraction geometry of the RHEED.

atomic structure of the first few planes. This technique is very appropriate to determine the surface reconstruction (Fig. 2.15). Diffraction from a struture periodic in only two dimensions therefore underlines the observed patteren, and the positions of the elastically scattered beams can be determined from single scattering expression. The interpretation is very complicated and has many open questions, because of the unusually asymmetric scattering geometry and of the necessity of accounting for multiple scattering processes [89, 90, 92].

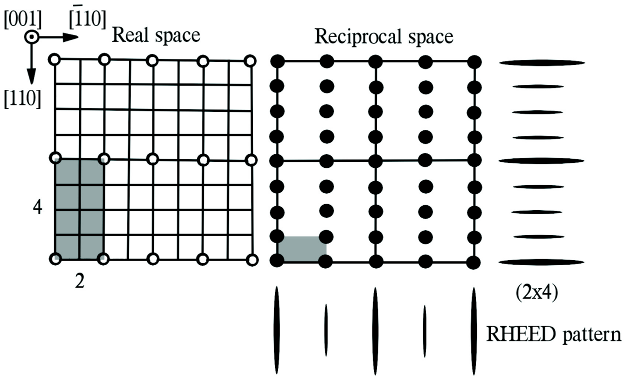

2.15. Fig. The RHEED is very appropriate technique to determine the surface reconstruction. Demonstration of the (2x4) reconstruction.

On the fluorescent screen, the intensity of the RHEED pattern changes during the crystal growth. Oscillatory response to a surface-sensitive probe during thin film deposition is generally considered to be the manifestation of two dimensional layer-by-layer growth mode. This phenomenon can be explained as follows: At the beginning, the reflection of the electron beam is high from the surface, resulting in high specular spot intensity. During the process of growth, crystalline islands forms on the surface. The initial surface loses its smoothness and becomes rougher. This results reduced reflection, because of larger electron dispersion (Fig. 2.16). The model is a very rough simplification of the very complicated interaction [88, 90, 91, 93].

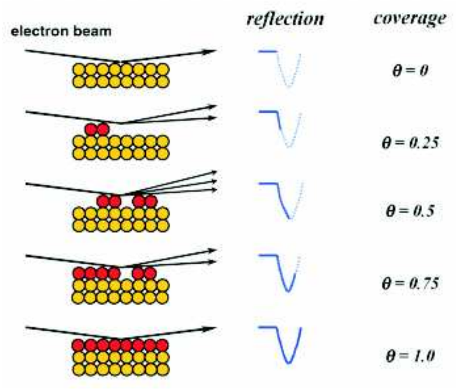

2.16. Fig. Lucid explanation of the RHEED oscillation originated by B. A. Joyce.

The intensity of the specular beam depends on the incidence and the azimuth angle of the electron beam. The interaction on the surface can be treated as a multiple scattering process, so the elastic component of the specular intensity is attributed mainly to multiple diffraction and surface resonances. There is a very significant contribution from inelastic and incoherent processes, with the portion of elastic/inelastic process depending on azimuth, incidence angle and energy. As a result of the beam penetration it is also necessary to take account of refraction effects in considering the angular position of emergent electrons [88, 89, 90, 91, 92, 93].

### 2.4.2. Some Open Questions in the Interpretation of Static and Dynamic RHEED

As we mentioned before, the RHEED is a widely used monitoring technique during MBE growth. The orientation, quality and reconstruction of the grown surface can be determined by the RHEED pattern. Compared to other in-situ investigations, the glancing-incidence-angle geometry of RHEED is ideally for the in-situ observation of growth process and furthermore has very high surface sensitivity. The penetration depth of electron beam into the surface, can be changed by the variation of the incidence angle. The intensity of the RHEED pattern oscillates under appropriate conditions during the growth process [91]. One period of these oscillations corresponds exactly to the growth of one complete monolayer (ML) in the case of the layer-by-layer growth mode. The growth rate, and the composition in the case of alloy materials can be determined with the help of RHEED oscillations [48].

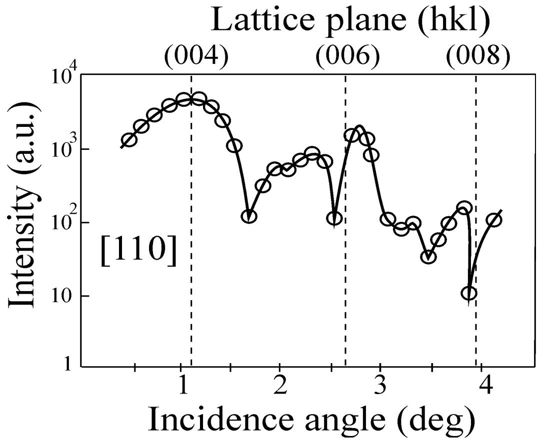

2.17. Fig. Intensity of RHEED specular spot as a function of the angle of [110] azimuth from GaAs (001) (2x4) reconstructed surface.

RHEED and its oscillations of intensity are very complex phenomena. This technique is a versatile tool for in-situ monitoring, in spite of the fact that we do not know many details of its nature. This oscillation is characterized by the period, amplitude, phase and damping of the oscillations, the behaviour at the initiation of growth, the recovery after growth and the frequency distribution in the Fourier spectrum of the oscillations. The origin and describing of oscillation were investigated by several authors [38, 39, 41, 42, 197]. Many properties and behaviours of the oscillations are not yet understood. For example, some of these problems are the different phases of the specular and nonspecular RHEED beams [40], and the varied behaviour of the oscillations in the case of III-V and II-VI materials [41]. There are still more interesting and open problems in the topic of the decay of intensity oscillations and of the initial phase change, etc. Several authors have tried to describe these phenomena [42]. Several effects can be interpreted by the above mentioned geometrical description. The oscillations in the case of two-dimensional growth mode, the disappearance of oscillations by step propagation, and the exponential decay of the oscillations can be explained by this geometrical description, too [42, 43, 44].

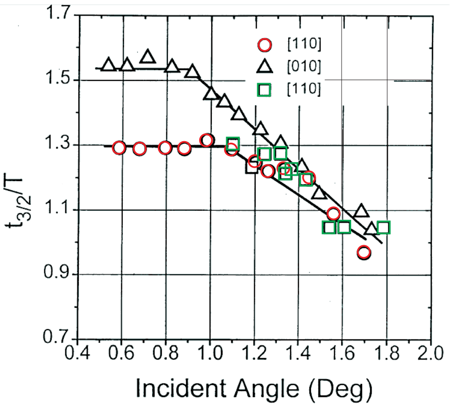

2.18. Fig. Phase relationship of RHEED specular spot as a function of the angle of [110] azimuth from GaAs (001) (2x4) reconstructed surface.

The RHEED is a suitable technique to investigate the binding properties on the surface. Furthermore, it is appropriate to distinguish special crystallographical directions, for which X-ray diffraction (XRD) is unable. This crystallographical direction are e.g. on the (001) surface, where the [110] and

$[1\bar{1}0]$ directions have different properties in crystallographical and in technological view, too. However the dynamic RHEED is appropriate to determine and calibrate the growth parameters, such as e.g. growth rate and molecule flux [43, 44, 45]. One of the interesting problems is the initial phase change of the oscillation, which is depend on the direction of the incident electron beam, and the technological parameter, too.

The amplitude and period of the initial swing of RHEED oscillations are different from what follows. Except for the first period, the measured decay of the oscillations fits well to an exponential function [43]. The incident electron beam impinges on the surface with low angle. If we change the incident or the azimuthal angle, the initial phase of the oscillations changes, too. For the phase change investigations, GaAs (001) serves as good model material [40, 42]. There are several models, which describe this phenomenon in broad range of incidence angle [45, 46]. These generally scattering based models take into account more MLs. These approaches describe qualitatively well the phase switch in the range of incident angle to about 4 but the fitting e.g. at low angle under 2 has some deviation from the measured curve.

### 2.4.3. A Quantum Mechanical Interpretation of the RHEED Oscillation

A simple reflection based model of the effect was described by Joyce soon after the discovery of the oscillations [91]. According to his work, the oscillating intensity can be explained by the changing of the surface morphology. The complete layer which has maximum reflection corresponds to the maximum intensity and the rough surface in intermediate state which has minimum reflection corresponds to the minimum value of the oscillation respectively. In this model the complete monolayer surface behaves as a perfect optical grating producing diffraction pattern with the maximum possible contrast. The building of the new layer manifests as more and more arising impurities that destroy the diffraction pattern. As the growth process gets near to a perfect monolayer, at about half filled layer, where the diffraction pattern has the least contrast, the holes, i.e., the spots without elements from the new layers start to be the impurities on the grating, thus with always decreasing impurity number the diffraction pattern starts to be regenerated. The usefulness of this description can be underlined by the fact that it can be applied for the explanation of the intensity decay of RHEED oscillations

[48]. However, the symmetry to half-filled layer of the model and the asymmetry of the practical results are in contrast, thus more sophisticated models were introduced.

The diffraction-like behaviour of the electron is used in the kinematical model introduced by Lent and Cohen, which can explain the origin of the RHEED intensity oscillations as well [102]. The particular oscillations are explained considering elastic and inelastic processes such as electron, phonon and plasmon scatterings on the surface layer as well as the first few covered layers [103, 50].

These descriptions of the RHEED phenomenon are not fully satisfactory, i.e., they describe the behavior of the RHEED only under special conditions; moreover, they contain rather rough approximations and neglections. The asymmetry of the oscillations to the half-filled layer is also not described. By introducing step density between the growing and the already grown layer, the model can be refined [105, 41, 107, 108], but the calculations become more complicated with more fitting parameters.

However, we can not give up the semiquantitative quantum-mechanical approach. There is, e.g., the surface coherence length, which was introduced by Beeby [109], which was used for explaining the behaviour of the initial phase of RHEED oscillations [221], and which should be included in the further models of the reflecting electrons.

The quantum-mechanically exact description of RHEED phenomenon is very sophisticated and practically it can not be carried out because of the high number of interacting particles. However, a phenomenological description can be rather successful. The investigated quantum-mechanical entities, such as the electrons can be approximated as particles or waves under different experimental conditions. The surface morphology is changed during the growth process, which causes changes in the experimental conditions. These condition variations determine the type of the interaction. We usually say, that a quantum mechanical entity (like the electron) shows particle-like behavior if its path to the interaction place can be given exactly, i.e., in the case if we can somehow identify its path, there is only one energetically most efficient path. The same entity shows wave-like behavior if this path can not be exactly identified, i.e., it can move from one place to another along more different, but energetically indistinguishable paths. This complementary behavior depends on the experimental conditions. The complementarity itself is independent of the uncertainty relation, which was demonstrated by Dürr, Nonn and Rempe in a two-slit experiment [111].

The observation of the path of a quantum entity is usually possible by its interactions with other quantum entities. Quantum entanglement of two or more quantum mechanical particles is generated during the interaction between these entities. According to the philosophy of Buchanan, these new quantum entanglements destroy the interference with any other entities, not entangled with the studied particle [112].

In our model philosophy, the quantum entanglement between the incoming electrons as quantum entities and the already present macroscopic diffraction lattice can be neglected. The electrons can however build correlated, or entangled states with the atoms or small clusters of atoms in the newly building layer. (Similarly with the holes in the almost finished layers.) Usually, entanglement is meant between identical particles, but there is no strict rule against entanglement between electrons and more complex quantum mechanical objects. It is important to emphasize that the size of the investigated objects is small enough to exhibit quantum behavior. The quantum behavior of much larger objects (like $C_{60}$ molecules) containing much more atoms was already shown [113]. The principle of complementarity and the quantum entanglement can help us in the description of RHEED oscillations.

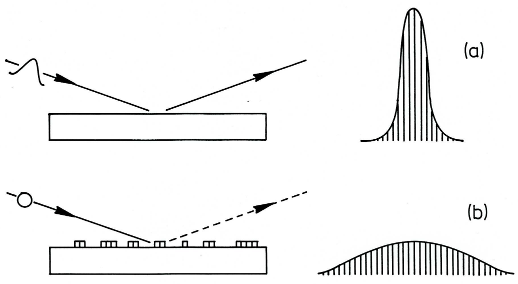

2.19. Fig. The electron beam impinges on the sample under grazing incident angle. Upper part: Experimental arrangement at perfect surface. The electron interacts with the crystal as a diffraction lattice. Electron shows wave behavior. The quantum entanglement is insignificant in this case. Lower part: Experimental arrangement at rough surface. The electron interacts with atoms and atom groups. Electron shows particle behavior. The quantum entanglement is dominant in this case. ((a) and (b) mean intensity at perfect and imperfect surface, respectively.).

Let us investigate the RHEED phenomenon on the basis of above mentioned quantum mechanical ideas. If the crystal surface was complete and perfect, then the electron wave functions after the scattering on the complete "grating" (the rows of the surface atoms) would differ in the phase. In the maximum intensity cases, the wave functions of the electrons sum up with their phase being the same, in dark point with exactly opposite phase, thus interference is obtained. To give a mathematical description, the wave functions with different phases are indexed with number 1, 2, 3, etc., thus the collective resulting function can be given as follows:

$$\Psi \ \sim \Psi_1 + \Psi_2 + \Psi_3 + \ldots, \tag{2.1}$$

If the electron interacts with a perfect crystal surface, it behaves like a wave. The "electron wave" interacts with the crystal lattice as if it would be a diffraction lattice. The size of the crystal is macroscopic. Experimentally reasonable quantum entanglement does not arise between the electron beam and the lattice. We can observe partial diffraction pattern which originates from the interference of the electron waves. In these cases we do not have a definite path of the electron for the description of the interaction, i.e., we have several different paths simultaneously, because a translational crystal symmetry exists in the lateral direction of the surface. This experimental condition results in sharp diffraction pattern as it is shown in the upper part of 2.19.

If the crystal surface is not fully occupied by atoms, the upper layer consists of quantum objects such as atoms, atom groups or holes in the layer. These quantum objects are different although they consist of same atoms because they have different sizes, different shapes and different connections with the surface. These atoms and the atom groups are quantum objects with which the electron beam interacts quantum mechanically. The quantum entanglement generated by the incoming entities varies during the interaction. The reason of this variation is, besides the topological difference in the initial surface, the difference in the growth process in different conditions. If the larger clusters of atoms (holes) are preferred during the growth process, the entanglement becomes less, while in case of small, but several clusters, the entanglement can be quite large, and can attain more incoming electrons. For a mathematical summary of the entanglement, some notations should be introduced. Let us denote the different surface quantum objects with A, B, C, etc, the electrons with 1, 2, 3, etc. The resulting, entangled wave function can be given in a direct product wave function basis as

$$\Psi \sim |\Psi_1\rangle \otimes |\Psi_A\rangle + |\Psi_2\rangle \otimes |\Psi_B\rangle + |\Psi_3\rangle \otimes |\Psi_C\rangle + \ldots, \tag{2.2}$$

where the numbered and lettered functions describe incoming electron and surface objects respectively. As the number of small clusters increases during the growth process, the number of possible quantum objects for interaction with the incoming electrons grows, thus formation of interfering substances has smaller probability. In this case the sharp diffraction pattern is smoothened [112]. The electron interacts with the discrete entities on the surface, i.e., we can identify the electron path to the interaction place. The particle-like property of the electron dominates its behavior and overcomes the wave property. This results in a less intensive diffraction as it is demonstrated in the lower part of 2.19. It can also happen, that the atom groups tend to cluster to larger, non quantum mechanical objects, and e.g. the holes in the newly growing layer tend to remain separated, in this case an inflection, or even a turnback can arise in the contrast oscillation intensity plot.

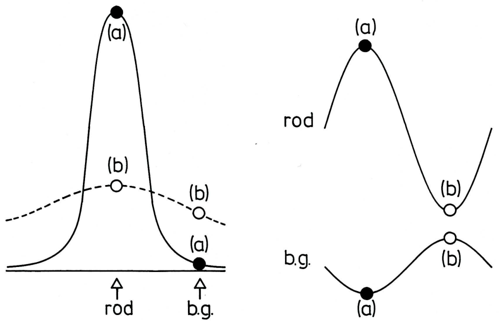

2.20. Fig. Left part: The RHEED intensity distribution at smooth (solid line) and at rough (dashed line) surface. Right part: RHEDD intensity vs. time; The intensity oscillation at the place of rod and background (b.g.) show opposite phase behavior. ((a) and (b) mean intensity at perfect and imperfect surface, respectively.).

According to these simple considerations the pattern intensity of the diffraction has maximum value when the surface is perfect and at its minimum value intensity takes place when the surface is roughest, i.e., when the largest number and most diffuse interacting entities are present on the surface, thus the most of the entanglements can be formed. This state does not always correspond to the half-filled layer in the growth process. The experimental results show that the background intensity between the diffraction rods has a small oscillation, too. The intensity oscillations of the peak and the background are in opposite phase [48]. Let us observe Fig. 2.20. The intensity oscillations of the peak show a maximum value at smooth and minimum value at rough surface. Simultaneously, the oscillations of the background show exactly the opposite behavior, the maximum is when the surface is rough, and the minima take place at smooth surfaces.

### 2.4.4. Particular Behaviour of the RHEED

The phase of the oscillation depends on the incident angle of the electron beam. However the very useful kinematic theory does not predict the phase shift of the oscillations, which depends on the condition of the electron beam. The contribution of inelastic processes such as Kikuchi scattering to the phase shift penomenon is not completely taken into account [91]. The RHEED phenomenon is partly reflection-like and partly diffraction-like. The effect of phase shift is described by the position of the minima of the oscillations. The behaviour of the minima and maxima of the oscillations can also be explained with a geometrical picture, which will be employed in this case. Because the specular spot is not a reflected beam, the interaction of the electron beam and the target surface must be described quantum mechanically. The glancing-incidence-angle electron beam touches the surface over a large area. The reflected-diffracted information obtained does not come from the whole area. The interaction between the surface and the electron beam exists only under special conditions, therefore we need to consider the surface coherence length (SCL) ($w$) [99]. The wave function after the interaction $|X_a\rangle$ is written as follows:

$$|X_a\rangle = W_B(r_1)W_T(r_2)|\chi_a\rangle, \tag{2.3}$$

where $W_B(r)$ and $W_T(r)$ are the wave packet of the electron beam and the interacting surface of the target, respectively. With the solution of this equation it can be shown that the SCL depends on the interaction potential between the incident electron and the target and depends less on the wave packet [109].

We can suppose that the SCL ($w$) is of the same order as the coherence length ($\Lambda$) of the beam. The energy of the electron beam is on the order of

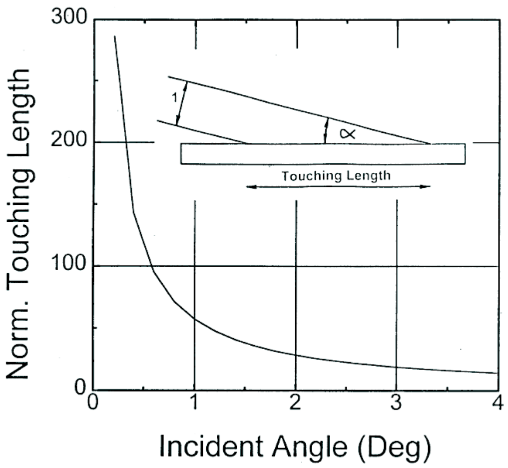

2.21. Fig. The normalized touching length of the electron beam vs. incidence angle. The SCL is assumed to show similar behaviour.

E = 10 keV, with a de Broglie wavelength = $12.2 \times 10^{-12}$ m. The coherence length of the electron beam is [95]

$$\Lambda = \frac{\lambda}{2\beta\sqrt{1+(\Delta E + E)^2}} \tag{2.4}$$

where $2\beta$ is the divergence of the electron beam and $\Delta E$ is the full-width at half-maximum (FWHM) of the electron beam energy. These two quantities are usually $10^{-3}$ and 0.1 , respectively. The wave packet extends $\Lambda_1 = 12.2$ nm with these values. The wave packet from interference investigations is $300\lambda$ [96]. By this measure we get $\Lambda_2 = 3.7$ nm for the wave packet.

The spot size of the illuminating electron beam on the surface in the incident direction depends strongly on the incident angle. The size of the touching area between the beam and the surface in the case of unit beam width can be seen in Fig. 2.21. This dependence is very strong in the vicinity of an incident angle of 1°. We can suppose that the SCL depends on the incident angle, too.

The relation between the size of characteristic growth terrace (s) and the SCL (w) in the case of a polycrystalline surface was investigated in Ref [109]. This concept can be applied in our case if we use, instead of domains, identically oriented growth units (or growth terraces).

An estimate of the characteristic dimension of a growth terrace can be given from experiments. The terrace average width ($s$) and the migration length of Ga ($l$) depend on the substrate temperature. The RHEED oscillations are present if $l \leq s$ and absent if $l \geq s$. In our case, the migration length is 7 nm because the substrate temperature is 580 °C [91].

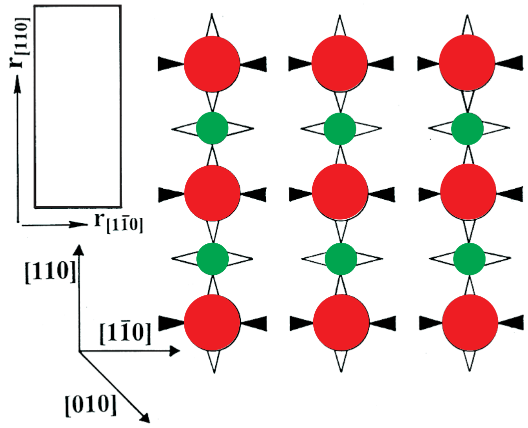

2.22. Fig. The lattice of GaAs projected on the (001) plane. The red and green circles represent the As and Ga atoms, respectively. The black triangles are the dangling bonds, which cause different rates of composition (growth) and decomposition (etching) of the crystal in different directions. The component of growth rate in the direction of the investigating electron beam $r_{\|}$ and the perpendicular components $r_{\perp}$.

The binding energy on the (001) surface in the direction [110] and [1$\bar{1}$0] is not the same, which explains the dangling bonds in Fig. 2.22. This anisotropy is manifested in the different growth rates. The growth rate in the [110] direction is larger than that in the perpendicular direction [97]. This anisotropy is apparent not only in the growth of the crystal (in other words composition of the crystal) but also in the etching (that is decomposition) of the crystal. The growth rates in the [110] and [1$\bar{1}$0] directions are different by more than factor of two. This factor can be estimated with the help of etch-pit shapes [98].

We can suppose that the SCL and the average terrace width have commensurate dimensions at glancing-incidence-angles ($w \approx s$). This supposition seems right, because the touching length of the electron beam (also the SCL after our supposition) changes very abruptly at angles less than 1° and in this region the function $t_{3/2}/T$ is constant accordingly as $w > s$. The relation between SCL and average terrace width is changed with changes in the incident angle. If the incident angle increases, the SCL becomes smaller than the average terrace width ($w < s$), so and thus reflected-diffracted informations comes from only a part of the average terrace.

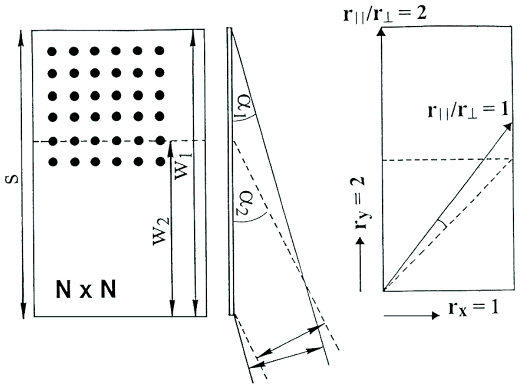

2.23. Fig. View of one island with lattice nodes in the growth model consisting of islands of $P \times P$ terraces of $N \times N$ lattice sites (where $N = 36$, $P = 4$). The relation between the terrace dimension and SCL is illustrated.

For calculation, we used the polynuclear growth model in the two-dimensional case [99]. The simplified picture takes into consideration diffraction contributions only from the top most layer and the RHEED intensity is taken as proportional to the smooth part of the surface top layer [48]. The arrangement of our computing model is similar to that of Ref. [114], which contains $N \times N$ lattice sites in a $P \times P$ growth terrace (Fig. 2.23). The reflected beam intensity corresponds to the surface coverage $\Theta$ as follows:

$$I(t) = \begin{cases} \Theta_n(t) \rightarrow if{:}\Theta_n \geq 0.5 \\ 1-\Theta_n(t) \rightarrow if{:}\Theta_n < 0.5 \end{cases} \tag{2.5}$$

The relation between the terrace size and the area of surface coherence is shown in Fig. 2.23. The information supplying surface area decreases with inceasing incident angle of the beam. The different crystallographic directions mean different growth rates. Because we do not know accurately the ratio $r_{[110]}/r_{[1\bar{1}0]}$, the oscillations were calculated under ratios of $r_{\|}/r_{\perp} = 2$ and $r_{\|}/r_{\perp} = 1$, where $r_{\|}$ and $r_{\perp}$ are the components of the growth rate in the observation direction (parallel with the incident electron beam) and the perpendicular direction, respectively.

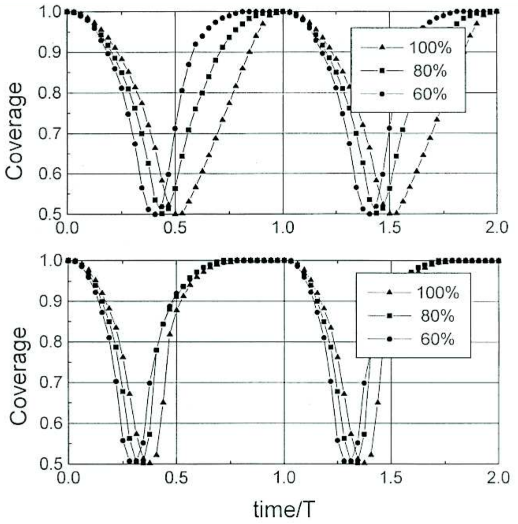

2.24. Fig. The computed oscillation at different incidence angles. The symbols △, □, and ⊙ mean incident angles of 1°, 1.25°, and 1.5°, respectively. The reflected-diffracted information comes from 10, 80 and 60% of the terrace area, respectively. The upper part of the figure shows the case of $r_{\|}/r_{\perp} = 2$ and the lower part shows $r_{\|}/r_{\perp} = 1$.

If we suppose the value 2 as the ratio in the [110] direction, then the ratio 1 corresponds with an 18° deviation from [010] direction (see Fig. 2.23). The calculated oscillations can be seen in Fig. 2.24. Perfect layer-by-layer growth was assumed in the calculation, so only the actual top monolayer was investigated. The calculated function of $t_{3/2}/T$ vs. azimuthal angle the two different directions is shown in Fig. 2.25. The growth time for one complete ML in the two different directions is the same ($T$), but the phase is different ($t_{3/2}$) because of the anisotropic growth rate. These curves correspond with the measured data in Fig. 1. If the SCL is larger than the average terrace width then the $t_{3/2}/T$ ratio remains constant (which constant value is determined by the $r_{\|}/r_{\perp}$ ratio). If the SCL is smaller than the average terrace width, then the $t_{3/2}/T$ ratio decreases, too.

The behaviour of $t_{3/2}/T$ vs. incidence angle was investigated for glancing-incidence-angles, under 1.8°. In real situations, the diffracted-reflected electron beam gets information not only from the topmost ML. A larger incidence angle causes a larger penetration depth. The description of this phenomenon

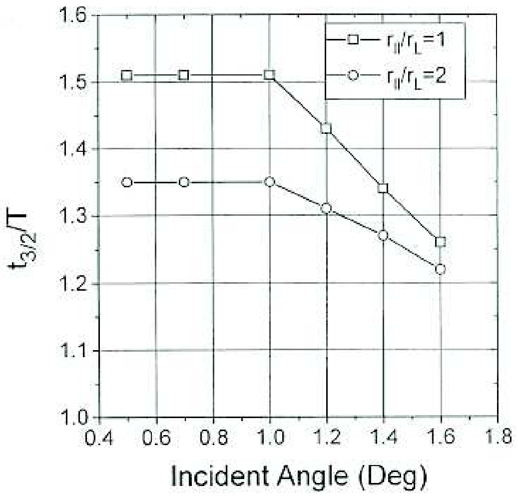

2.25. Fig. The computed $t_{3/2}/T$ ratio vs. incidence angle in different crystallographic directions (in the case of $r_{\|}/r_{\perp} = 2$ and $r_{\|}/r_{\perp} = 1$).

probably can be improved in either range by considering more MLs below the surface during the growth process.

### 2.4.5. RHEED Intensity Dependence on Temperature

In the following we are going to investigate the changes in the behaviour of GaAs and InAs (001) surfaces against temperature variation, based on the experiments of Yamaguhi and Horikoshi [38]. This intensity variation against temperature shows hysteretic properties. During the experiment the change in temperature was slow, so every point could be regarded as being in the state of thermal equilibrium. Shown by the experimental results the temperature dependence of the intensity of the specular spot depends neither on of incident azimuth angles nor on the energy of the electron beam (Fig. 2.26). We can say, therefore, that the intensity change of the specular spot is not the result of diffraction.

The results show that at lower temperature the specular spot intensity is high. As the temperature rises the intensity gradually diminishes. Both in the case of GaAs and InAs the surface at lower temperature shows arsenic-terminated $(2 \times 4)$ surface reconstruction. At higher temperature, however, In/Ga-terminated $(4 \times 2)$ surface reconstruction can be observed. The change

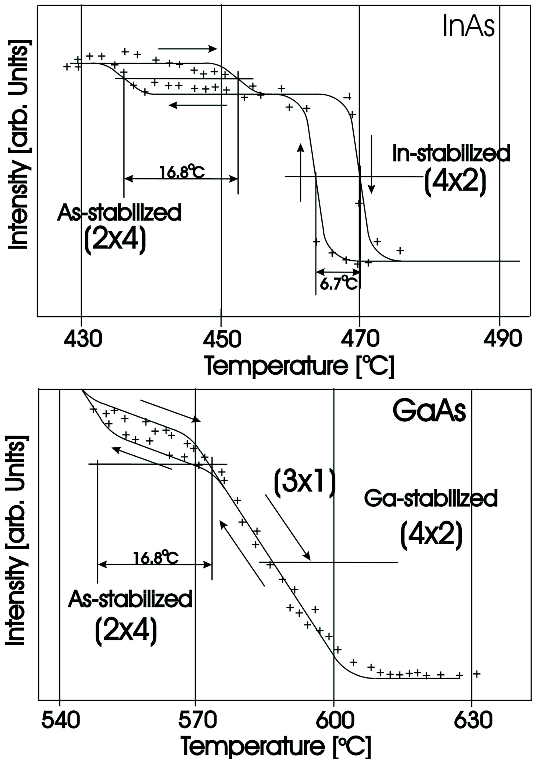

2.26. Fig. Temperature dependence of the specular beam intensity in the case if InAs and GaAs (001) surfaces.

of the direction of the temperature shows, that the process is subject of hysteresis. In the case of both semiconductors the observed hysteresis loops fall within approximately a 50 °C temperature range.

In case of InAs we had two distinct hysteresis loops. At lower temperature the observed wide loop is the indication of smaller intensity variation. At higher temperature however we have seen a narrower loop with large and sudden intensity change. In case of GaAs there is only one real loop at lower temperature and a supposed degenerate pseudo loop at higher temperature. In the second loop the ascending and the descending branches seemingly overlap.

We will apply the general description of the phenomenon to both materials. In our present work we will consider two loops in both cases, giving a qualitative explanation for this inverse spin-valve like, coupled loop structure. For the quantitative investigation we applied the $T(x)$ hyperbolic hysteresis model, developed for a general description of hysteretic phenomena [117].

In the case of diffraction the specular spot intensity would depend on one hand on the surface morphology on the other hand on the surface construction. The reflection from a perfect crystal surface is good, therefore the specular spot intensity is high. A surface with any imperfection disperses the electrons, therefore the specular spot intensity is reduced. The increase in temperature causes primarily arsenic to leave the surface, therefore a perfect surface with high reflectivity is rich in arsenic. Any surface, rich in metallic components, has low reflectivity, disperses the electrons and droplets can also form on it.

Both the InAs and the GaAs crystallize in face-centered-cubic structure, with covalent binding, where four identical binding can form due to $sp^3$-hybridisation. The four equivalent binding represent identical electron distribution in different directions. At the surface the symmetry brakes and the surface relaxes. In case of the arsenic terminated surface, the probability of the presence of the electrons is higher, due to the distorted electron distribution, because of the missing binding, perpendicular to the surface. When the surface is Ge terminated, then the effect is the opposite. The arsenic terminated surface becomes marginally negative, repelling the electrons, making the specular spot intensity higher. When however the surface is In/Ga terminated then the electrons of the incident beam are neutralized and the specular spot intensity is reduced [123]. The composition and also the morphology of the surface is linked to the surface reconstruction and this reconstruction is the function of the temperature as well as the arsenic pressure. The various reconstructions are periodically roughing up the surface in Fig. 2.27.

As we said before, the spot intensity change versus temperature shows hysteretic properties. The change in stoichiometry is the result of the ongoing absorption and desorption processes and these processes are generally regarded as hysteretic. The surface reconstruction is non-uniform and a number of similar processes could be acting simultaneously, forming domain like structures on the surface. Any exchange between them in shapes and sizes can also be the cause of hysteresis. The increasing temperature shall start the migration of the crystal constituents, leading to increased roughness of the surface. Because the sticking coefficients of the metallic components are close to unity, the migration of arsenic is expected when the temperature is increased. The arsenic incorporation takes three stages. The first step is the physisorption of the arsenic species, followed by the dimeralization of the

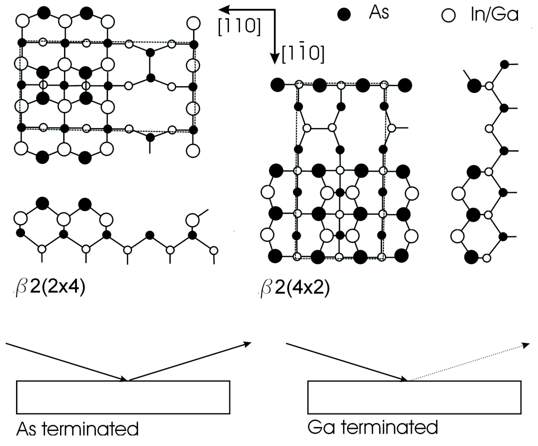

2.27. Fig. The surface reconstructions in arsenic rich and in Ga rich case. The relation between specular spot intensity and reconstruction. The reconstructed surface shows domain structure.

arsenic to be finally chemisorbed in this form to the surface. The dimers will split at this stage and the arsenic atom will finally be incorporated in the lattice. These processes represent three different energy levels. In our experimental temperature range we only have to deal with the last two processes [39, 40]. The process of incorporation is more complex than the process when the arsenic leaving the substance. Before the arsenic is incorporated, it has to be dimeralized and it also has to find two neighbouring vacant locations on the surface for the dimmer to enable the arsenic atom to set in the surface. When arsenic is leaving the surface the process does not need to follow these conditions, therefore the process becomes simpler. As a result the two processes follow two different paths [123].

The surface behaviour is different from that of the bulk material, because due to the energy minimalization, during relaxation, it forms various surface reconstructions [10, 55, 63, 64, 118]. These reconstructions, depending on the temperature and the flux of the components present, result in very complicated phase-diagrams. Each of the $I(T)$ graphs is composed of two hystetesis loops (in case of the GaAs we assume that the second loop is degenerate) (Fig. 2.28).

We can conclude from the model, that each of the loops describe one of the separate processes and that these processes are coupled. An inverse spin-valve shows similar character. The loop at lower temperature belongs to

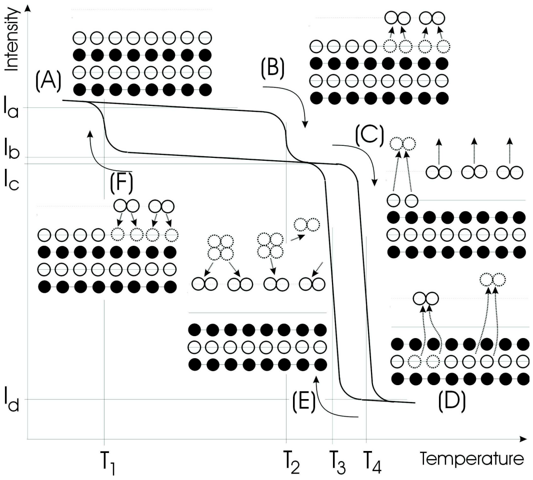

2.28. Fig. The qualitative explanation of the hysteresis in the case of InAs with absorption-desorption processes.

higher intensity, therefore it describes a process associated with arsenic-rich surfaces. In both cases the RHEED indicates $(2 \times 4)$ surface reconstruction in this region. On the surfaces without reconstruction the dangling bonds are pointing in $[1\bar{1}0]$ direction, that forces the lines of the arsenic-rich reconstructions running in the same directions. This surface symmetry can be formed by a number of reconstructions such as: $\alpha(2\times4)$, $\alpha2(2\times4)$, $\beta(2\times4)$, $\beta2(2\times4)$, $\beta3(2\times4)$, $\gamma(2\times4)$. These domain transformations could cause the hysteresis. The energy levels of these domains are very close to one another. At lower temperature first the arsenic-rich $\beta2(2\times4)$ reconstruction will take place, followed by the formations of the domains less rich in arsenic such as $\alpha(2\times4)$ and $\alpha2(2\times4)$. The $\beta2(2\times4)$ reconstructions are more stable, than the ones listed above, therefore they will last longer. They will only transform at higher temperature and than at a faster rate. This represents the upper part of the hysteresis loop. With lowering the temperature, first the reconstructions, of less arsenic content will form. Domains of $\beta2(2\times4)$ reconstruction will start forming at an appropriate temperature, but they will rapidly dominate the surface due to their favourable construction. The intensity curve therefore will follow another path, which forms the lower hysteresis loop. We can conclude that the transformations are governed not only by the change in the temperature but also the phase transitions and the delay in their excitations.

The upper parts of Fig. 2.29. A and B depict the coupled nature of the process and the complex functional relationship between the main and the constituent loops for InAs and GaAs respectively. It also shows the relative contributions of the various surface effects to the specular spot intensity variations.

The various surface reconstructions are associated with different stoichiometry, which are linked to the RHEED intensity [119]. Although a large volume of information is available on the subject of surface construction, the temperature effect and growth, the comprehensive and consistent explanation is still awaited for. It is obvious, from what we said before, that the connection between the surface roughness and the RHEED intensity is only part of the truth. The surface producing maximum intensity is far from perfect due to the process of relaxation, although the surface stoichiometry is changing continuously. The arsenic-rich crystal surface produces higher RHEED specular spot intensity against the lower intensity surface, rich in In/Ga. This assumption is supported by the phenomenon observed at droplet epitaxial formation as well, which shows that the arsenic-rich stripy RHEED picture becomes diffused, when the atoms in the Ga beam combine with the arsenic atoms and by absorbing them the result is the presence of Ga atoms on the surface [120, 206].

The phenomenon of hysteresis in many fields of science is well known and well documented in the literature. The spin-valve and later the inverse spin-valve effect, as part of the hysteretic processes have only been discovered less than ten years ago. Although the phenomenon described in this paper is far removed from the physical mechanism of spin-valves, its general character is strikingly similar. In general terms, the spin-valve effect involves two coupled hysteretic processes and characterized by two hysteresis loops flowing into each other as the excitation varies periodically. Although there are a number of known models for describing hysteresis, so far there is only one, the $T(x)$ hyperbolic model, which can describe this rather complex phenomenon of two coupled hysteretic processes, like in a spin-valve [121]. The model is based on the Langevin's theory of ferromagnetism. The independent constituent components are identified and formulated by their separate hyperbolic functions ($A_n f_n$, $n = 4$, An amplitude, $f_n$ same functions with different numerical parameters) and linearly superimposed by using Maxwell's superposition principle [14]. The loop, predicted by the model, gives a good fit to the measured specular spot intensity versus temperature $I(T)$ curve as shown in Fig. 2 A and B for GaAs and InAs respectively. Although the

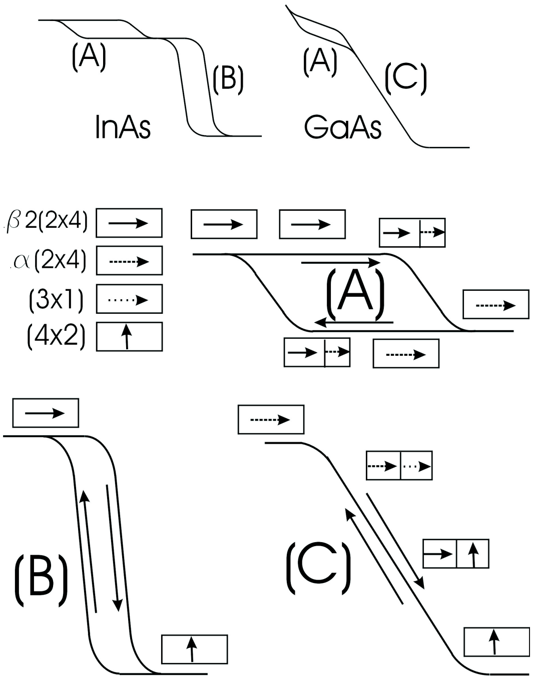

2.29. Fig. The qualitative explanation of the hysteresis for InAs and GaAs with the changing of domain-like areas with various surface reconstructions.

model predicts the presence of a very narrow loop in the InAs intensity plot at higher temperature as well, its width is probably within the experimental error. It is interesting to note, that while the physical parameters used in modeling are different for the two substances the approximate ratios between the amplitudes ($A_n$) remained nearly the same. This is a good indication that with the changing temperature the surface reaction is the same for the two experimental substances as we have initially assumed.

This first successful modeling of the phenomenon has far reaching implications. The model predicts that, there are two separable, simultaneous coupled processes taking place on the surface of both the GaAs and InAs crystals, at a given time. In one temperature cycle, both cases the up and down processes can be represented by two single simultaneous physical processes. The two simultaneous coupled processes are surface morphology and surface stoichiometry. Each of the four processes is represented by one separate function in the model. In the phase of up-going temperature the dominant

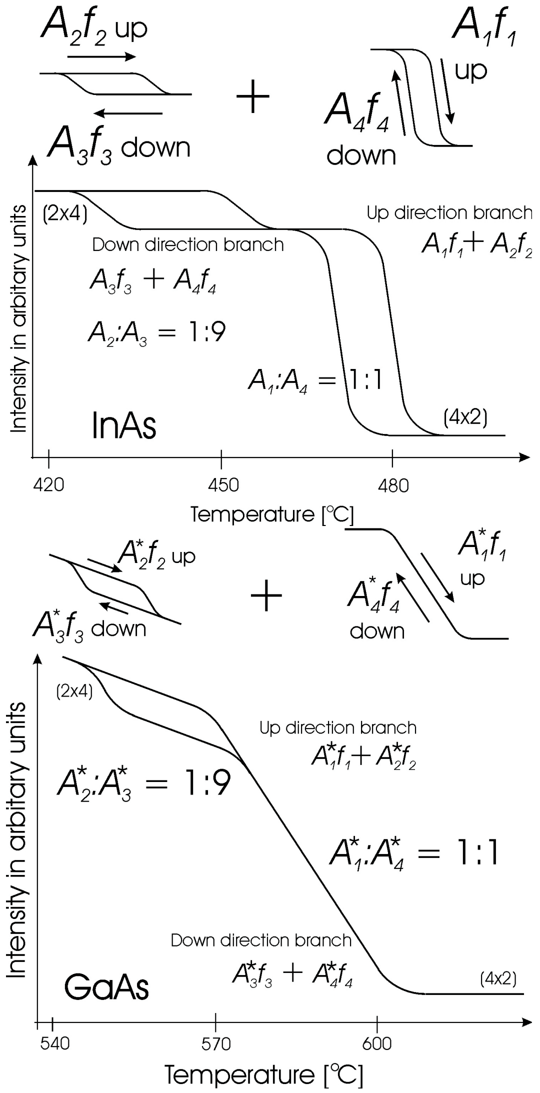

2.30. Fig. Two consistent hysteresis loops of $I(T)$ curve for InAs and GaAs.

process is stoichiometric, representing approximately 90% of the RHEED intensity changes. The rest 10% is due to the morphologic changes. When the temperature is decreasing however, the contribution of the two processes are equal (50%-50%). This finding fortifies the physical explanation given before and the results of the RHEED studies on GaAs and InAs. While, at higher temperature, the As can leave the surface with relative ease, at lower temperature the surface reconstruction with the As capture, involves complex timely processes, as described earlier. The model also leads to the calculation of the activation energy involved in the absorption/desorption processes. Following Boltzman's relations the $\varepsilon$ activation energy involved in each leg of the hysteresis loop can be calculated as $\varepsilon = \alpha t k T$, where $\alpha$ is the inclination of the leg of the loop in $K^{-1}$, representative of the speed of the process or reaction at $t$ temperature (in K). $k$ is the Boltzman constant and $T$ is the mid temperature of the processes in K [38, 121]. Detailed model interpretation and mathematical formulation of this surface phenomenon is outside the scope of this paper, because its limited size, that will be published elsewhere in full [123].

### 2.4.6. Evaluation of the RHEED Sign

The relation between the growth front and the connected RHEED pattern is very complicated. It is important to track the temporal metamorphosis of the RHEED pattern. The grown structure is influenced strongly by the surface reconstruction. In the initial stage of the sample preparation, simple layer is grown. The number of the mono layers is determined with the help of intensity oscillation of a RHEED spot.

The position of the observed RHEED spot can be changed during the growth process (Fig. 2.31.). Here, a computer program was developed for the tracking and the intensity measurement of the RHEED spot. The program is written in $C^{++}$ language. In the case of the investigation in the given point, we start the searching algorithm. After the start, pick out the potentiale spots with the help of the gradient change. The permission of the spot tracking is initialized with the manual selection of a spot. So we can investigate the spot intensity vs. time.

The RHEED pattern change during the growth of the nano-structure. We have to determine the growth kinetics from the pattern change. The pattern consists from streaks, from points etc. We need the knowledge of the metamorphosis of each pattern.

We developed a computer program to recognize these metamorposies. With this program the dynamic RHEED (in-situ and also videos) are easy to be observed and analysed. There are two possibile ways, each one is coloured in false colour to improve the readibility of the RHEED intensity information Fig. 2.32. The first way is to represent the data in 2D, after the threshold cutting. The second way is a 3D representation, which makes the intensity

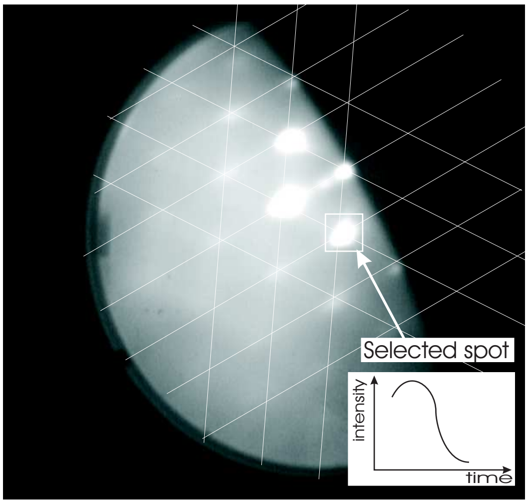

2.31. Fig. A snapshot of the RHEED pattern during the QD evolution. This is the pattren which is investigated with image processing.

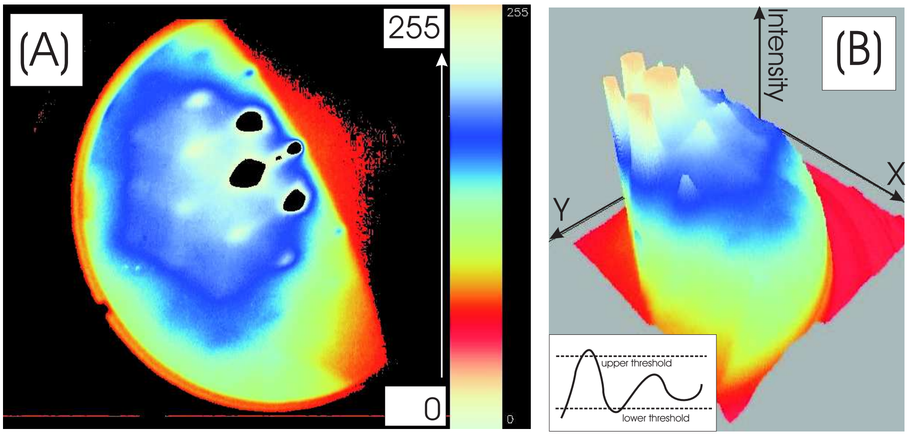

2.32. Fig. RHEED image after image processing. (A): Intensity after crop (see insert). (B): the same in three dimension. the intensity relations are recognizable.

around the envolved shapes more easy to observe. Both could be saved in JPG for further analysis. The program is written in C++ and uses OpenCV for image processing, and OpenGL for the 3D imaging [83, 123].

# 3. Chapter

# Two-dimensional Structures

## 3.1. Growth of InGaAs/GaAs Layer Structures

### 3.1.1. Strained and Unstrained Junctions

Since the seventies, because of the very precise control of layer thickness is one of the main advantages of the MBE, the study of interface structures and their influence on device parameters has stayed in the mainstream of MBE research since the initial proposal of semiconductor super-lattices and quantum wells. A two-dimensional structure that is a sole quantum well consists of two heterojunctions. The structure that arises when two different semiconductor crystals are jointed together is called heterojunction. The crystal potential and consequently the electronic structure of each constituent semiconductor remains unchanged that is bulk-like right up to the interface plane, where it changes abruptly into bulk properties of the other semiconductor. In particular, the interfacial atomic configuration of lattice matched (unstrained) AlGaAs/GaAs heterostructures has played an important role in the development of modern semiconductor physics and in the progress of advanced device concepts, since this materials system is commonly used as a model system for fundamental studies of lattice matched heteroepitaxy.

InGaAs/GaAs heteroepitaxy has a great importance not only in the fabrication of semiconductor devices but this is as a good model structure for the investigation of the strained layer growth. The critical layer thickness (CLT) in the heteroepitaxy was investigated experimentally as well as theoretically [126]. Under real growth circumstances the measured CLT depends not only on misfit but on the growth parameters, too [127]. The best in-situ way to monitor MBE deposition is the RHEED. The lattice mismatch also effects the behaviour of RHEED oscillations. The oscillation amplitude decreases rapidly during the InGaAs growth due to its strong dependence in InAs mole fraction. This decrease also indicates the formation of the tree-dimensional growth mode.

### 3.1.2. Technological Preliminaries of InGaAs/GaAs Heterojunction

In our experiment, the growth of InGaAs layers on GaAs (001) substrate was carried out by MBE at 490 °C deposition temperature. In this case, the accurate intensity of RHEED oscillations was measured directly by means of high resolution Faraday cup. The growth rate and the composition were determined by the help of RHEED oscillation while the composition ranged between $x = 0$ and 0.4. The composition change was caused by the increase of In flux, while the other technological parameters remained unchanged.

The magnitude of intensity oscillations continuously decreases during the growth process. With the Increase of In composition not only the growth rate becomes faster but the decay of oscillations, too. We have investigated the decay of amplitude oscillations (peak-to-peak). The least-squares method was used to fit an exponential function to the experimental intensity decay data, where $\tau_d$ is a decay time constant and $A_0$ a fitting factor. The measured decay fits very well to an exponential function with the only exception of the first period. This description for $I(t)$ is valid for all $x$ values in the investigated range (0 - 0.4) [48, 128]. With increasing composition $x$ the decay time $\tau_d$ decreases. The measured value of the decay time constant is a function of composition $\tau_d(x)$, where the exponential function was fitted by the least-squares method. The fitted function is $\tau_d = a\exp(-x/b) + c$, where the parameters in our case are $a = 24.85$, $b = 0.103$ and $c = 4.1$ [128].

### 3.1.3. Technological Preliminaries of Thick InGaAs Layers

The GaAs wafers used in the experiment are Zn doped ($p = 4 \times 10^{18}$ cm$^{-3}$) with (001) orientation and etch pit density (EPD) $< 5 \times 10^4$ cm$^{-2}$. Prior to growth the surface was bombarded by 30 mA argon ion beam to remove the damaged layer. Then an undoped GaAs buffer layer was grown to improve the morphology of the surface. This was followed by the undoped InGaAs layer which varied in composition from sample to sample. The variation in composition was induced by varying the temperature of the In source, between 470 and 570 °C. The other parametes during this process were kept constant. The substrate and the Ga source temperature was 490 and 925 °C, respectively. The arsenic pressure in the recipient was about $7 \times 10^{-5}$ Pa during the growth process. The layer composition, the growth mode and the growth rate was monitored by RHEED. The growth rate, which is about 0.6 $\mu$m/h, depends on the In content. The In content was between 3 and 30% and the layer thickness varied between 0.02 and 5 $\mu$m. By using electrochemical etching we found that the undoped layers were of slightly p-type. We investigated two samples in details: sample $A$, 1.2 $\mu$m, In content 30% and sample $B$ 3.2 $\mu$m, composition 3%. Were the lattice misfit are $f$ = 0.024 and 0.0024, respectively.The Matthews-Blakeslee (equilibrium) CLT for the misfit generating dislocation [126] is about 8 nm and 800 nm for samples $A$ and $B$, respectively, that is to say our layers are much thicker than the CLT.

## 3.2. The RHEED and the Critical Layer Thickness

### 3.2.1. Separation of the Part Processes

The measured values of the deading time constants depend on the composition. Most probably there is a relationship between the behaviour of the RHEED oscillation decay and CLT. The decay of oscillation amplitude exists even without mismatch, e.g. at pure GaAs layer growth. Changes of the In content modify not only the mismatch but the conditions of growth (e.g. growth rate), as well. Therefore, the misfit and the technological parameters have a joint influence on the behaviour of amplitude decay. The exponential function is a good approximation of the $I(t)$ function at every $x$ values. Provided that both processes are independent from each other, the phenomenon of decay at arbitrary $x$ values can be described by two time constants as follows:

$$I(t) = A_0 \exp(-t/\tau_d) = A_0 \exp(-t/\tau_M - t/\tau_G) \tag{3.1}$$

where $\tau_M$ and $\tau_G$ are the assumed time constants of the separed part effects which are responsible for the influence of misfit and the growth, respectively. According to this model, the $x$ dependent decay from misfit can be written as follows:

$$1/\tau_M(x) = 1/\tau_d(x) - e(x) \tag{3.2}$$

where $\tau_d(x)$ and $\tau_M(x)$ time constants are functions of the composition $x$, and the $e(x)$ term contains the dependence from deading constants. In the case of pure GaAs growth ($x = 0$), there is no caused by misfit. It means that at $x = 0$, the reciprocal value of the decay time constant originates entirely from crystal growth phenomenon. Function $\tau_d(x)$ is known. The value of $1/\tau_M$ at $x = 0$ is zero. As a first approximation, we can neglected the $x$ dependence of negative part in Eq.(3.2.), so the $1/\tau_M$ function describing the mismatch can be obtained by moving the $1/\tau_d$ function in negative ordinate direction (Fig). We can easily determine the $\tau_M(x)$ function from its reciprocal form. In order to be able to compare the calculated decay with the theoretical CLT, we should change to layer thickness instead of period time because now we have only function of time vs. $x$ [131].

### 3.2.2. Comparison with the Matthews Model

The grown thickness under one period of oscillation is one monolayer which corresponds to half of the lattice parameter. After evaluating the function of thickness vs. $x$ instead of the function of time, we can compare the calculated threshold thickness with the theoretical CLT. As it can be seen from Fig., there is a relatively good agreement between our calculation and the isotropic and anisotropic Matthews model [129].

As a first approximation, it was supposed that the dependence of $1/\tau_G$ on the composition $x$ is not significant, i.e. the second term in Eq. (3.2.)2 is constant. Although, we have received similar course between the theoretical CLT and our calculated threshold layer thickness, one can find difference between curves as well. The reason of the deviance can be in the fact that the $\tau_G$ also depends on the composition.

We can investigate the technological influence in the case of pure GaAs growth. We can increase the growth rate by increasing of the Ga flux. Let us see an example. At the Ga source temperature of 935 °C the growth rate is 490 $r = 3.85$ s$^{-1}$ ($\tau_{GaAs} = 2.61$ s) [128]. In this case, the decay

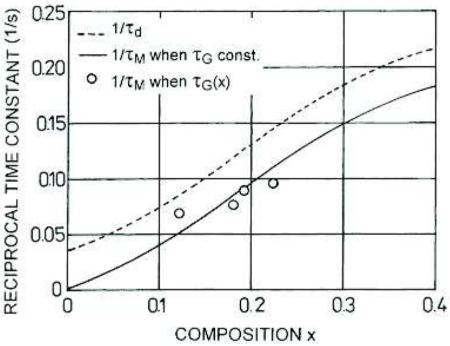

3.1. Fig. Reciprocal function of deading time constant, where the curve of $\tau_d$, $\tau_M$ and some values of $\tau_G$ are depicted.

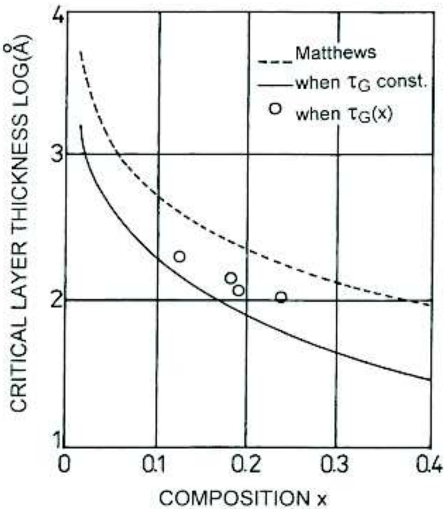

3.2. Fig. Threshold layer thickness calculated by us is compared by Matthews model, where also some corrected data are depicted, which originated from taking into account of technological influence.

of oscillation can be described with decay constant $\tau_d = 15.3$ s, where - because of the homoepitaxy - $\tau_M$ is missing therefore $\tau_d$ and $\tau_G$ are equal. The above mentioned growth rate corresponds to the case of InGaAs growth ($\tau_{InGaAs} = 2.61s$), $x = 0.13$, (where $T_{Ga} = 925$ °C and $T_{In} = 540$ °C). With the increase of the growth rate the decay constant decreases. In the case of InGaAs growth, the increase of growth rate means simultaneous increase of

InAs mole fraction, too. The more pronounced decay of oscillation can be traced back not only to the change of growth rate but to change in the In content as well. The course of RHEED intensity oscillations depends strongly on the observed material. The observed oscillation is weaker and has larger decay in the case of InAs growth on InAs (001) than in the case of GaAs homoepitaxy under similar growth conditions [48]. The change of $\tau_G$ can be caused by the change of growth rate and/or change of In/Ga ratio. The supposed tendency of $\tau_d$ is supported by both above mentioned phenomena. We can find further data of pure GaAs growth with different growth rate which can be fitted to the corresponding $x$ compositions in InGaAs, where the growth parameters are kept as far as possible the same. The values marked in Fig. 3.1. The threshold thickness is defined as the thickness where the oscillation becomes weak enough as it was determined earlier [128, 131] and is depicted in Fig. 3.2. The supposed dependence of $\tau_G$ on the growth rate/composition seems valid because the deviance between CLT and the calculated data becomes less. The growth rate dependence was proved in the case of InGaAs growth by in-situ XRD measurement where the deposition temperature was 490 °C (the same as in our case) [130]. More detalis can be found in Refs. [131, 221]. The concept is valid for growth of low temperature GaAs [137, 139].

## 3.3. Layer Structures over CLT

### 3.3.1. The Measuring Set-up and the ex-situ Investigation

The InGaAs/GaAs layer structure was ex-situ investigated by electrochemical method. The arrangement of our electrochemical measuring set-up is often used in electrochemical investigations. The working electrode is the semiconductor sample, the counter electrode made from carbon and the reference electrode is a saturated calomel electrode [143]. The sample is held against a rubber ring seal of 3 mm diameter. The morphology of the etched surface was studied by SEM in secondary electron imaging mode. The removed layer thickness was calculated by Faraday´s law [144] and measured by a surface stylus profiler. As we were unable to carry out in-situ EPD measurement with our present set-up, each measurement was taken on a separate part of the samples. Any large-scale lateral inhomogenity could cause an error in the measurement. The EPD values determined on the surface area of about 1 $mm^2$.

The etching parameters (electrolyte and bias voltage) were optimized by using a bare GaAs substrate. We tried three aqueous electrolytes: (i) 10% $NH_4OH$; (ii) 5% $H_2SO_4$; and (iii) 0.5M HCl. The $NH_4OH$ was the only electrolyte suitable for defect etching. The other two electrolytes resulted in precipitates on the surface. Besides the type of electrolyte, the surface morphology also depends on the bias voltage. After etching, the surface is well structured when larger than 0.5 V anodic bias (defect etch condition) is applied. At lower bias voltage, the surface remains mirror-like (polish etch condition). The etching current, when the bias ranges between 0.5 and 0.8 V is stable, i.e. increases only slowly with depth (or time). The etching current is large at higher doping in this bias range, and the etch rate is low. In this range we can remove thick layers and detect the location of the etched surface relative to interface or substrate. At an anodic bias larger than 1 V the etching current becomes unstable and increases strongly with time (or depth). In this etching current range for the undoped layer is larger than for the bare substrate. The $I(V)$ characteristics are depicted in Fig. 3.3. The slope of $I(V)$ characteristics of the epitaxial layer, above 0.5 V bias, is larger than the slope of that of the substrate. This can be explained by the presence of defects. At higher EPD, the current vs. time (or depth) is steeper, because at higher bias voltage, current filaments are formed t the imperfections [145].

Based on these results, we carried out the defect etching at about 0.6 V bias, where the current density was less than 2 $mA/cm^2$. Prior to studying the substrate, the damaged surface layer was removed by non-selective etching (for first step of etching see upper part of Fig. 3.3.). The position o the interface is indicated by current vs. depth function. The current density has a sudden increment at the interface, because of the substrate has higher charge concentration than the epitaxial layer (see Fig. 3.3). Related publications to be found in Refs. [151, 152, 154, 156, 158, 161, 165, 167].

### 3.3.2. Threading Dislocations in the Layer

Typical SEM pictures of the surface morphology of the bare substrate and for sample $A$ and $B$ are shown in Fig. 3.3. The measured EPD of the substrate was half of the value specified by the supplier. The substrate defect density was found to be non-uniform: The average separation between two

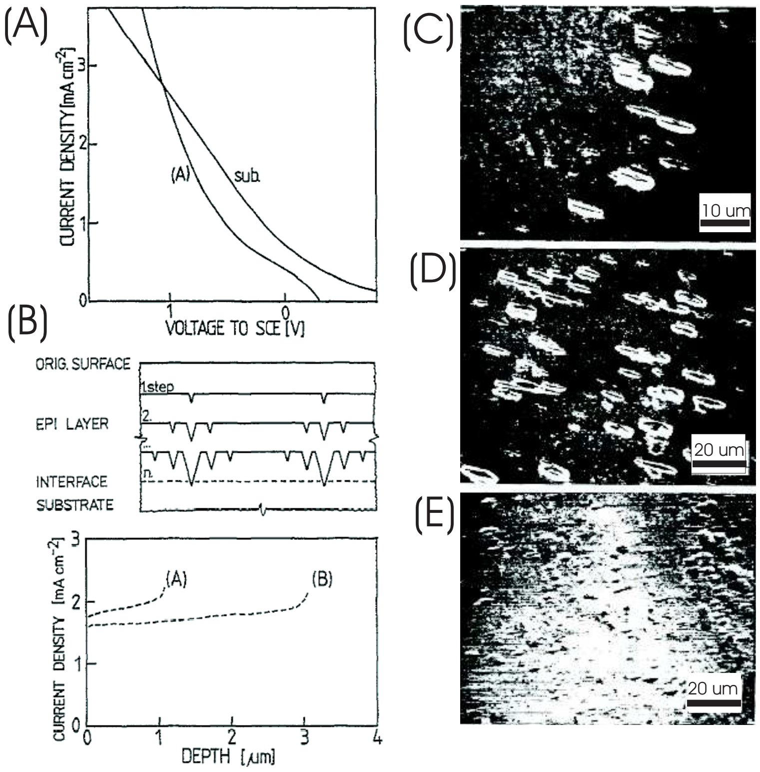

3.3. Fig. (A): $I-V$ curves of p-type GaAs substrate and sample $A$ using the $NH_4OH$-based electrolyte; (B): upper part, stepped etching. The step of the removed layer thickness must be larger than 0.5 $\mu$m (see text), lower part, the current density of anodic dissolution vs. depth; (C),(D),(E) show SEM micrographs of etched surfaces; (C): bare substrate, EPD is about $2 \times 10^4$ cm$^{-2}$; (D): sample $A$, at 0.7 $\mu$m from the interface, EPD is about $2 \times 10^8$ cm$^{-2}$; (E): sample $B$, at 0.9 $\mu$m from the interface, EPD is about $10^7$ cm$^{-2}$.

adjacent week maxima of the defect bunches was found to be typically 80 and 200 $\mu$m for the samples $A$ and $B$, respectively. Similar, but weaker non-uniformity was present in the epitaxial layers. For sample $A$, the bounch distance was between 30 and 45 $\mu$m. This indicates that the dislocations in the epitaxial layer originate also from sources other then the grown-in dislocations of the substrate. We further note of the non-uniform distribution threading dislocation is inherent to the mismatched systems. The size of etch pits are different; larger pits indicate dislocations traveling further from the interface; this is an indirect evidence for the depth inhomogenity of the defect density. The elongated shape of the pits is due to the higher etch rate along one of the ⟨011⟩ axes.

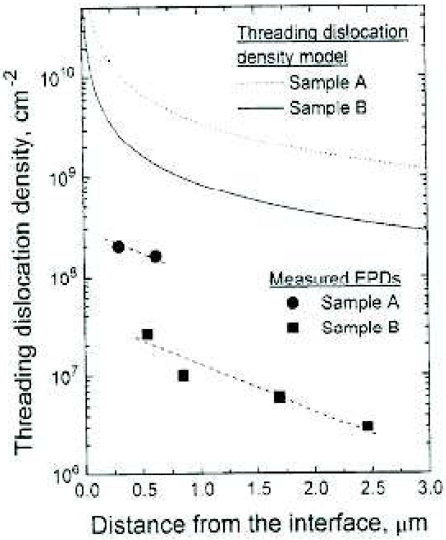

3.4. Fig. EPD as the function of etched depth for our samples, together with model calculations. The lines serve only as guides to eye.

Several theoretical model have been worked out to predict the threading dislocation density $D$ in mismatched heteroepitaxial system. Ayer´s glide model appears to be the closest to the physical base. Furthermore this model uses no fitting parameters [146]. This model assumes that $D$ is set by the equilibrium between the line tension of the dislocations misfit segment and by the attractive force between two adjacent threading segments. The calculated $D$ for (100) system with 60° dislocations is [146]:

$$D = \frac{f\sqrt{2/3}}{4hb}\left(\frac{1}{4} + \frac{3}{16(1-\nu)}\right)\ln\frac{1}{8f} \tag{3.3}$$

where $b$ is the Burgers vector length ($b = 4$ nm), $h$ is the layer thickness and $\nu$ is the Poisson ratio ($\nu = 0.32$) and $f$ is the value of the misfit. The measured EPD values vs. etched depth are shown in Fig. 3.4, together with those predicted by the model. Although the difference between the model and our measurements is striking, the overall $h$ and $f$ dependence agrees well. (We note that the other models also predict a $1/h$ and $f\ \ln(1/f)$ type dependence [146]). This discrepancy may have several reasons. First, it has been reported that EPD measurements underestimate the real dislocation density [147]. Second, the possible effects may stem from the depth dependence of the dislocation density, i.e. the dislocations that terminate close to the actual etched surface may yield pits that are too small to be observed. The removed layer thickness must be larger than 0.5 $\mu$m to get an evaluable surface morphology [142]. Thus, we have shift the measured EPD points by at least 0.5 $\mu$m in our curve in order to measure the EPD of actual surface (see in Fig. 3.3).

The main cause is probably due to the limitations of the equilibrium glide model. The model implicitly assumes that initially there are enough number of threading dislocation sources in the system. Thus, i the number of the threading dislocations is limited, what is typical in small-misfit systems, the threading dislocation density might be smaller than the equilibrium one. In addition, increasing of the annihilation rate due to the inplane anisotropy [148] may further decrease the treading dislocation density.

Dense furrows (density, few lines/$\mu$m), running parallel to the elongated etch pits, were observed in sample (A) at about 0.5 $\mu$m from the heterojunction. The furrows are caused by preferential etching due to the periodic strain field of the misfit dislocation network. Crosshatch pattern, which is typical in systems with moderate misfit [149], is not observed in our samples.

# 4. Chapter

# One-dimensional Structures

## 4.1. Growth of Nano-wires

The one-dimensional nano-structures that is the nano-wires have recently attracted intensive interest due to their potential application to semiconductor electronic, optoelectronic, and biosensing devices. Nano-wires, which are structures confined in two dimensions $\mu$m long and with diameters in range 1 - 200 nm. There are two common kinds of nano-wires. One of them is the laterally aligned nano-wires which can be grown like as vertically propagating super-lattice [2]. The another ones are the vertically aligned structure, which can be grown by metal-induced method (Fig. 4.1.).

As an example the polymer-based solar cells can be mentioned, their efficacy can be as high as 5% due to the applied nano-structures [10, 11]. This huge increment in the efficiency made this type of solar cells turn from technical curiosity to a cheap competitor of the present devices.

Nano-wires have gained a lot of attention over the past decade due to their unique geometry and mechanical, electrical and optical properties. Nano-wires can be grown from several materials upon various substrates by many technologies. They can be prepared e.g. by molecular beam epitaxy [176], evaporation technique [177], laser ablation [178], aqueous chemical growth [179], vapor phase growth [180]. Ususally, the different types of nano-wires correspond to different growing methods, however some materials can build nano scale wires via multiple technologies. The compositional variation within these nano-structures also plays a crucial role in governing their electronic band structure. In this paper, we are dealing with nano-wires which were grown by the metal induced manner in an evacuated chamber on GaAs and InP substrates. The growth occurs from the gaseous phase, where the mechanism can be explained by the vapor-liquid-solid model in the presence of Au catalyst particles [181].

## 4.2. Some Remarks to the Nano-wires Grown on III-V Substrate

### 4.2.1. Preparational Preliminaries and Investigations

In our experiment, the nano-wires were synthesized on GaAs and InP (001) surfaces. After the cleaning of the surfaces, 50 nm thick Au layer was deposited by sputtering method on both crystals. Each samples were closed in separate silica ampoules, which were evacuated to $10^{-3}$ Torr. The heating and the annealing of the samples inside of the ampoules ranged between 300 - 700 °C. After a rapid heating, subsequent annealing was carried out on the samples. The annealing times were 1, 10, 30 and 60 min. During the thermal treatment (550 - 700 °C) first the continuous Au layer changed to fractal like clusters. In the next step of the heat treatment (350 - 450 °C) the nano-wires were growing. All samples undergone similar processing. The samples were opened after cooling them to room temperature. Detailed description of the growth technology can be find in Ref. [182, 183].

The samples were investigated by scanning electron microscopy (SEM) and transmission electron microscopy (TEM). Furthermore, energy dispersive X-ray spectroscopy (EDS), ultrahigh resolution TEM and selected area electron diffraction (SAED) were carried out with the same TEM equipment. Detailed description about these investigations can be read in Ref. [182]. The SEM measurements were made by an LEO 1540 XB system. For analyzing the samples we have applied 10 keV energy beam. The studies on the changes due to the diameter variance of the wires were carried out by 5 and 20 keV primer energy electrons. In our case, the working distance was 5 mm.

### 4.2.2. Composition of the Nano-wires

The composition and the crystallinity of the nano-wires were determined by EDS and SAED methods, respectively. The SAED analysis showed that the nano-wires had crystalline structure. In the case of InP substrate, according

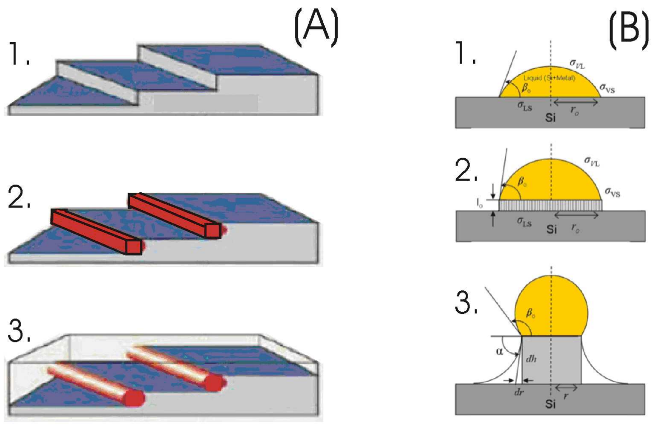

4.1. Fig. (A) horizontally aligned nano-wires (grown by vertically propagating-like super-lattices); (B) vertically aligned nano-wires (grown by metal-induced method).

to the EDS spectrum, the wire consists of indium and phosphorus. In the case of GaAs substrate the situation is entirely different, although the growth technology in both cases was the same, $Ga_2O_3$ nano-wires and $As_xO_y$ nano-tubes arouse. The reason of the difference can be find in the reactivity of the growth components.

The growing processes took place in a $10^{-3}$ Torr evacuated ampoule, which is a relatively weak vacuum. The residual gas contains both oxygen and water. The kinetics of the growth process of the nano-objects are not fully known, however, the state of the surface before the thermal treatment is probably a determining factor. The remaining gas in the ampoules can also affect the growth.

First, let us study the case of the GaAs substrate. As it is well known, the GaAs oxidize easily, and the oxides dissolve only above 582 °C [183]. In the growing method applied by us the thermal treatment is well below this temperature, thus the oxidized surface takes part in the growth process, it does not dissolve previously. According to these arguments, no pure GaAs nano-wires can be produced. On non-oxidized surface clean GaAs nano-wires grow [185], while if the surface is oxidized, the nano-objects are built from the components' oxides.

In case of the InP substrate, because of the similar technology, the composition of remaining gas is the same. The nano-wire grows from the gas phase. During the heat treatment phosphorous releases from the substrate, which is, as it is well known, oxidized quickly. The oxide of the phosphorous adsorbs water, and at higher temperatures these processes are more intensive. These reactions take place as long as the oxygen is present at the small ampoule, afterwards the nano-wires grow upon clean InP surface.

### 4.2.3. The Change of the Diameter of the Nano-wire

During the SEM studies an interesting phenomenon attracted our attention. The diameter of the nano-wires changed due to electron irradiation. We have exposed InP nano-wires of two different diameters to radiation of two energies. The resulting diameter changes are summarized in Table 1. Usually the thickness of the wires decreases as an effect of the irradiation. A typical SEM picture of a decreased diameter is shown in Fig. 4.2.

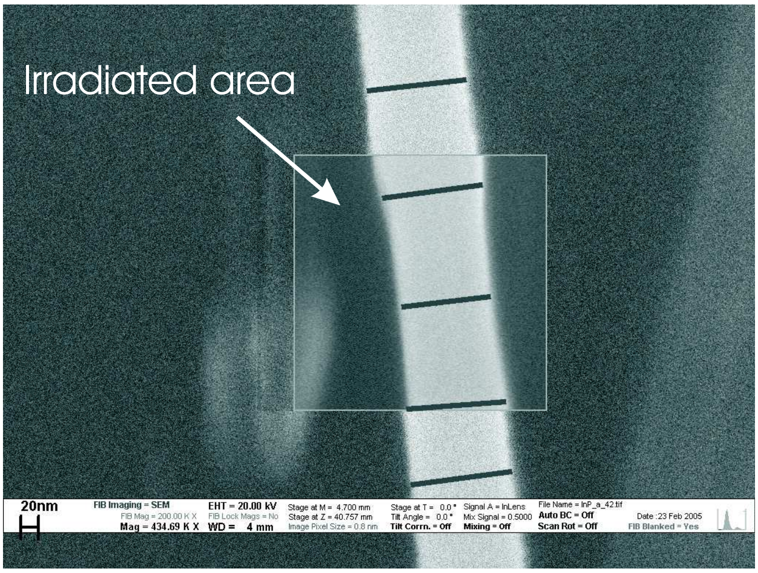

4.2. Fig. Typical change of the diameter of the nano-wire after the 20 keV electron irradiation.

According to our experiences the crystalline nano-wires usually adopt the crystal structure of the substrate [184, 185, 186, 187]. In case of slow growth the whole nano-wire takes this structure, which is, in our case, a zinc blende (001) structure in the direction of the axis of the nano-wire.

In the nano-wire the structure taken from the bulk crystal is distorted compared to the ideal one. Due to the large surface, the position of the atoms and bonds changes. M. Bukala et al. carried out a simulation for studying the stability of nano-wires for various crystalline structures [188] The analyzed structures were zinc blende (001), (111), (110) and wurzite(0001) axis nano-wires. They have found the wurzite (0001) to be the most stable state and the zinc blende (001) the least stable one.

We ascribe the diameter variance to crystal structure changes. If larger energy then a given threshold is transmitted to the crystalline nano-wire, it acquires a more stable state instead of the original one. The influence of the neighboring crystalline wires is negligible due to the thin geometry. Quick energy transport results in quick restructurization.

In case of same diameters, the wurzite (0001) axis nano-wires consist of 2/3 times more atoms in the plane normal to the axis then the zinc blende (001). If the structure changes, the number of atoms do not increase, thus the diameter shrinks. Let us calculate the diameter decrement for the 41 nm nano-wire. The diameter of the wire is proportional to the number of atoms in the cross section. Considering the transformation zinc blende (001)/wurzite (0001), the resulting diameter is 32 nm, which is within the error bounds of our measured values. According to our calculation the diameter decrease of the thicker nano-tubes is, of course, smaller. In case of the zinc blende (001)/wurzite (0001) transformation of the 115 nm wire 93 nm is the resulting diameter. The deviation of the calculated and measured diameters is larger in this case, which can be attributed to partial or mixed transformations. In case of mixed transformation, zinc blende (110) and (111) structures, as energetically more favorable ones can come into question. The mixed transformations can account for the diameter expansion. More details can be found in Ref. [174].

# 5. Chapter

# Zero-dimensional Structures

## 5.1. Quantum Dot Grown by MBE

### 5.1.1. The Strain-induced Technology for Quantum Dot Growth

Recently, the growth of self-assembled quantum structures has been intensively investigated for basic physics and device applications. It is very important to understand their growth process and to know their particular shape. The archetypal system of these nano-structures is the lattice-mismatched system such as InAs on GaAs, where the strain-induced process leads to the formation of quantum dot (QD) [266, 267].

As we mentioned before, the structure growth can be classified in three modes. The SK or layer-plus-island mode is an intermediate case between the FM and VW modes. In the case of SK, the lattice mismatch between the grown layer and the substrate material is the most common case. Here, a possible way the deformation energy minimization is to nucleate nano-sized islands on the even layer. This layer is called as wetting layer (WL). The essential driving force for coherent QD formation, after a WL has formed, is strain relaxation, whereby the energy gain from the increase in surface area via dot formation more than compensates the increase in interfacial free energy [271]. The filed of self-organized strain-induced QDs is dominated by two model system, InAs/GaAs (001) and Ge/Si (001). Two families aceted and defect-free islands (pyramids and domes) as well as the transformations that these undergo during the embedding-passivation process are general features.

Under typical deposition conditions, pyramidal islands bounded by shallow (105) facets form spontaneously on WL. They can then undergo transitions into multi faceted dome islands dominated by much steeper (113)facets and bounded also by other facets [168, 169, 171, 170, 172, 173].

Detailed electronic structure of QD, which governs electronic and optical properties, depends on the shape [268, 269] . It is generally accepted, that one of the essential driving forces, for coherent lattice mismatched QD formation, is strain relaxation [271].

### 5.1.2. Droplet Epitaxial Technology for Production of Different Nano-structures

In this field, the self-assembled lattice matched quantum structures, employing droplet epitaxy, is an interesting and novel alternative for the the estabilished technology of strain-driven QD formation [272, 273]. Today, no theoretical description is available for the underlaying growth mechanism, the development of the facetting, in the case of droplet epitaxy. It is very important to understand the growth kinetics.

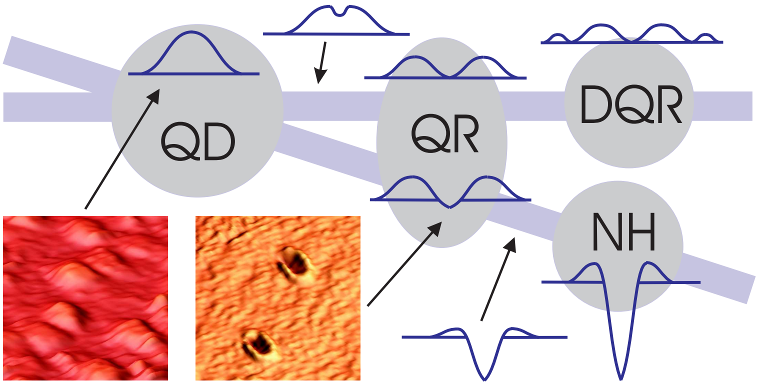

5.1. Fig. Overview of the III-V based droplet epitaxially grown nanostructures such as quantum dots (QDs), quantum rings (QRs), double quantum rings (DQRs) and nano-holes (NHs).

The low dimensional structures, grown by molecular beam epitaxy (MBE), has revolutioned the electronic devices both in their potentials and efficiency. Nowadays, the growth of self-organized nano-structures has been intensively investigated for basic physics and device applications. It is very important to understand their growth kinetics and to know their shape. The most prominent technique is the lattice mismatched Stranski-Krastanov growth mode [266, 267]. For instance, molecular beam epitaxy (MBE) growth of InAs quantum dots (QDs) driven by strain between the InAs deposit and the substrate. For a long time, for zero dimensional structure production, this strain-induced method, was the only known process. Based on Koguchi's discoveries, a droplet epitaxial technique evolved, giving greater opportunities for the development of the self-organizing nano-structures [190, 191]. In this method, the lattice-mismatch lost its significance and with the new procedure, it is possible to create QDs [272, 273, 194, 254, 196], quantum rings (QRs) [193, 243, 206], double quantum rings (DQRs) [255, 256] as well as nano-holes (NHs) [276, 281, 277] (see Fig. 5.1). The electronic structure of these nano-objects depends very much on their shape. Roughly, the droplet epitaxial process is the following: first, metal (e.g. Ga) droplets are generated on the surface in the Volmer-Weber-like growth mode. After, the crystallization of the droplets and their transformation occurs into e.g. GaAs QDs under arsenic pressure. In order to control the process it is necessary to understand the kinetics of the growth process. Here, no theoretical description is available yet of the underlying growth mechanism. In this paper, we are dealing with the III-V based nano-structures. The forms of the GaAs nano-structures, grown on AlGaAs (001) substrate, is strongly dependent on the applied technology.

Self-assembled semiconductor quantum dots (QDs) have attracted increasing interest stimulated for instance by advanced applications such as single photon emitter, quantum computing [12] and cryptography [264, 265]. Different methods have been developed to fabricate QDs, in particular with low areal density for single QD devices. The most prominent technique is the lattice-mismatched Stranski-Krastanov growth mode [266, 267]. For instance, molecular beam epitaxy (MBE) growth of about 1.5 monolayers (ML) of InAs on GaAs results in the spontaneous formation of InAs QDs driven by the strain between the InAs deposit and the substrate. Obviously, here, the electronic and optical properties of a QD crucially depend on its shape [268, 269] and composition [270]. The droplet epitaxy is an interesting alternative method to the strain-driven QD formation of InAs QDs. The basic idea of the droplet epitaxy was raised by Koguchi and his co-workers in the beginning of nineteen nineties [271, 272] and further developed in the following decades [273, 272]. As an important advantage in comparison to the Stranski-Krastanov growth mode, droplet epitaxy allows the fabrication of strain-free GaAs QDs. However, the low process temperatures used for droplet epitaxy cause the incorporation of crystal defects and background impurities [275]. A further very recent method for the fabrication of strain-free QDs is the local droplet etching (LDE) of nano-holes (NHs) and their subsequent filling [276]. In contrast to the droplet epitaxy, the LDE process takes place at optimum MBE growth temperatures and we expect here an only very low level of crystal defects. The LDE nano-holes are created in a self-organized fashion by local material removal [277, 276, 278, 279, 281]. For NH-QD fabrication, nano-holes are generated using Al droplets on AlAs substrates. A previous study on nano-hole etching with Ga droplets has shown that the walls surrounding the nano-hole openings are crystallized from droplet material and form GaAs quantum rings [23]. In order to avoid such an additional confinement by the walls, in the present experiments we use Al droplets. Subsequently, the holes are filled with a GaAs layer to form GaAs NH-QDs of controlled height [276, 282, 283]. In this paper, we discuss cross-sectional transmission electron microscopy (TEM) investigations of such GaAs NH-QDs formed by filling of nano-holes after droplet etching. The high-resolution TEM images are combined with elemental maps of the relevant species.

## 5.2. Technology of the Droplet Epitaxy

### 5.2.1. Growth of Nano-structures at Low Temperature

The growth experiments were performed in a solid source MBE system. The evolution of growth front was monitored in the $[1\bar{1}0]$ direction with reflection high-energy electron diffraction (RHEED). After the growth, the QDs were investigated with atomic force microscopy (AFM) in tapping mode. On the AlGaAs (001) surface (with Al content of $x = 0.3$), droplet epitaxial GaAs QDs were formed. The main steps of the droplet epitaxial process of QDs were as follows: Following the preparation of AlxGa1-xAs surface, the samples were cooled down to 200 and 250 °C, and Ga was deposited (the surface coverage $\Theta = 3.75$ ML) with the flux of 0.15 and 0.025 ML/s without the arsenic flux, respectively. After a few sec waiting time following the Ga deposition, annealing was performed at 350 °C temperature under $5 \times 10^{-5}$ Torr arsenic pressure. Detailed experimental description is published elsewhere [194]. The droplet-epitaxial QRs were grown as follows: Following the preparation of AlGaAs layer, the sample was cooled down to 300 °C, and $\Theta = 3.75$ ML Ga was deposited with the flux of 0.75 ML/s without arsenic flux. After Ga deposition we waited for 60 sec duration. During this time of the annealing, we kept the temperature the same (300 °C), at $4 \times 10^{-6}$ Torr arsenic pressure. Detailed description of the growth parameter is published elsewhere [245]. Here, the technological parameters of further five different nano-structures are given. The solution process investigated at two cases. The NHs was generated at 570 °C in AlGaAs surface applying 6.4 ML Ga [281]. In this case, The AFM measurement shows NHs and very large clusters [281]. The next nano-structure (sample type e) was prepared similarly, but the Ga coverage was different (3.2 ML) [276, 281]. Here, the AFM picture shows deep NHs surrounded by ring like bulge formations and shallow NHs, with plane rims (without any bulge) [276, 281]. The crystallization process is investigated at three samples. The first nano-structure is a very fast crystallized QD (sample type f). The crystallization of the Ga droplet occurs during the high arsenic supply ($2.5 \times 10^{-4}$ Torr) at 150 °C [254]. The elementar map of transmission electron microscopy (TEM) shows, that the QD had Ga inclusons [254]. The next sample (type g) is crystalized at $2 \times 10^{-6}$ Torr arsenic pressure at low temperature (200 °C) [255]. In this way, we received DQR [255]. The last sample (type h) is crystalized at about the same arsenic background ($1.1 \times 10^{-6}$ Torr) but at high temperature (500 °C) [277]. The middle of the structure is surrounded by single ring like bulge formations [277]. For detailed technological parameters of the above samples see the given references.

### 5.2.2. Nano-structure Preparation at High Temperature

The NH-QD sample was fabricated on a GaAs (001) substrate using solid source MBE with a valved cracker cell for arsenic evaporation. A scheme of the layer sequence is sketched in Fig.1a. The sample is projected as a Laser structure according to a design proposed in Ref. [275]. Five stacks of GaAs NH-QDs are embedded in $Al_{0.23}Ga_{0.77}As$ barrier material. This stack is embedded in an $Al_{0.69}Ga_{0.31}As$ wave guide. The NH-QD layers were fabricated as has been described previously [276, 284]. After growth of the $Al_{0.23}Ga_{0.77}As$ barrier layer, a 5 nm thick AlAs layer was deposited (dark blue lines in Fig. 5.20.). The As beam was supplied by a valved cracker cell. After growth of the AlAs layer, the As shutter and valve were closed and 3.2 ML of Al was deposited at $T = 650$ °C to form Al droplets on the AlAs surface. This is followed by an annealing step of 180 s, during which the droplets transform into nano-holes [278]. Following that, the NHs were partially refilled by deposition of a 0.6 nm thick GaAs layer in a growth-interrupted fashion. From the thickness of the GaAs filling layer, we estimate the height of the QDs to be 8 nm according to the model described in Ref.[276]. The structures were covered with $Al_{0.23}Ga_{0.77}As$ and the whole growth sequence was repeated five times. Due to the very fast oxidizing AlAs surface and the corresponding modification of the surface morphology, reliable AFM measurements of the nano-structures under air are not possible. For illustration, we thus show reference data obtained after etching of $Al_{0.35}Ga_{0.65}As$ with Ga droplets at 620 °C. Clearly visible are the nano-holes and the walls surrounding the hole openings [281]. Thin cross sectional specimens from the sample were prepared for the TEM investigations by cutting, embedding into a special holder, mechanical grinding, polishing, and finally ion beam milling with 10 keV Ar ions. The conventional TEM imaging of the samples was performed on a Philips CM20 electron microscope at 200 kV. The high resolution images and elemental maps were taken with 300 kV JEOL 3010 high resolution microscope equipped with an imaging filter (GATAN Tridem model).

## 5.3. QD Formation Investigated by RHEED

### 5.3.1. The RHEED Stages and the Facet of the Quantum Dot

During the growth process, the main stages of the RHEED pattern are shown in Fig. 5.2. The diffraction pattern of the initial AlGaAs surface consists of sharp streaks (Fig. 5.2./A). After the Ga deposition the picture becomes diffuse (Fig. 5.2./B). At this time liquid Ga droplets have been formed on the surface. After the opening of the As cell, the RHEED picture was changed from diffuse to spotty one (Fig. 5.2./C). This indicates appearence of crystalline and even monocrystalline state. During the annealing in the arsenic atmosphere, characteristic chevron-tails were developed from the spotted RHEED picture (Fig. 5.2./D).

The chevron-tails are connected with the faceting of QDs as it was verified in the case of diverse shaped droplet epitaxial QDs [195]. In our case, it can be shown from the atomic force microscopy (AFM) measurement and from the tilted TEM picture that the shape and size of QDs are very uniform [196], and their side angle is about 25° [194], which corresponds to the half opening angle of the chevron-tails (see the insert in Fig. 5.2./D). In spite of the same shape of the QDs, the chevron-tails are not sharp but broad. The observed side-angle near to 25° corresponds to the (113) crystallographic plane [195]. In the case of InAs QDs on GaAs with the same side-angle, sharper and line shaped chevron-tails can be observed usually [268, 197] although the uniformity of the QDs is higher in the case of droplet epitaxially produced.

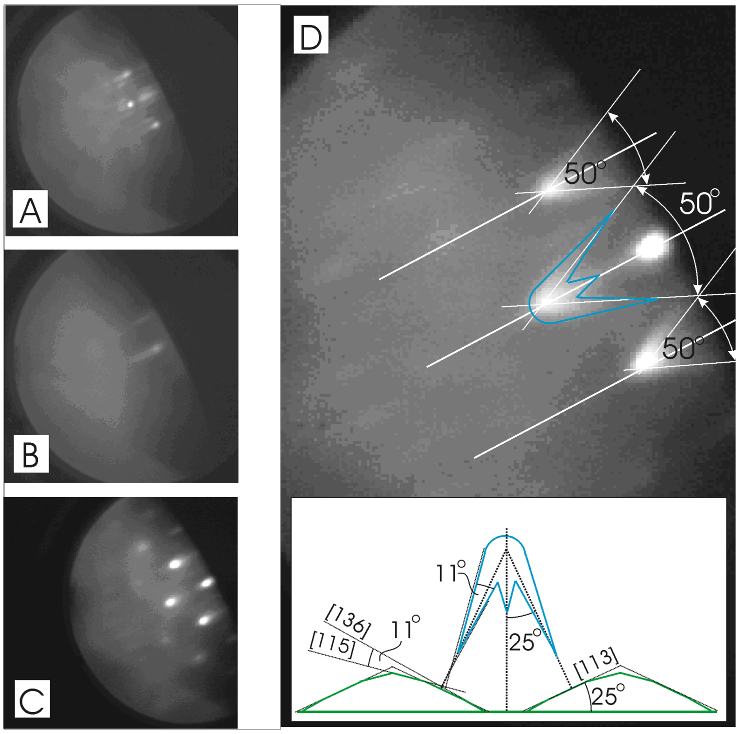

5.2. Fig. The change of the RHEED pattern in different stages of the QD formation. (A) The RHEED pattern of the initial AlGaAs surface (B) The RHEED pattern after the Ga deposition (C) The RHEED pattern after the opening of the arsenic cell; the dotted pattern represents monocrystalline transmission character (see text). (D) The appearance of the chevron-tails after the annealing stage and (insert) its explanation. The chevron-tails appear only in later stage of the crystallization, when the shape of the nano-structure becomes characteristic (see text). These shevron-tails are not sharp but rather broadened.

A cross sectional TEM image of a droplet epitaxial QD is shown in Fig.

5.3 Figure shows that the QD is perfectly crystalline. The crystal planes of the substrate are continued without any break in the QD, no defects can be observed at the interface. The side of the QD is not a single crystalline plane but it has stepped shape (faceting). The steps consist of planes parallel with interface (parallel with 002 crystal planes) and planes with 55° to the interface, corresponding to 111 planes. The envelope curve of the QD cross section is a circle segment with radius of R = 64 nm (see Fig. 5.3.). The base width of the QD is 54 nm.

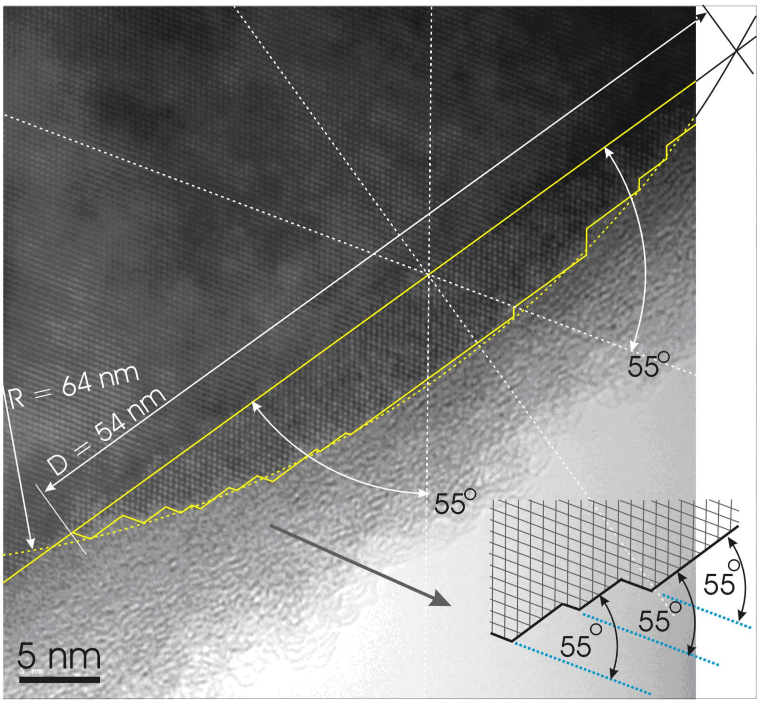

5.3. Fig. Cross sectional TEM picture of a QD. The side-facet of the QD is stepped. The cover-line of the stepped quantum object is a circular segment. The stepped side-facet consists of planes parallel with interface and also of planes with angle of 55°. (see insert)

## 5.3.2. Growth of the Stepped Facet

During the growth of QD, side facets with low Miller-index (corresponding to 55°) are preferred to side facets with higher Miller-index (corresponding to 25°). This is proven by the observation of strain induced QDs: when the growth process is slow, the side-facet-angle will be 55° [173]. When the growth process is fast, the low side-facet-angle will grow [199]. When the growth of QDs is slow, than there is enough time available for the atoms to find their optimum (minimum energy) position, to form low Miller-index facet (55°). When the growth of QDs is fast, there is not enough time for the migration to find the optimum position, therefore non-optimum Miller-index facet will be formed. This can be considered as a frozen state.

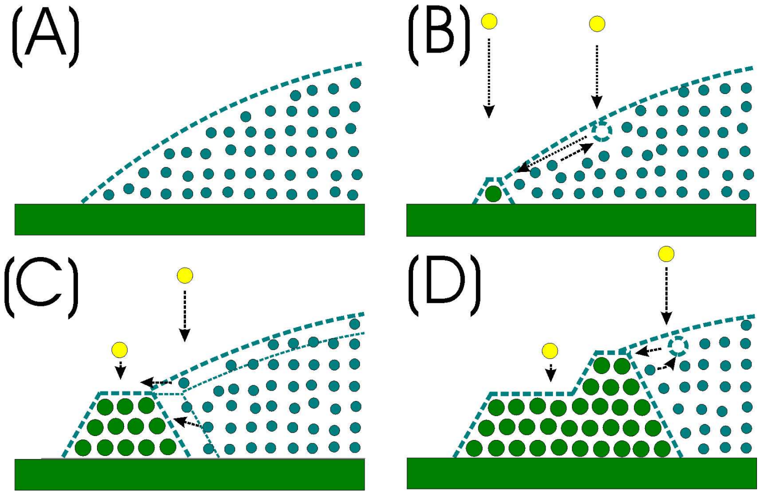

5.4. Fig. The steps of the crystallization of QD; Blue: Ga in the droplet, yellow: arsenic in the environment, green: crystallized state of III-V material; (A): Ga droplet on the crystalline surface, (B): The seed of the crystallization forms at the three-phase-line, (C): The crystal seed has a favourable (111) outer facet and it grows partly upwards and also partly into the droplet. During the growth, the relative position of the three-phase-line moves to the crystal edge (see the text). (D): As a result a stepped side facet will be developed.

The evolution kinetics of the stepped outer surface of the QD can be observed according to Fig. 5.4. The intersection of the crystal surface with the droplet is the three-phase-line, which serves as initial place of crystallization [200]. When a Ga atom of the droplet meets an arsenic atom, they form a GaAs molecule. These GaAs species making a Brown-like movement over the droplet surface can reach the three-phase-line, where the crystallization starts (Fig. 5.4./B). Here, the crystal structure of the forming seed perfectly corresponds to the crystal structure of the substrate. The crystal seed at the three-phase-line will grow on the account of further arriving arsenic species. The outer facet-angle of the crystallization centre at the edge will be the favourable 55° because it has enough time to find the optimal position (the low index facet).

The crystallization seed grows partly upwards and also partly in direction of droplet inside (Fig. 5.4./C). During the process of solidification, a circular monocrystalline phase is formed at the droplet edge inheriting the orientation of the perfect substrate. This phase is responsible for the spotty RHEED pattern (Fig. 5.2./C) although the structure is not large enough to cause a visible chevron-tail. The chevron-tail becomes visible upon the increase of the crystallized volume. During the process of solidification the amount of Ga atoms in the droplets decreases so the droplet size decreases too. Fig. 5.3. shows that the outer side of the QD consists of steps of few mono layers, where the front panel and the terrace of the step are (111) and (001) planes, respectively. It is known in fcc crystals that the surface energy of (111) face is less than that of (001) face thus the latter grows predominantly during crystallization [201, 202]. This takes place by the lateral shift of the low energy (111) step faces with simultaneous areal growth of (001) faces (Fig. 5.4./C). With the size decrease of the droplet its edge moves inward thus creating a new triple-phase-line or crystallization seed at the new place (Fig. 5.4./D) and the whole process continues as before with the original droplet and substrate. The only difference is that the crystallization takes place along a circle of less and less diameter.

The crystallization of the QD begins simultaneously at the droplet edge. So after the formation of Ga droplets, upon opening the arsenic cell, the RHEED pattern becomes almost immediately spotty. This is because the crystallized material at the droplet edge at the whole surface is monocrystal and has identical crystal structure than the substrate. Therefore, the RHEED shows a monocrystalline transmission diffraction pattern. Here, the intensity of the spotty pattern increases in time with the increasing of the quantity of the monocrystal. The chevron-tails develop continuously in later stage of the crystallization, when the shape of the nano-structure becomes characteristic (Fig. 5.4./D). Since the centre of crystallization at the droplet edge fits very well to the substrate crystal the structure of whole crystallized QD will also fit to the substrate.

### 5.3.3. Explanation of the Shevron Broadening

It is known that the droplet epitaxial QDs have a very homogeneous lateral distribution [196]. Their sizes and shapes are also homogeneous, compared to the strain induced QDs. However with a strain induced QDs have a sharp chevron-tail on its RHEED pattern [268, 196]. In spite of the similar size and form of droplet epitaxial QDs, the RHEED pattern is broadened, the chevron-tail is not sharp and line-like, as it is usually in the case of well defined QD facets (Fig. 5.2./D). The reason of this effect is hidden in the form of droplet epitaxial QDs (see Fig. 5.2./D and 5.3.). The shevron-tails are perpendicular to the side planes of the QDs which are stepped in the reality. In our case, the QD side does not consist of single crystallographic plane but there are few such planes with different angles, which results in the broadening of the shevron-tails.

It is proven, that the chevron-tail is perpendicular to the side plane of the QD. This is true, independently from the angle of the side plane that is true both for the low-index and high-index surfaces. In the case of low-index, the surface consists of sole crystal facet. In the case of high-index, the surface forms by low-index terraces and steps. This observation corresponds with the idea that planes with high surface energy break up into faces corresponding to planes with lower surface energy forming distinct ordered surface structures on a nanometer scale which represent the equilibrium configuration [203, 204]. In our case, the edges of the crystallographic steps, near to the base of the QD, fall nearly into the same plane. The inclination of this plane is somewhat less than 25° as shown in Figs 5.2. and 5.6. (This difference can originate from the non-diameter cross-section TEM image. It is proven that the base width measured by TEM is less than measured by AFM method.) This dominant angle and its corresponding opening angle of the chevron-tail on the RHEED image are marked in Fig. 5.2. Towards the top of the QD, the inclination of the bordering planes with high-indices gradually diminishes causing the widening of the shevron-tail. Approaching to the top of QD, the bordering high-index planes have less inclination angle. The broadening of the chevron-tail is due to the decrease of the inclination angle of these planes. This observation correlates with the RHEED pattern broadening of the misoriented mosaic structure [205].

## 5.4. Growth Kinetics of the QD

### 5.4.1. The Lateral Distribution of the Droplet Epitaxially Grown QDs

The formation of the QDs on AlGaAs (001) surface were observed by in situ RHEED. At the start of the process, the RHEED pattern of the surface shows sharp streaks. After the Ga deposition, the pattern becomes diffused on RHEED screen (stage A). Almost at the same time with the opening of As cell (pressure of $6.4 \times 10^{-5}$ Torr), the RHEED pattern changed from diffused to spotty (stage B). During the annealing phase, the pattern has changed slowly (some minutes) from spotty to spots with chevron tails [206].

Fig. 5.5 shows the QDs as observed on the AlGaAs surface by AFM (A) and by TEM (B). To make the latter image, the cross sectional TEM specimen was tilted by 30°. Both images show, that the QDs have uniform shapes and the sizes were distributed homogeneously on the surface. A part of the region of 1 $\mu$m × 1 $\mu$m is recorded in perspective and shown in Fig. 5.5.A. (upper insert). The mean dimensions of QDs (60 nm base width and 7.5 nm height) were determined from individual line scans of the height. An example of one of these scans (from the marked QD at the middle of the image) is shown on the lower insert of Fig. 5.5.A. The surface density of QDs was determined from AFM pictures as $1.5 \times 10^{10}$ cm$^{-2}$. The TEM image of the tilted sample (Fig. 5.5.B.) confirms the presence of the homogeneously distributed QDs of uniform size. Their density (calculated from the TEM image taking into account the tilt angle) was found $2.5 \times 10^{10}$ cm$^{-2}$, slightly different from the value measured by AFM. This small deviation may come from the little macroscopic inhomogeneity of the sample (the AFM was performed at the wafer centre while TEM specimen was prepared close to the wafer edge, because the two measurement location were positioned at least 2 cm from each other) or from the different measuring method.

### 5.4.2. Lattice Match between QD and Substrate

The atomic resolution structure of a typical quantum dot is shown on Fig. 5.6 (the image was taken with the electron beam parallel to the [110] zone axis of the AlGaAs single crystal substrate). The amorphous film above the surface consists of two distinct layers: a thin photoresist protecting layer (darker contrast, marked by "a") and the glue applied between the two faces

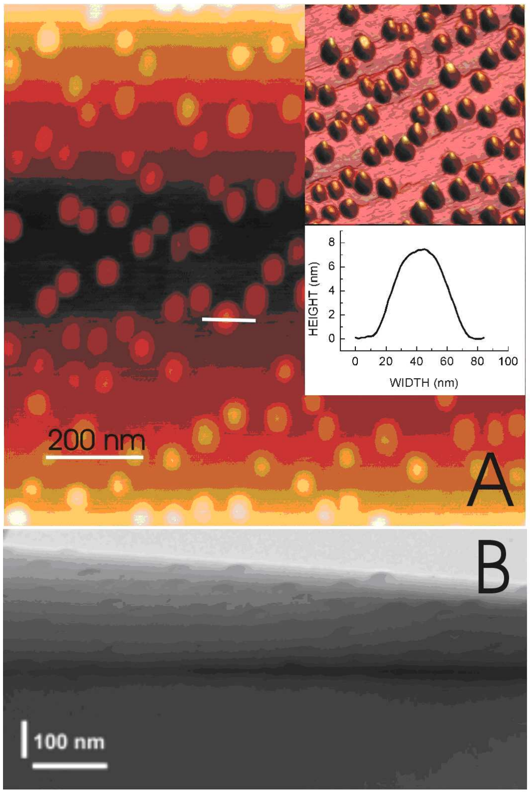

5.5. Fig. A: AFM image of QDs; The density of QDs calculated from AFM image is $1.5 \times 10^{10}$ cm$^{-2}$; The inserted pictures show the perspective of QDs (taken by AFM) and the profile of a typical QD (the direction of the scan is marked), respectively. B: QDs on the tilted surface with the angle of 30°. The image is taken by TEM. The density of QDs calculated from the tilted TEM image is $2.5 \times 10^{10}$ cm$^{-2}$.

of the cross sectional specimen (brighter, marked by "b"). The presence of these layers on the image makes sure that the original surface morphology was preserved during the complex process of specimen preparation. Fig. 5.6. shows that all the lattice fringes of the AlGaAs substrate are continued in the GaAs QD without any distortion. It is well known that the lattice parameters of these two substances are practically the same. No crystal defects were be observed within the QD or at the interface with the host crystal.

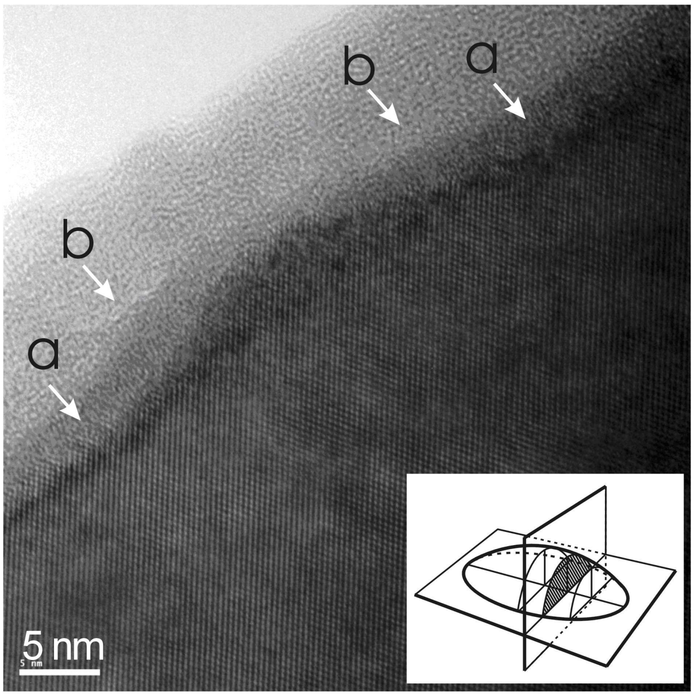

5.6. Fig. High-resolution cross-sectional TEM image of a droplet epitaxial QD. The lattice parameters of the substrate and QD materials are about the same. No lattice defects are visible at the interface. Two amorphous layers are visible on the surface; a: surface is covered by lacquer for protection, b: adhesive required for sample preparation. The QD visible in TEM image is less than mean size of QD measured by AFM (see inserted profile in Fig. 5.5.). This can originate from the non-diameter coss-section (see inserted figure).

### 5.4.3. Composition of the QD and its Environment

The feature mentioned is shown in a darker contrast of the QD, also a few atomic surface layer of AlGaAs crystal between the QDs. The darker contrast on the AlGaAs surface can be interpreted as follows. The AlGaAs layer, at low temperature, shows As rich c(4×4) surface. Nominally $\Theta = 3.75$ ML Ga is deposited on the surface without arsenic flux. In the duration the Ga supply, a few ML of Ga is combined with excess arsenic surface atoms, thus a thin GaAs layer forms on the surface, while the rest of the Ga forms nano-droplets (stage A). During the crystallization, the droplet and the surface layer go into similar composition (stage B). As a result the QD and the surface layer shows similar darker contrast compared to the host material. The existence of this GaAs surface layer was predicted earlier from the comparison of the photoluminescent measurement and the energy levels calculation [274].

The dimensions of the QD in Fig. 5.6. were 35 nm base width and 4.5 nm height., These are somewhat lower than the average measured by AFM. The probable cause is that during preparation, the QD might have been sectioned not at its largest diameter (see insert). The steepness of the QD side wall was measured on the TEM image as well as by AFM. The result were about 25° measured by both methods, which also correlates with the RHEED image showing a chevron angle of 50° [194].

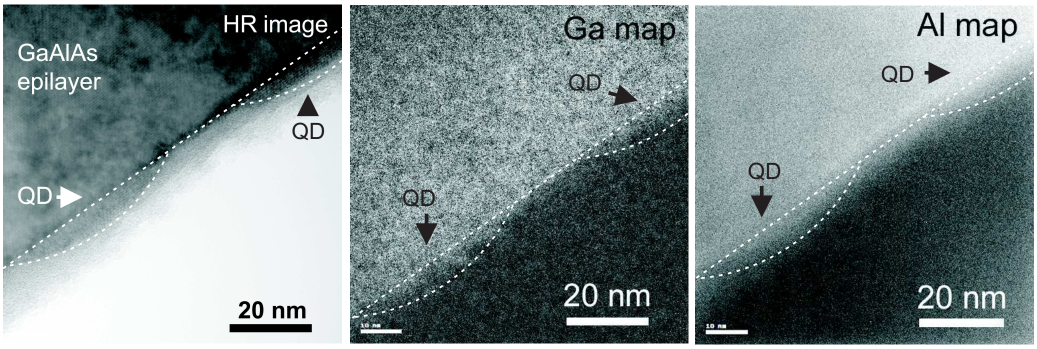

5.7. Fig. Composition of the QD with the help of electron energy loss spectroscopical (EELS) scan; upper part: High-resolution cross-sectional TEM image of a QD, middle part: Ga-L map on the same cross-section, lower part: Al-K map on the same cross-section; The dotted line serves as guide for eye to recognize the interfaces.

Fig. 5.7 shows the high resolution micrograph of a similar QD together with Ga and Al elemental maps (composed from energy filtered TEM) of the same area. The elemental maps were taken with the three windows technique using the Ga-L edge and the Al-K edge. Although their spatial resolution (typically a few nm) is far from that of the high resolution image (0.17 nm) these images clearly show that the QDs contain both Ga and Al. The presence of Al within the QDs is supported by the explicit protrusion of bright contrast on the Al map at regions corresponding to the QDs.

### 5.4.4. Some Aspects to the Kinetics of Droplet Epitaxially Grown Structures

The formation mechanism of droplet-epitaxial GaAlAs QDs is explained as follows. The first step is the deposition of Ga resulting in the formation of small Ga droplets on the AlGaAs surface (stage A). The appearance of liquid aggregate on the surface is proved by the change of the sharp diffraction streaks in RHEED to a diffused pattern [206]. It is known from the liquid phase epitaxy, that thermal etching takes place at the Ga melt/GaAlAs crystal interface [207] and Al or AlAs species dissolve into the Ga melt. This dissolution occurs when the Ga is in liquid state. The Al contamined volume of the droplet spreads out from the bottom interface to the outer shell (see Fig. 5.8. A., process (1)). This dissolution and mixing of the constituents takes place continuously during the whole 60 sec waiting time since the surface aggregate is in liquid status during this time (according to RHEED result). On the Al elemental map (Fig. 5.7.) a slight enrichment of aluminum can be observed in a thin surface layer of the substrate. This might be the result of the demixing effect similar to that observed in the case of GaAs/AlGaAs [208].

The next step (processing) begins with the opening of arsenic cell (stage B). The appearance of the crystalline phase is confirmed by in situ RHEED as well, showing the transformation of the diffuse pattern to a spotty one as soon as the As background emerges [206]. It is known, that the formation of the droplet epitaxial nano-structures is caused by As diffusion and Ga migration together. While at higher temperature and lower arsenic pressure, the Ga migration is the dominant process during nano-structure formation, at lower temperature and at higher arsenic pressure, the As diffusion dominates the formation [211]. In the case of dot formation, the spread out process is suppressed and the As diffusion is dominant. The lateral spread out of the structure, due to the Ga migration helps the formation of rings. The process of GaAs crystallization starts at the edge of the droplet, initialized by the three-phase-line at this point, serving as discontinuity for the seeding [192]. Although in principle interaction can take place at any point of the droplet, due to the thermal movement, the species, arriving to the edge, will start the seeding of the crystallization process. The described mechanism for this process have been accepted by other authors too, otherwise it would de difficult to explain the formation of the quantum rings [200, 209, 210]. In the case of a dot, the seed grows inwards, whilst in the case of ring it tends to grow outwards, which is maintained by the Ga migration. Since we are dealing with dot shape, the dominant process is As diffusion [211]. The crystal seed grows inwards into the droplet, and also upwards simultaneously. This process of growth can only be explained quantitatively because, in the case of nano-sizes, the observed bulk processes and properties like diffusion and binding energy can not be applied. Although similar crystallization processes have been observed, but till now no attempt has been made to explain them (see Fig. 5.8. B., process 2) [253].

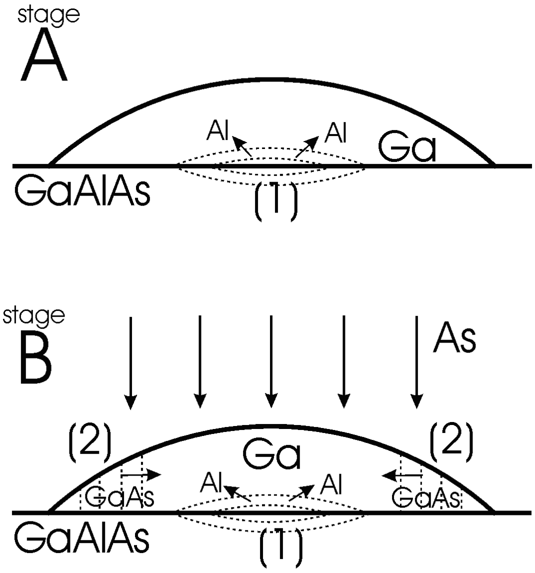

5.8. Fig. The scheme of the Ga droplet on GaAlAs surface; (A) during the waiting time; (B) after the opening of arsenic cell; (process 1): Dissolution of AlAs at the gallium (liquid) - GaAlAs (solid) interface; (process 2): growth of crystalline GaAs starting from the droplet edge.

The growth of the GaAs crystal occurs in direction opposite to the penetration of Al (see Fig. 5.8). The crystallization of GaAs (process 2) can start only after the opening of arsenic cell, while the dissolution of AlAs species (process 1) occurs immediately upon deposition of droplets. The process 2 is quicker than process 1. So, the process 2 is the dominant during the processing time.

An important part of the above discussed process is the dissolution. The phase diagram of the Ga-Al-As system is known. Nevertheless, the interpretation of the processes can be given only qualitatively. The thermodynamically calculated and the measured values differ from each other [213]. The nano-scale material properties (also thermodinamical properties) may differ drastically from the macroscopic case. These nano-scale properties are known only partially as yet. The description of the phase transitions has some incompleteness even in the macroscopic case. So in our nano-sized case, the above mentioned thermodynamical description is a rough qualitative approximation.

## 5.5. Growth Kinetics of Droplet Epitaxial QR

### 5.5.1. Distribution of the QR Size and its Cavity

The development of the QR structures was monitored in-situ by RHEED. In the initial stage, the perfect crystalline AlGaAs (001) surface causes sharp RHEED streaks on the fluorescent screen. Then, due to the presence of Ga, droplets form on the surface, whose formation is governed by Ostwald ripening [214, 215, 216, 217]. After the deposition of Ga, the RHEED picture is becoming diffuse, due to the amorphous nature of the phase present on the surface. The annealing phase begins after the offering of arsenic component with the pressure of $4{\times}10^{-6}$ Torr, while the substrate temperature is 300 °C. After releasing the arsenic, some time is needed for the development of the characteristic sharp pattern, representative of the crystalline structure (see Fig. 5.9./A.) 5.9. This is an indication, that the liquid state on the surface stays longer and that the material transfer processes helps the formation of the QRs. This process is different from the QD formations, when the RHEED pattern characteristic to the crystalline phase coincides with the opening of the arsenic cell [206]. For detailed technological parameters of the different droplet epitaxial nano-structures (QD, QR etc.), we refer the readers to the literature [242, 210, 243, 244, 245, 275, 193, 220, 219]. After the completion of the growth, the QR structures were investigated with AFM. The perspective AFM image and the top view with line scans are shown in Fig. 5.9./B and C, respectively. The dimensions of QRs were determined from individual line scans. Two typical adjacent AFM line scans are shown in the right side of the Fig. 5.9./C. The density of QRs determined from AFM pictures, was $1.5{\times}10^{9}$ cm$^{-2}$. It is visible, that the middles of the QRs are deeper than the original surface level. It can be shown, from the AFM measurement, that although the shapes and sizes of QRs are fairly uniform, we can observe small deviations from these averages. It is often observed, that the smaller diameter QRs have deeper cavities in the centre and the larger diameter QRs have shallower ones in the middle. (In the illustrations, the smaller and larger objects are labelled with "S" and "L", respectively.) Fig 5.9./C shows, that the QRs have slightly elongated shapes (see top view), due to the different binding properties in [110] and $[1\bar{1}0]$ directions [221]. This phenomenon however is neglected, because it has no influence on our general proposition. The larger QRs are larger in both lateral directions, and the smaller ones are smaller. (It is common knowledge, that the shape of the AFM tip influences the line scan, particularly the slope of the side wall, therefore the bottom area of the cavities are distorted. In the general proposition, we use two parameters of QRs, such as the diameter of QR (i.e. is the distance between two tips on opposite side) and the depth of the cavity in the middle of QRs. Both parameters can be measured accurately, although the diameter at the apex is less than ten nm.

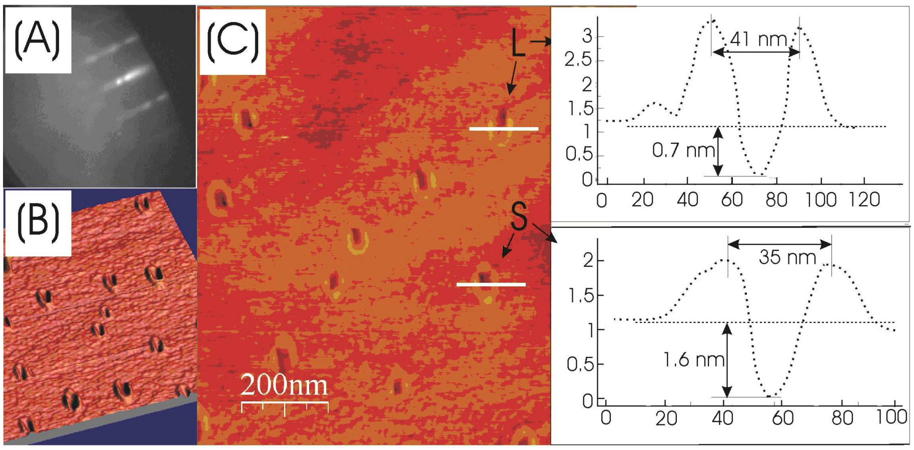

5.9. Fig. Experimental data of the AlGaAs (001) surface with GaAs QRs; (A) The RHEED pattern of the AlGaAs surface with the GaAs QR structures, (B) The perspective AFM picture of the sample surface, (C) Top view of the AFM image with line scans of single QRs (marked with white lines).

### 5.5.2. The Contradictory Behaviour

These facts are contradictory to the aspect ratios of QRs and the explanation can be help to the understanding of the kinetics of the droplet epitaxial quantum structure formation. Our explanation to this extraordinary behaviour is as follows. During the Ga deposition, droplets form on the AlGaAs surface. It was assumed, that the larger droplets are leading to the development of rings of larger diameter and equally the smaller droplets to smaller rings. The intersection of the crystal surface with the droplet edge is the three-phase-line, which is the starting initial place of crystallization [200, 222]. The three-phase-line of larger diameter initiates a larger droplet and equally, the smaller diameter forms from a smaller droplet. It is known from the liquid phase epitaxy, that thermal etching takes place at the interface of the Ga melt and AlGaAs surface [207]. This phenomenon was confirmed by analytical transmission electron microscopy for droplet epitaxial QD [196]. The Ga melt can solve the arsenide molecules (e.g. GaAs). These arsenide molecules originate partly from the thermal etching of the AlGaAs substrate surface and partly from the reaction of the external (from effusion source) arsenic atoms. (When a Ga atom of the droplet meets an arsenic atom from the environment, they form a GaAs molecule.) These molecules, due to thermal movement in the droplet, can reach the three-phase-line, where the crystallization takes place. During the process of solidification, the material migrates from the middle to the edge of the nano-structure. A circular crystalline phase is formed at the droplet edge. During the solidification, the number of Ga atoms in the droplets drops, therefore the droplet size decreases at the same time. The proposed kinetics for the formation is shown schematically in Fig. 5.10 (During the thermal etching, not only arsenic and gallium but aluminium as well leaves the AlGaAs surface, building up the lattice matched crystalline part, shown earlier for QDs [196]. We assume, that similar conditions exist for QRs.

### 5.5.3. The Solubility and the Size Effect

It is known for a long time also, that the melting point decreases with the reduction of the particle size. This finding is in qualitative agreement with the theory of thermodynamics, which states, that small particle should melt at lower temperature than that of the bulk, due to surface effect [223, 224, 225, 241, 227, 228, 229]. In bulk, the surface-to-volume ratio is small usually and the curvature of the surface is negligible. Melting of small particles showed a rule of reduction in melting point as approximately 1/r. The ratio breaks down for particles with less than approximately 50 nm diameter (that is around 500 atoms). This is verified theoretically as well as experimentally

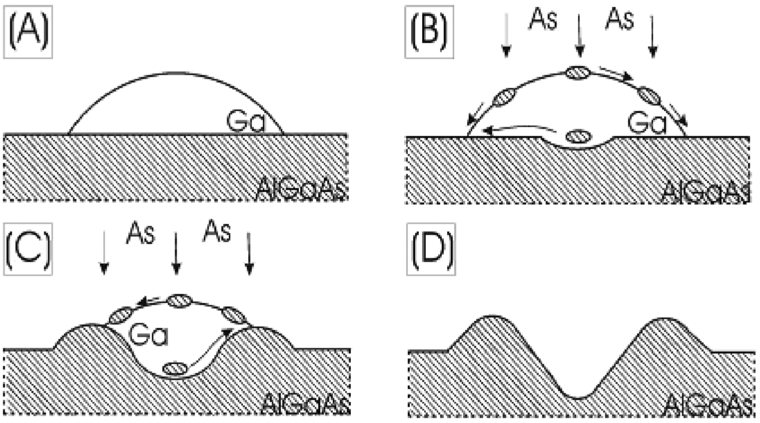

5.10. Fig. Process of QR formation (A) Ga droplet, (B) and (C) different state of the QR evolution, (D) ripened QR structure (detailed description in the text).

for different metals [241, 227, 230, 231, 232, 233, 234]. The left part in the the Fig. 5.11. depicts the normalized melting curve vs. diameter of the particle. It shows, that when the particle size is less than 50 nm, then the melting point depends very strongly on size. In the nano-range, this dependence on the size is stronger than for the bulk. What makes it more complicated is the fact, that the melting point depends on the particle shape as well [229]. In our case, the Ga droplet's shape is a segment of a sphere. Its width in the middle falls in the range of 10 - 20 nm. Here, the change in the melting point is particularly sharp (see Fig. 5.11.) 5.11. Around the edges the structure is thin. (The properties of this regin will be discussed later.) The experimentally obtained melting curves for near spherical metal nanoparticles show similarly. We use these curves for the qualitative assessment. This indicates, that the melting point of the large and that of the small Ga droplets can differ considerably. The right side of this figure shows the solubility curves for different particle sizes. This figure also shows, that at the same temperature, the larger droplet has lower saturating concentration than the smaller one [235]. The meaning of this is, that crystallization in the larger droplet will take place earlier, at lower arsenide concentration than in a smaller one. The smaller droplet will crystallize later, when arsenide concentration is already high.

We have to mention, that we take it as obvious, that the crystallization

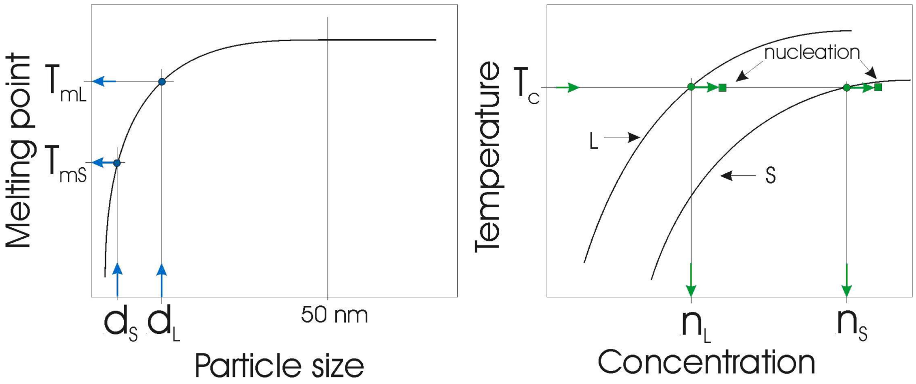

5.11. Fig. Left side: The melting point dependence vs. particle diameter. If the size less than 50 nm then the dependence is very strong. In our case, all dimensions of the droplet are less than this size. The smaller droplet has significant lower melting point ($T_{mS}$) than larger ones ($T_{mL}$). Right side: The solubility (conc. vs. temp.) for different droplet sizes. The temperature of the crystal formation was the same in both cases (in our case $T_c$ = 300 °C). The nucleation starts at much higher dissolvable GaAs concentration in smaller droplets due to their lower melting point.

process starts at the skirts of the QRs, at the intersection of the crystal surface, at a three-phase-line, formed with the droplet edge. The question arises however, that we considered the solution only at the middle of the droplet and neglected the droplet edges. The theoretical studies of the nanoparticles revealed a number of unknown phenomena, some verified experimentally [236]. One of those is the fact, that Ga nanoparticle, containing less 40 atoms, have their melting points higher than that of the bulk material. These higher melting points (over 300 °C) are attributed mainly to the covalent bonding in the cluster, against the bulk covalent-metallic bonding [237, 238]. Considering the experimental temperature of 300 °C, the middle of the droplet is liquid already, while the thin edge of the droplet is still solid (the number of Ga atoms is small). As a result, the middle is still in a liquid phase, where the crystallization, or thermal etching, could take place. At the edges of the cluster Ga is in a solid phase, therefore solution is not present. The solution is restricted to the middle and that is opposing the crystallization [239].

The temporal evaluation of the smaller and larger QRs is shown in Fig. 5.12. In other words, in the larger droplets, the probability of the formation of the crystallization seeds is higher; therefore the crystallization takes place

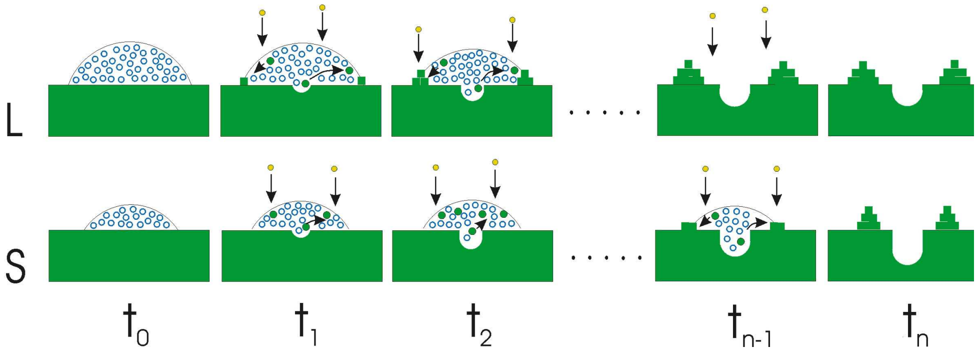

5.12. Fig. Temporal evaluation of the quantum ring for both droplet sizes. Upper part represents the larger ($L$) while the lower part the smaller ($S$) droplet. The small open blue ring and the small yellow and larger green disc represent the Ga, As atoms and GaAs molecules, respectively. The green cornered figure (angular formation) represents the crystalline material. The initial stage for both particle sizes is the same ($t_0$). In the case of smaller droplet size, the duration of the thermal etching process is longer.

earlier so less time is spent on material transportation, causing the development of the hole in the middle. When the droplets are small, the probability is less, crystallization starts later, leaving more time for the formation of deeper hole in the centre of the ring. This process is influenced by other factors as well. The melting temperature of the nano-structure is dropping with its diminishing size, staying longer in liquid state at the same temperature, spending more time on the formation of deeper cavity in the centre. This conclusion can only be made on statistical ground. It is likely, that the forming process depends not only on the size of the droplets but also on the arsenic molecules, whose presence is independent of the size of the droplets. Although, the size and spatial distribution of these nano-structures looks fairly uniform, we observed some deviations from this rule.

## 5.6. RHEED Observation of QD and QR Formation

### 5.6.1. Evaluation of the Temporal RHEED Pictures

Both kinds of GaAs quantum objects such as QDs and QRs was evaluated on AlGaAs (001) surface. The initial stage of the surfaces was the same in both cases. The RHEED pattern showed sharp streaks (see Fig. 5.13. column A). After the Ga deposition, the pattern became diffuse on the RHEED screen (column B). In the case of QDs, almost at the same time with the offering of As pressure of $5\times10^{-5}$ Torr, the RHEED pattern changed suddenly from diffuse to spotty (see upper part of column C). During the annealing phase, the pattern changed slowly (some minutes) from spotty to spots with tails (upper part of column D). In the case of QR production, the process is the same until stage of Ga deposition. But after the Ga deposition, the change of the observed RHEED pattern is quite different. After the Ga deposition, the RHEED pattern becomes diffuse (lower part of column B). After the offering of As background of $4\times10^{-6}$ Torr, the RHEED pattern develops very slowly (over five minutes). The developed pattern contains in the middle a streak with a small spot and around elongated larger spots. The density of QDs and QRs are different, so the influence of the open (001) surface on the RHEED pattern is also different. The densities of QDs and QRs are $3.6\times10^{10}$ and $1.5\times10^{9}$ cm$^{-2}$, respectively. In the case of QR, the effect of open surface on RHEED is larger than in the case of QD. It is shown; that the characteristic RHEED pattern of QD is still recognizable even, if the dot density is one order of magnitude less [194]. The RHEED tracking of the temporal evaluation of both quantum objects is summarized in Fig. 5.13.

The sharp RHEED streaks disappear and the diffraction picture becomes diffuse during the Ga deposition. The deposited Ga is in liquid phase. The disappearance of the RHEED pattern originates from the appearance of the liquid phase (Ga droplet) on the surface. In the annealing phase of QD production, the RHEED pattern becomes from diffuse to spotty nearly simultaneously with the opening of As source. The sufficient As quantity ($5\times10^{-5}$ Torr) and the low temperature (200 °C) make the building-in (infiltration) of As in Ga phase that is the crystallization possible [250]. This process of infiltration takes about two-three minutes to the sharp chevron image (see Fig. 5.13. Upper part of column D). So, a crystallized shell comes into

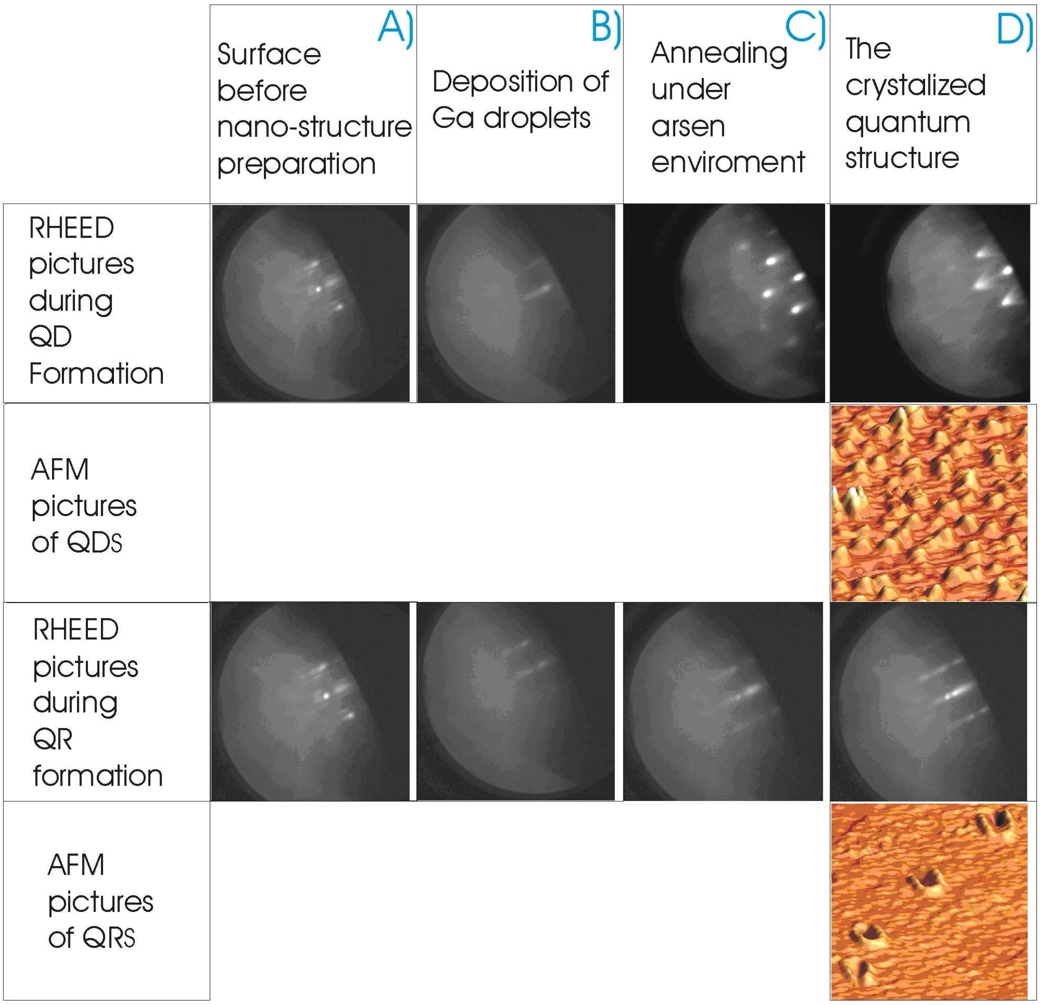

5.13. Fig. RHEED patterns observed step by step manner during the evolution of the quantum objects and the AFM picture of the ripened structure. The upper and lower parts concern QD and QR, respectively. The density of QDs and QRs are $3.6 \times 10^{10}$ and $1.5 \times 10^{9}$ cm$^{-2}$.

being on the Ga droplets. The appeared spotty RHEED pattern originates from the transmission electron diffraction. The electron beam goes through the crystalline GaAs shell layers. It is observed, if there are crystallite formation or droplets on the surface, bulk scattering of the grazing beam can occur and the RHEED pattern may become dominated by spots rather than streaks due to transmission electron diffraction. The scattering from several planes modulate strongly the intensity along the reciprocal lattice rod. So, the streaks observed from two-dimensional surface are not observed when transmission dominates. For the transmission case, the reciprocal lattice is an array of points each broadened owing to the finite size of the scattering region. During the annealing, the As diffuses inside of droplets, while excess As builds in (infiltrates) in the shell [250, 253][20, 23]. So, the droplet crystallizes through slowly. At the same time, chevron-shape spot develops on the RHEED screen [194].

### 5.6.2. Interpretation of the RHEED Image for QD

In the case of InAs/GaAs QDs, the shevron-tails were attributed perpendicularly to the facets (reciprocal rod nornal to (113) and $(\bar{1}\bar{1}3)$ facets because the angle between the two chevron-tails is about 55° [252][22]. For $[1\bar{1}0]$ incident azimuth, an electron beam which enters via $(\bar{1}13)$ facet and exits from the $(1\bar{1}3)$ is refracted into the $[00\bar{1}]$ direction. This gives rise to streaks perpendicular to the (001) surface. Alternative approach is based on refraction effect, which can explain the origin of RHEED pattern [251][21]. It was observed that refraction from inclined facets on small crystallites on a specimen surface should result in discrete displaced spots, not continuous streaks [252]. The side-facet angle of droplet-epitaxial GaAs QD, measured by AFM method, corresponds ca. with the half angle between the two chevron-tails [194][15]. The angle between two RHEED streaks starting from same reciprocal lattice point is about 55° as shown in Fig. 5.13. (upper part of column D).

The observed RHEED pattern can be recognized by the product of square modulus of the separate Fourier-transformation of the periodic constituents. In this case the intensity pattern is proportional with the product of intensity originated from transmission and from the pyramidal hut. A lucid explanation of the observed RHEED pattern and the temporal evaluation of QDs can be shown in Fig. 25.14.

### 5.6.3. RHEED Interpretation for QR Structure

The change of the RHEED pattern during the evolution of QR can be followed in the lower part of Fig. 5.13. The sharp streaks (column A) become diffuse on the RHEED screen, when Ga shutter is opened without any As

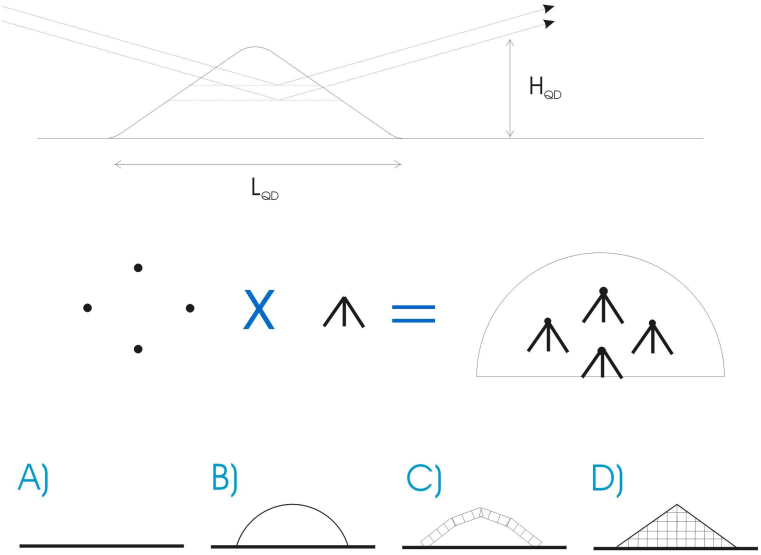

5.14. Fig. Scattering of grazing electron beam on QD. Upper part: Geometrical arrangement of scattering on several crystal planes in QD. Transmission character dominate here. Middle part: The observed RHEED pattern originate from the product of the diffraction intensity from a crystal cluster and from a pyramid. The influence of the open (001) surface is neglected. Lower part: Temporal evaluation of QD in step by step manner (see Fig. 5.13.).

background (column B). This effect can be explained, similarly to the explanation in the former case, with the appearance of the liquid Ga droplets on the surface. The annealing phase begins after the offering of As component with the pressure of $4{\times}10^{-6}$ Torr, while the substrate temperature is 300 °C. This process takes about five minutes. During the annealing, a typical RHEED pattern is formed, shown in the lower last frame in Fig. 5.13. This pattern consist of a streak with spots. The crystal structure and the form of the nano specimen influence together the RHEED pattern. Theoretically, the QR structure can be produced with the help of a disc structure from which a concentric disc of smaller diameter is removed. With the help of this idea, the diffraction pattern of the ring can be determined. The diffraction pattern of the ring originates from the superposition of positive and negative discs.

The volume of the QDs are large enough to receive transmission pattern during the electron scattering. The main lateral expansion $L_{QD}$ and height

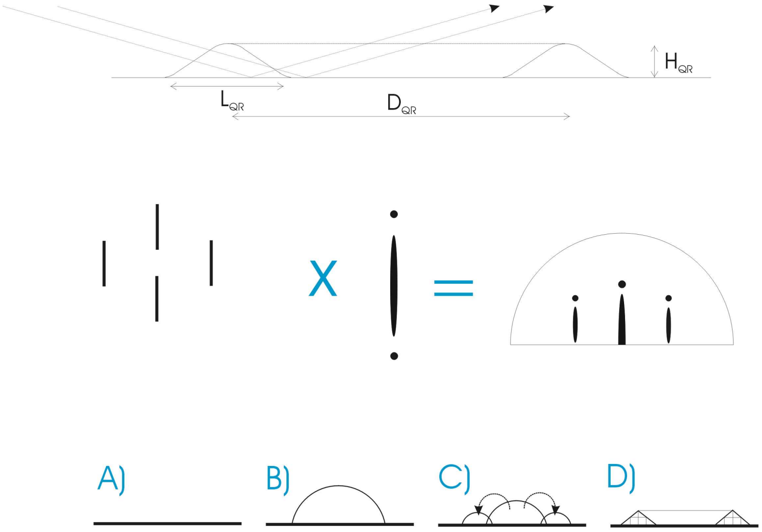

5.15. Fig. Scattering of grazing electron beam on QR. Upper part: Geometrical arrangement of scattering on several crystal plane in QR or on two-dimensional basis plane. Either transmission or reflection character dominate depending on the finite size. Middle part: The product of transmission- or reflection-like intensity and the scattering from rotational-shaped object results the near same RHEED pattern. The influence of the open (001) surface is neglected. Lower part: Temporal evaluation of QR in step by step manner (see Fig. 5.13.).

$H_{QD}$ of QD - according to the AFM measurement - are 50 and 5 nm, respectively (see Fig. 5.14.). The mean free path of the electrons $\Lambda$ in GaAs between the crystal planes without collosion at the typical incidence angle of RHEED (about $2°$) is less than 20 nm. So, in our case, there are several (ca. 9) lattice planes to receive transmission character. The situation in the QR is different. (The mean diameter of the principal ring $D_{QD}$ is 60 nm.) The thickness of the ring $L_{QR}$ - according to the AFM measurement - is 20 nm and the height $H_{QR}$ is 2 nm (see Fig. 5.15). In this case the measure of $L_{QR}$ is comparable with $\Lambda$ and the height $H_{QR}$ consists only few planes. This is a marginal case where the dominant character of the diffraction pattern can be either transmission-like or reflection-like. The QR production takes a long time during the annealing phase. The As background pressure is low here. So, the process of crystallization is slow. In this case, the liquid condition remains for a longer time, so there is enough time for the material transport, which leads to the formation of QR [209, 211]. Because, the crystallization occurs mainly after the transport process, only that can be demonstrated in the RHEED picture. Intermediate stages - because these happen mostly in amorphous state - provide the same diffuse RHEED pictures. The resulted RHEED picture is originated from the product of the reflection/transmission image and the diffraction image of the rotational-shaped object.

## 5.7. Study of the Electronic Structure

### 5.7.1. Photoluminescence Studies on QD and QR Structures

In this section, we focus on the photoluminescence (PL) properties of the droplet epitaxial non-covered QDs and QRs. The 4 K PL spectra of the QD sample and the temperature dependent PL spectra of the QR sample are shown in Figs 5.16 and 5.17, respectively. At 4 K, three peaks can be seen on the QD spectrum. They can be identified as bound exciton (1.5129 eV) (its intensity is very low), the exciton bound to acceptor line (1.4919 eV) and its longitudinal optical phonon replica (1.4585 eV). At 4 K, the QR spectrum has five peaks. They can be explained as bound exciton (1.5129 eV), exciton bound to acceptor (1.4892 eV) and its longitudinal optical phonon replica (1.4577 eV). Further on at higher energies two peaks appear (1.5308 and 1.5602 eV). The PL spectra were also recorded as a function of temperature. To verify the identification of the peaks, the temperature dependence of the band gap energy of GaAs and that of the bound exciton were compared. A good correlation was found, (see Fig 5.18/A).

It can be seen, that for the QD no peak was found at energy higher than the bound exciton, but two peaks appeared for the QR, due the quantum effects. In the following this phenomenon will be explained.

Our nano-structures were prepared without a cap layer. The nano-structures described in the literature are either self supported or confined in another material. For practical differentiation, the phenomenon in the first one is called quantum size effect and in the second one quantum confinement, although theoretically the phenomenon is the same. Our nano structures are located somewhere between these two. According to Viswanatha et al.'s calculations a perceptible band gap change in the case of GaAs nano-crystals begins un-

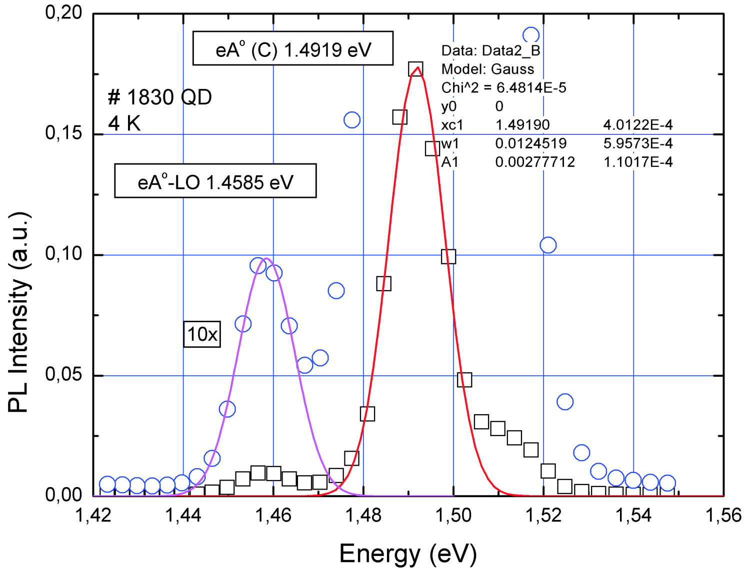

5.16. Fig. The PL spectrum of the QDs, where no levels are observable over the bounded exciton.

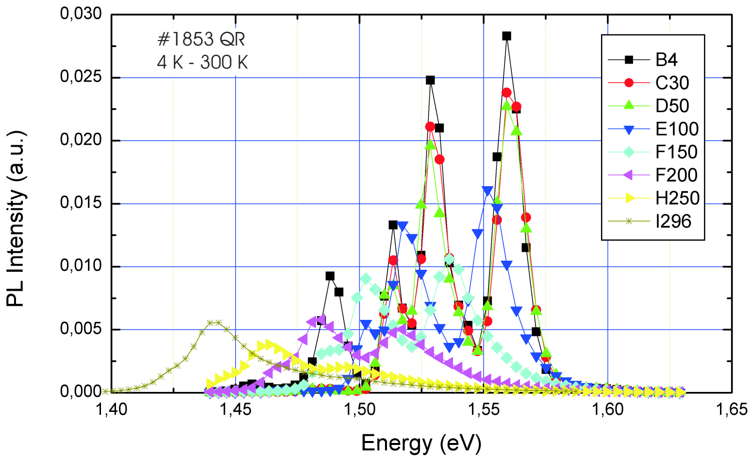

5.17. Fig. The PL spectrum of the QRs, where two levels are observable over the bounded exciton (details see in the text).

der the diameter ($d_n$) size 7 nm [260]. The base diameter of the QD ($d_{QD}$) investigated was much larger, and its height ($h_{QD}$) was also larger, but comparable. So, here no quantum effects are expected (compare Fig. 1C and Fig. 5.18/B). Therefore it was impossible to detect a peak shift or peak broadening for QD. For QR the laterally wide ($d_{QR}$) nano-structure had a height ($h_{QR}$) significantly less than 7 nm, consequently the supposition of quantum confinement produces proper result [261]. Fig. 5.18./C shows the calculated energy quantization of GaAs quantum well con-fined among AGaAs barriers. This corresponds well to the PL peaks of the QR at a higher energy level than that of the bound exciton.

### 5.7.2. Explanation of the PL Peak Width

Remarks concerning the width of the photoluminescence peaks of QD and of QR: During a PL measurement the laser beam is focused to the material irradiating a spot with a diameter of about 200 $\mu$m, resulting in the simultaneous excitation of several nano-structures. The PL spectra show characteristic peak width, depending on the temperature and the size distribution of these structures. At the same temperature a broader size variation results in a broader PL peak. Mano et al. investigated the PL peaks of QRs [275] and found that under similar growth conditions the Full Width at Half Maximum (FWHM) is significantly narrower (less than one third) than that of the QDs. This comparison was based on the works of Watanabe et al. [259]. They reasoned that the variation of the size distribution of the QRs is smaller than the same parameter of the same parameter of the QDs, producing the great difference in the FWHM [275].

In our opinion this difference can be explained by other facts. As it is known, both the QR and the QD is shaped from a gallium droplet. Assume that the volume and its variation of the initial droplets are the same in both cases. The facet of the nanostructures is size dependent and cannot be arbitrarily sized [194]. For the QD let's start from the greater (111) facet (the approx. diameter ($2r$) is 100 nm [194], see Fig. 5.19). For the QR only the (113) facet can be taken into account because of the smaller volume (the approximate width ($w$) is 60 nm [194], see Fig. 5.18.) dedicated to a circle segment (see the RHEED patterns and line scans in Ref. [?]). Due to the crystallographic constraints the geometry of the formed QDs and QRs are determined. The height-to-diameter ratio cannot be arbitrary; it can be defined by a single parameter.

If $r$ is the radius of the base circle belonging to the initial droplet the volume of the developing QD, as a function of r, is given by V = $1.58\times r^3$.

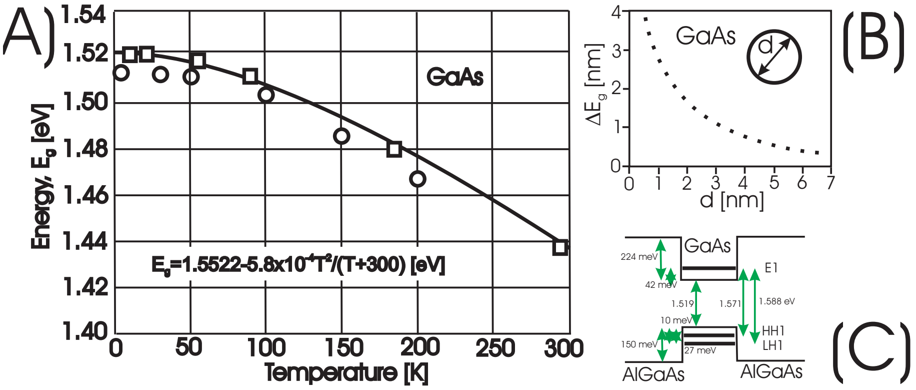

5.18. Fig. (A) The PL spectrum of the QDs, where no levels are ovservable over the bounded exciton. (B) The Eg variation on the nanocrystal size (dn) using the approximation based on quantum size effect [16]. (C) The scheme of the energy bands, using the approximation based on quantum confinement [17].

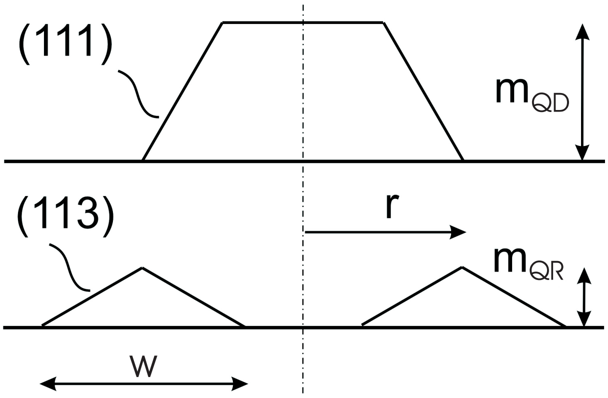

5.19. Fig. Explanation to the difference of the FWHM of the PL peaks in the case of QDs and QRs (see in the text).

For the QR, from the equality of the volumes, the w parameter can be calculated as w $= 0.71\times r$ (see Fig 5.19.). (This means that the nano-object with parameter of $2r = 100$ nm has (111) facets, and the other one with parameter of $w = 0.71 \times 100 \sim 70$ nm or less has (113) facets. It corresponds to the above presented measured data.) As was shown above, the height of the nano-structure influences the quantum behaviour. The heights of the QD and QR structures can be expressed as a function of their volumes: $m_{QD} = V^{1/3}/1.34$ and $m_{QR} = V^{1/3}/6.56$, respectively. Assuming the same variations of the volumes, it can be seen that the variation of the height for QR is much smaller than for QD, consequently the corresponding FWHM of the PL peak is smaller [262].

## 5.8. Inverted Quantum Dot

### 5.8.1. Preliminaries to the Study

A further very recent method for the fabrication of strain-free QDs is the local droplet etching (LDE) of nano-holes (NHs) and their subsequent filling [276]. The resulting nano-structure is called inverted QD. In contrast to the droplet epitaxy, the LDE process takes place at optimum MBE growth temperatures and we expect here an only very low level of crystal defects. The LDE nano-holes are created in a self-organized fashion by local material removal [277, 278, 279, 280, 281]. For NH-QD fabrication, nano-holes are generated using Al droplets on AlAs substrates. A previous study on nano-hole etching with Ga droplets has shown that the walls surrounding the nano-hole openings are crystallized from droplet material and form GaAs quantum rings [285]. In order to avoid such an additional confinement by the walls, in the present experiments we use Al droplets. Subsequently, the holes are filled with a GaAs layer to form GaAs NH-QDs of controlled height [276, 282, 283].

In this paper, we discuss cross-sectional transmission electron microscopy (TEM) investigations of such GaAs NH-QDs formed by filling of nano-holes after droplet etching. The high-resolution TEM images are combined with elemental maps of the relevant species.

A previous photoluminescence (PL) spectroscopy study [284] of this sample shows lines with a full width at half-maximum (FWHM) of the ground-state transition of only 13 meV at 8 K. This very sharp PL line demonstrates the high uniformity of NH-QD ensembles. In addition, the PL data of Ref. [284] establish room temperature emission from the GaAs QDs. These data demonstrate the high optical quality of the NH-QDs. Now, the present TEM study of single NH-QDs provides details of the structure and composition of this interesting QD system (5.20.Fig.).

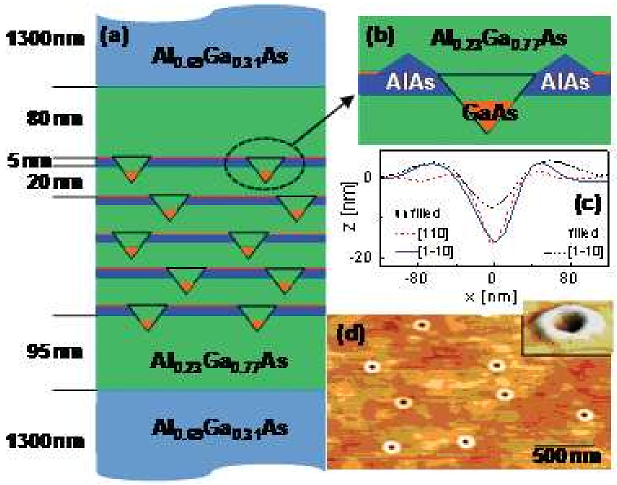

5.20. Fig. Scheme of the sample cross-section with 5 stacked layers of GaAs NH-QDs fabricated by partial filling of droplet etched nano-holes. b) Magnified scheme of a single NH-QD. c) AFM line-scans of reference nano-holes etched using Ga droplets in AlGaAs with and without subsequent filling. d) Top view of a reference AlGaAs surface with nano-holes after etching with Al droplets. The inset shows a 3D AFM image of a single nano-hole. Clearly visible is the wall surrounding the hole opening.

## 5.8.2. Structural Investigation of the Inverted QD

A cross-sectional TEM image showing an overview of a NH-QD is visible in Fig. 5.21. A scheme of the structure is shown in Figs.1a and b. The contrast caused by the different atomic numbers allows the distinction between AlAs (brighter) and AlGaAs/GaAs (darker) regions. Clearly visible are the thin AlAs and the thicker $Al_{0.23}Ga_{0.77}As$ layers. The measured thickness of the AlAs layers is 5.5 nm and that of the $Al_{0.23}Ga_{0.77}As$ layers is 19.5 nm. Both values agree well with the respective layer thicknesses of 5 and 20 nm expected from the calibration of the MBE beam fluxes. The most interesting feature of Fig. 5.21 is the inverted GaAs NH-QD that is visible in the middle of the image. The NH-QD is clearly identified by the gap in the AlAs layer. This gap is caused by the removal of the AlAs during droplet etching and its replacement with GaAs and $Al_{0.23}Ga_{0.77}As$ during filling. Very importantly, both, Fig.2 and the high-resolution image of Fig. 5.22 indicate that no crystal defects or dislocations have been formed inside and in the surrounding of the NH-QDs. This result directly proves that the NH-QDs are defect-free. Previous photoluminescence (PL) measurements support this result only indirectly. There, the PL intensity from an ensemble of NH-QDs shows no increase after rapid thermal annealing of the sample [284]. The TEM view graphs also reveal that in contrast to the case of InAs-QDs no strain pattern is surrounding the dots [286].

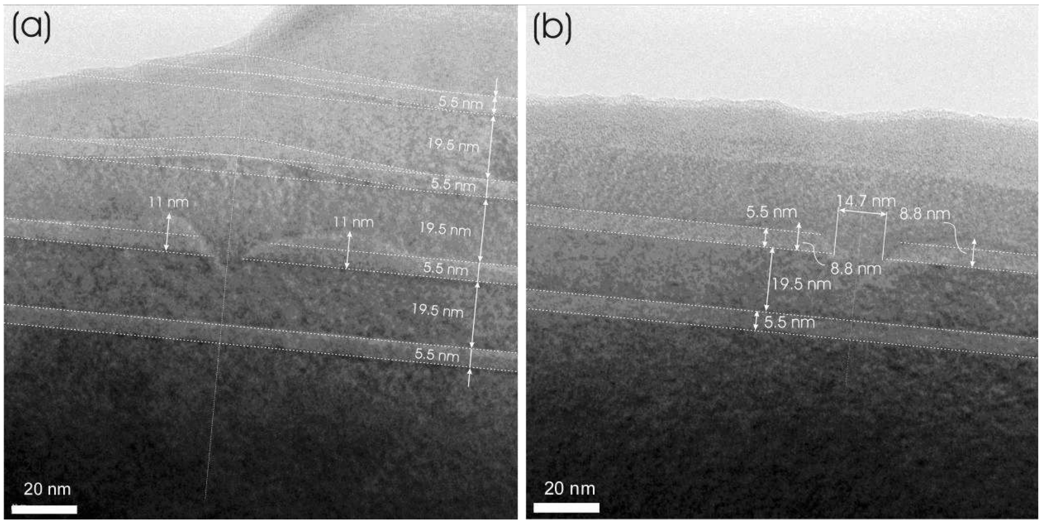

5.21. Fig. (a)TEM picture of an inverted NH-QD and its environment. The lines serve as guides to eye to recognize the structures. The structures consists of a AlAs (5.5 nm) / AlGaAs (19.5 nm) super-lattice with a NH-QD in the center.(b) second NH-QD.

### 5.8.3. Some Aspects to the Formation

Furthermore, the TEM images of Figs. 5.21. and 5.22. show a thickening of the AlAs layer in the surrounding of the nano-hole. Elementary maps taken using electron energy loss spectroscopy (EELS) confirm that the thickened regions consist of AlAs (Fig. 5.23). We identify the additional AlAs on top of the flat AlAs layer as the wall that surrounds the nano-hole opening. The formation of such walls has already been observed earlier during etching of AlGaAs with Ga droplets [279]. A typical AFM image of a nano-hole with wall after Ga LDE is shown in the inset of Fig. 5.20. Importantly, previous photoluminescence measurements establish that the walls formed using Ga

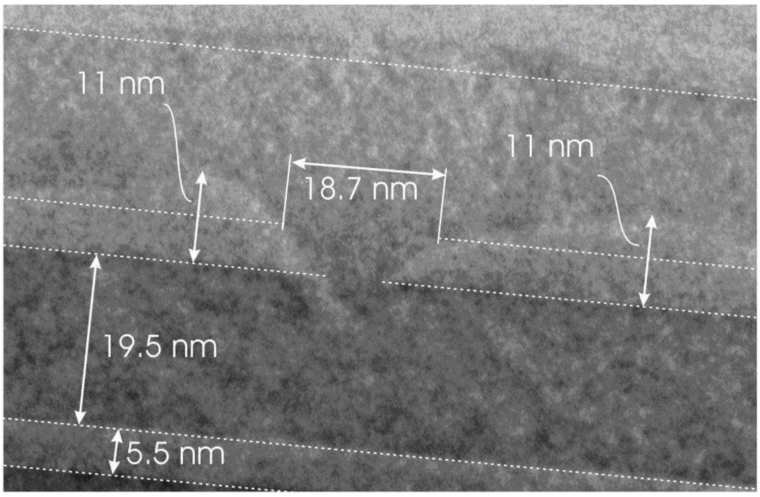

5.22. Fig. High resolution TEM picture of the NH-QD from Fig. 5.21.(a).

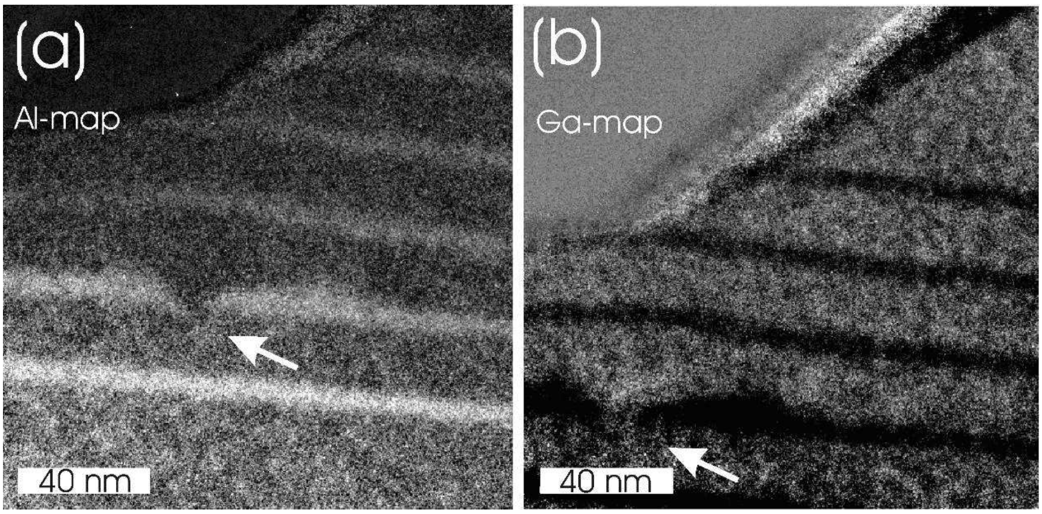

5.23. Fig. Composition of the inverted QD determined with the electron energy loss spectroscopy (EELS) (a) Al-L map and (b) Ga-M map. The arrows marks the NH-QD.

droplets consist of GaAs [285]. Basing on this experimental finding, a recent model of droplet etching and wall formation [281] assumes that the walls are crystallized from droplet material and arsenic from the substrate. However, so far, this effect has not been confirmed for etching with Al droplets. As a key result, the present TEM study clearly establishes that also for etching with Al droplets the walls crystallize from droplet material and, thus, that the basic mechanism of droplet etching is equal for both droplet materials.

Furthermore, Fig. 5.22. shows that the next AlAs layer grown on top of the NH-QDs layer is bended upwards at the location of the NH-QD, resulting in the formation of a kind of hill. The slope of this hill agrees approximately with the slope of the wall around the nano-hole and, thus, reflects the additional material incorporated there. On the other hand, the hill shows no indentation in the center. This interesting result establishes that the nano-hole has been completely filled before overgrowth with the AlAs layer.

A clear determination of the shape of the GaAs NH-QDs is difficult due to the small Al content in the surrounding $Al_{0.23}Ga_{0.77}As$ barrier material and the thus only weak contrast. Since no reliable AFM profiles of nano-holes on the highly reactive AlAs surface exist (see above), we compare the present TEM data with reference holes etched with on AlGaAs surfaces [276, 279]. There, a typical angle between the planar surface and the nano-hole side-facets of approximately 20° was determined. Interestingly, the side-facets visible in the present TEM images seem to be steeper. However, for a quantitative analysis, a better statistics and measurements of a larger number of NH-QDs are desirable.

# Bibliography

[1] T. Steiner: Semiconductor Nanostructures for Optoelectronic Applications; Artech House INC (2004)

[2] M. J. Kelly: Low-dimensional Semiconductors; Materials, Physics, Technology, Devices; Clarendon Press, Oxford (1995)

[3] M. Jaros: Physics and Applications of Semiconductor Microstructures; Clarendon Press, Oxford (1989)

[4] B. R. Nag: Physics of Quantum Well Devices; Kluwer Academic Publisher, London (2000)

[5] D. H. Navon: Semiconductor Microdevices and Materials; CBS Publ. Asia LTD, New York (1987)

[6] K. Barnham, D. Vvedensky: Low-dimensional Semiconductor Structures, Fundamentals and Device Applications; Cambridge Univ. Press (2001)

[7] M. Reed: Nanostructured Systems (Semiconductors and Semimetals vol. 35) Acad. Press INC., Boston (1992)

[8] A. C. Gossard: Epitaxial Microstructures (Semiconductors and Semimetals vol. 40) Acad. Press INC., Boston (1994)

[9] Á. Nemcsics: Solar Cells and their Developing Perspective (in Hungarian) Akadémiai Kiadó, Budapest (2001)

[10] Á. Nemcsics; Fizikai Szemle 56 (2006) 293

[11] Á. Nemcsics; Elektronikai Technológia, Mikrotechnika 48 (2009) 39

[12] E. Knill, R. Laflamme, G. J. Milburn; Nature 46 (2001) 409

[13] J. Stolze, D. Sater: Quantum Computing; Wiley-VCH, Weinheim (2004)

[14] V. Vedral: Introduction to Quantum Information Science; Oxford University Press, Oxford (2006)

[15] H. Welker; Z. Naturforsch 7a (1952) 744

[16] O. Madelung: Physics of III-V Compounds; John Willey and Sons. Inc., New York (1964)

[17] J. S. Blakemore; J. Appl. Phys. 53 (1982) R123

[18] M.G. Astles: Liquid-Phase Epitaxial Growth of III-V Compound Semiconductor Materials and their Device Applications; Adam Hilger, New York (1990)

[19] P. Capper, M. Mauk: Liquid Phase Epitaxy; Wiley-VCH, Berlin (2007)

[20] S. Dhar; Bull. Mater. 28 (2005) 349

[21] F. Bantien, E. Bansen, J. Weber; J. Appl. Phys. 61 (1987) 2803

[22] N. Nakamura, K. Aiki, J. Umeda, A. Yariv, W. M. Yen, T. Morikawa; Appl. Phys. Lett. 24 (1974) 406

[23] T. J. Anderson; Microel. Processing 221 (1989) 105

[24] D. Alexiev, D. A. Prokopovich, S. Thomson, L. Mo, A. B. Bosenfeld, M. Reinhard; Condensed Matter 88 (2004) 8

[25] H. Nelson; J. Cryst. Growth 27 (1974) 1

[26] G.B. Stringfellow; J. Cryst. Growth 27 (1974) 21

[27] M. B. Small, I. Crossley; J. Cryst. Growth 27 (1974) 35

[28] L. R. Dawson; J. Cryst. Growth 27 (1974) 86

[29] D. E. Aspnes; Surf. Sci. 132 (1983) 406

[30] R. O. Carlson, G. A. Slack, S. J. Silverman; J. Appl. Phys. 36 (1965) 505

[31] A. P. Dmitriev, M. P. Mikhailova, I. N. Yassievich; Phys. Stat. Sol. (B) 140 (1987) 9

[32] S. M. Sze: Physics of Semiconductor Devices, John Wiley and Sons, New York (1981)

[33] V. P. Varshni; Phys. Stat. Sol 19 (1967) 459

[34] V. P. Varshni; Phys. Stat. Sol 20 (1967) 9

[35] M. J. Howes, D. V. Morgan: Gallium Arsenide: Materials, Devices, and Circuits; John Willey and Sons; Chichester (1985)

[36] B. A. Joyce, J. H. Neave, J. Zhang, P. J. Dobson; in Reflection High-Energy Electron Diffraction and Reflection Electron Imaging of Surfaces; NATO ASI Ser. 188, Plenum Press New-York (1988) 397

[37] B. A. Joyce, D. D. Vvedensky; in: Quantum Dots, Fundamentals, Applications and Frontiers; Springer, Dorndrecht (2005) 1

[38] H.Yamaguchi, Y. Horikosi; Phys. Rev. B 51 (1995) 9836

[39] C. T. Foxon, B. A. Joyce; Surf. Sci. 50 (1975) 434

[40] C. T. Foxon, B. A. Joyce; Surf. Sci. 64 (1977) 293

[41] J. H. Neave, P. K. Larsen, J. F. van der Veen, P. J. Dobson, B. A. Joyce; Surf. Sci. 133 (1983) 267

[42] Y. Fukunishi, H. Nakatuji; Surf. Sci. 291 (1993) 271

[43] E. S. Tok, J. H. Neave, F. E. Allegretti, J. Zhang, T. S. Jones, B. A. Joyce; Surf. Sci. 371 (1997) 277

[44] E. S. Tok, J. H. Neave, J. Zhang, B. A. Joyce, T. S. Jones; Surf. Sci 374 (1997) 397

[45] R. Venkatasubramanian, V. K. Pamula, D. L. Dorsey; Appl. Surf. Sci. 104/105 (1996) 448

[46] A. Suda, N. Otsuka; Surf. Sci. 458 (2000) 162

[47] B. A. Joyce; in Two Dimensional Systems: Physics and New Devices, Springer Ser. (Solid State Sci. 67) Springer-Verlag, Heidelberg (1986)

[48] Á. Nemcsics, J. Olde, M. Geyer, R. Schnurpfeil, R. Manzke, M. Skibowski; Phys. Stat. Sol. A 155 (1996) 427

[49] Acta Politechn. Hung. 4 (2007) 117

[50] W. Braun, L. Däweritz, K. H. Plogg; Phys. Rev. Lett. 80 (1998) 4935

[51] W. Braun: Applied RHEED, Reflection High-Energy Electron Diffraction during crystal growth; Springer-Verlag, Berlin (1999)

[52] Z. Mitura, S. L. Dudarev, M. J. Whelan; Phys. Rev. B 57 (1998) 6309

[53] Z. Mitura; Phys. Rev. B 59 (1999) 4642

[54] Z. Mitura, S. L. Dudarev, M. J. Whelan; J. Cryst. Growth 198/199 (1999) 905

[55] J. M. McCoy, U. Korte, P. A. Maksym, G. Meyer-Ehmsen; Phys. Rev. B 48 (1993) 4721

[56] Á. Nemcsics; J. Cryst. Growth 217 (2000) 223

[57] Q.-K. Xue, T. Hashizume, T. Sakurai; Prog. Surf. Sci. 56 (1997) 1

[58] M. Witte, G. Meyer-Ehmsen; Surf. Sci. 326 (1995) L449

[59] J. M. McCoy, U. Korte, P. A. Maksym; Surf. Sci. 418 (1998) 273

[60] F. Bastimann, A. G. Cullis, M. Hopkinson; Surf. Sci. 603 (2009) 2398

[61] K. Shiraishi, T. Ito; Appl. Surf. Sci. 121/122 (1997) 98

[62] S. Tsukamoto, N. Koguchi; J. Cryst. Growth 209 (2000) 258

[63] A. Ohatke: Surface reconstruction on GaAs(001); Surf. Sci. Rep. 63 (2008) 295-327

[64] B. A. Joyce, D. D. Vvedensky; Mat. Sci. Eng. R 46 (2004) 127

[65] W. A. Harrison: Electronic tructure and the properties of Solids - The Physics of the Chemical Bond; W. H. Freeman and company, San Francisco (1980)

[66] C. B. Duke; Chem. Rev. 96 (1996) 1237

[67] M.D.Phashley; Phys. Rev. B 40 (1989) 10481

[68] C. Deparis, J. Massies; J. Cryst. Growth 108 (1991) 157-172

[69] M. A. Herman, H. Sitter: Molecular Beam Epitaxy - Fundamentals and Current Status; Springer-Verlag, Berlin (1989)

[70] J. F. O. Hanlon: Uses Guide to Vacuum Technology; Wiley-Interscience, New York (1989)

[71] N. N. Ledentsov: Growth Process and Surface Phase Equilibria in Molecular Beam Epitaxy; Springer Verlag, Berlin (1999)

[72] H. Lüth: Surfaces and Interfaces of Solid Materials; Springer Verlag, Berlin (1998)

[73] W. S. Ruska: Microelectronic Processing; McGraw-Hill, New York (1988)

[74] E. S. Yang: Microelectronic Devices; McGraw-Hill, New York (1988)

[75] S. M. Sze: VLSI Technology; McGraw-Hill, New York (1988)

[76] M. Wautelet, D. B. Beljonne, J.-L. Brédas, J. Cornil, R. Lazzaroni, P. Lecĺere, M. Alexandre, P. Dubois, P. Gills, Y. Gossuin, R. Muller, A. Ouakssim, A. Roch, D. Duvivier, J. Robert, R. Gouttebaron, M. Hecq, F. Monteverde: Nanotechnologie; Oldenbourg Verlag, München (2003)

[77] M. Henzler, W. Göpel: Oberflächenphysik des Festkörpers; Teubner, Stuttgart (1991)

[78] Á. Nemcsics, I. Réti, V. Kulin, R. Hodován, J. Gábor, G. I. Taar, J. Pántos, J. Bozsik, S. Molnár, G. Szenczi: Proc. of XXIV Int. Kandó Conf. (2008) 4

[79] Á. Nemcsics, I. Réti, M. Serényi, G. V. Tényi, R. Hodován, J. Gábor, I. G. Taar, J. Pántos, J. Bozsik, S. Molnár, M. R. Jankóné: Mikrotechnika 48 (2009) 33

[80] Á. Nemcsics, I. Réti, G. V. Tényi, P. Kucsera, L. Tóth, P. Harmat, A. Mieville, M. Csutorás, B. Kupás-Deák, T. Sándor, J. Bozsik: Gép 61 (2010) 29

[81] Á. Nemcsics, M. Csutorás, G. V. Tényi, T. Sándor: Proc. of 8th Int. Symp. on Inelligent Systems SISY 2010 Sept. 10-11, Subotica, Serbia; 631

[82] P. Kucsera, G. V. Tényi, Á. Nemcsics, I. Réti: Proc. of 8th Int. Symp. on Inelligents Systems SISY 2010 Sept. 10-11, Subotica, Serbia; 659

[83] M. Csutorás, Á. Nemcsics, T. Sándor: Proc. of XXXVI Int. Kandó Conf. 2010 nov 4-5, Budapest; 10

[84] I. Réti, Á. Nemcsics, P. Harmat, L. Tóth, G. V. Tényi, P. Kucsera, B. Kupás-Deák, A. Mieville, R. Hodován, P. Turmezei, S. Mészáros, G. Battistig, I. Bársony: Proc. of XXXVI Int. Kandó Conf. 2010 nov 4-5, Budapest; 7

[85] G. V. Tényi, Á. Nemcsics, P. Kucsera, I. Réti: Proc. of XXXVI Int. Kandó Conf. 2010 nov 4-5, Budapest; 11

[86] Á. Nemcsics, J. Olde, M. Geyer, K. Resföft: Instruments and Experimental Techniques 48 (2005) 679

[87] Á. Nemcsics; in Quantum Dots: Fundamentals, Applications, and Frontiers Eds. B. A. Joyce, P. C. Kelires, A. G. Naumovets, D. D. Vvedensky, NATO Sci. Ser. II. Mat., Phys. and Chem. - Vol 190 Springer Dodrecht (2005) 221

[88] S. Clarke, D. D. Vvdensky; Phys. Rev. Lett. 58 (1987) 2235

[89] Y. Namba, R. W. Vook, S. S. Chaoo; Surf. Sci. 109 (1981) 320

[90] J. Zhang, J. H. Neave, P. J. Dobson, B. A. Joyce; Appl. Phys. A 42 (1987) 317

[91] B. A. Joyce, P. J. Dobson, J. H. Neave, K. Woodbridge, J. Zhang, P. K. Larsen, B. Bölger; Surf. Sci. 168 (1986) 423

[92] T. Kawamura, P. A. Maksym, T. Iijima; Surf. Sci. 148 (1984) L671

[93] P. K. Larsen, P. J. Dobson, J. H. Neave, B. A. Joyce, B. Bölger, J. Zhang; Surf. Sci. 169 (1986) 176

[94] Á. Nemcsics, Sz. Nagy; Vacuum (2011) available on line (2011)

[95] O. Brümmer, J. Heydenreich, K. H. Krebs, H. G. Schneider: Festkörperanalyse mit Elektronen, Ionen und Röntgenstrahlen, Deutscher Verlag der Wissenschaften, Berlin (1980)

[96] O. Klemperer: Electron Physics, Butterworths, London (1958)

[97] Y. Horikoshi, H. Yamaguchi, F. Briones, M. Kawashima; J. Cryst. Growth 105 (1990) 326

[98] Á. Nemcsics, L. Petrás, K. Somogyi; Vacuum 41 (1990) 1012

[99] Y. Ishibashi; J. Phys. Soc. Japan 60 (1991) 3215

[100] B. A. Joyce; in: Two dimensional systems: Physics and New Devices; G. Bauer, F. Kucher, H. Heinrich (Eds.); Springer Verlag, Heidelberg (1986)

[101] Á. Nemcsics, J. Olde, M. Geyer, R. Schnurpfeil, R. Manzke, M. Skibowski. Physica Status Solidi A 155 (1996) 427-43

[102] C. S. Lent, P. I. Cohen. Surface Science;139 (1984) 121

[103] K. D. Jamison, J. S. Resh, C. C. Horton, A. Bensaoula, A. Ignatiev; Journal of Vacuum Science and Technology B; 8 (1990) 279

[104] W. Braun, L. Däweritz, K. H. Plogg. Physical Review Letters;80 (1998) 4935

[105] S. L. Dudarev, D. D. Vvedensky, M. J. Whelan. Physical Review B; 50 (1994) 14525

[106] J. H. Neave, B. A. Joyce, P. J. Dobson, N. Norton. Applied Physics A; 31 (1983) 1

[107] P. J. Dobson, B. A. Joyce, J. H. Neave, J. Zhang. Journal of Crystal Growth;81 (1987) 1

[108] B. A. Joyce. Journal of Crystal Growth; 99 (1990) 9

[109] J. L. Beeby. Surface Science; 80 (1979) 56

[110] Á. Nemcsics. Journal of Crystal Growth; 217 (2000) 223

[111] S. Dürr, T. Nonn, G. Rempe. Nature; 395 (1998) 33

[112] M. Buchanan. New Scientist; 2176 (1999) 25

[113] M. Arndt, A. Zeilinger. Physikalische Blätter; 56 (2000) 69

[114] J. S. Resh, K. D. Jaminson, J. Strozier, A. Bensaoula, A. Ignatiev; Phys. Rev. B 40 (1989) 11799

[115] J. Griesche, N. Hoffmann, M. Rabe, K. Jacobs; Progress in Crystal Growth and Characterization of Materials 37 (1998) 103

[116] Á. Nemcsics; Thin Solid Films 367 (2000) 302

[117] J. Takacs: Mathematics of Hysteretic Phenomena - The T(x) Model for the Description of Hysteresis; Wiley-VCH Verlag GmbH, Weinheim (2003)

[118] M. Witte, G. Meyer-Ehmsen; Surf. Sci. 326 (1995) L449

[119] C. Deparis, J. Massies; J. Cryst. Growth 108 (1991) 157

[120] J. F. van der Veen, L. Smir, P. K. Larsen, J. H. Neave; Physica B 117 (1983) 822

[121] J. Takács; Int. Comp. El. 20 (2000) 2002

[122] L. K. Varga, Gy. Kovács, J. Takács; J. Magn. Mater 320 (2008) L26

[123] Á. Nemcsics, J. Takács; Acta Polytechn. Hung. 7 (2010) 109

[124] Á. Nemcsics, J. Takács, J. Bozsik; Proc. of 8th Int. SISY 2010 Sept. 10-11 (2010), Subotica, Serbia 389

[125] Á. Nemcsics, J. Takács; Semiconductors, 45 (2011) 93

[126] E. A. Fitzgerald; Mater. Sci. Rep. 7 (1991) 87

[127] N. Grandenjan, J. Massies; J. Cryst. Growth 134 (1993) 51

[128] Á. Nemcsics; in Proc. of IWPSD on Physics of Semiconductor Devices, Allied Publ. Ltd., Delhi (1999) 264

[129] J. W. Matthews, Epitaxial Growth, Acad. Press New York (1975)

[130] M. U. González, Y. González, L. González; E-MRS Spring Meeting, Strassbourg (2001) 1

[131] Á. Nemcsics; Appl. Surf. Sci. 190 (2002) 294

[132] Á. Nemcsics; Thin Solid Films 367 (2000) 302

[133] Á. Nemcsics, F. Riesz, J. Szabó, Z. E. Horváth, S. Gurbán; Phys. Stat. Sol. A 177 (2000) 231

[134] Á. Nemcsics, F. Riesz; (MRS Spring Meeting, April 24-28 2000 San Francisco, California) Mat. Res. Soc. Symp. Proc. 618 (2000) 225

[135] Á. Nemcsics, F. Riesz; Crystal Research and Technology 36 (2001) 1011

[136] Á. Nemcsics, J. Olde, M. Geyer, K. Resföft; Instruments and Experimental Techniques 48 (2005) 679

[137] Á. Nemcsics; Semiconductors 39 (2005) 1352

[138] F. Riesz, J. Z. Domagala, Á. Nemcsics; Phys. Stat. Sol. C 2 (2005) 1298

[139] Á. Nemcsics; Acta Politechnica Hungarica 4 (2007) 117

[140] Á. Nemcsics, M. Schuszter, L. Dobos, P. Turmezei; Proc. of 6th Int. SISY Sept. 26-27 (2008) Subotica, Serbia 1

[141] Á. Nemcsics, M. Schuszter, L. Dobos, P. Turmezei; Acta Polytechnica Hungarica 6 (2009) 95

[142] M. M. Faktor, J. L. Stevenson; J. Electrochem Soc. 125 (1978) 621

[143] Á. Nemcsics, K. Somogyi; Acta Phys. Hung. 70 (1991) 259

[144] T. Ambridge, M. M. Faktor; J. Appl. Electrochem. 5 (1975) 319

[145] Á. Nemcsics, L. Petrás, K. Somogyi; Vacuum 41 (1990) 1012

[146] J. E. Ayers; J. Appl. Phys. 78 (1995) 3724

[147] K. Ishida, M. Akiyama, S. Nishi; Jpn. J. Appl. Phys. 26 (1987) L163

[148] G. MacPherson, P. J. Goodhew, J. Appl. Phys. 80 (1996) 6706

[149] K. H. Chang, R. Gibala, D. J. Srolovitz, P. K. Bhattacharya, J. F. Mansfield; J. Appl. Phys. 67 (1990) 4093

[150] Á. Nemcsics; Ext. Abstr. of 7th Joint Vacuum Conf, May 26-29, (1997), Debrecen, (Ed. S. Bohátka) 163

[151] Á. Nemcsics, L. Dobos, L. Dávid L; Acta Technica, 108 (1999) 521

[152] R. Kinder, Á. Nemcsics, R. Harman, F. Riesz, B. Pécz; Proc. of 2nd Int. Conf. on Advanced Semicond. Devices and Microsystems, Smolenice Castle, Slovakia, 5-7 Oct. (1998), (Eds J. Breza, D. Donoval, V. Dorobny, F. Uherek) 215

[153] Á. Nemcsics, L. Dobos, B. Kovács, I. Mojzes; Proc. of 2nd Int. Conf. on Advanced Semicond. Devices and Microsystems, Smolenice Castle, Slovakia, 5-7 Oct. 1998, (Eds J. Breza, D. Donoval, V. Dorobny, F. Uherek) 39

[154] Á. Nemcsics, L. Dobos; Proc. of Heterostructure Epitaxy and Devices (eds. P. Kordos, J. Novák) NATO Science Series 3. High Technology 48 Kluwer Acad. Publ. Dordrecht (1998) 135

[155] Á. Nemcsics; Proc. of A ma és holnap fizikája Magyarországon, Fizikus Vándorgyűlés, Gödöllő, Aug. 25-28. (1998) (Ed. G. Pásztor) ELFT, Budapest, 239

[156] Á. Nemcsics; Phys. Stat. Sol. A 173 (1999) 405

[157] Á. Nemcsics, F. Riesz, L. Dobos; Thin Solid Films 343/344 (1999)520

[158] Á. Nemcsics, I. Mojzes, L. Dobos; Microelectronics Reliability 39 (1999) 1505

[159] Á. Nemcsics, F. Riesz, L. Dobos; Phys. Stat. Sol. A 171 (1999) 283

[160] R. Kinder, Á. Nemcsics, R. Harman, F. Riesz, B. Pécz; Phys. Stat. Sol. (A) 175 (1999) 631

[161] Á. Nemcsics, K. Somogyi; Proc. of 3rd Int. Conf. On Advanced Semicond. Devices and Microsystems, Smolenice Castle, Slovakia 16-18 Oct. (2000), (Eds J. Osvald, S. Hascik, J. Kuzmik, J. Breza) 256

[162] Á. Nemcsics, L. Dobos, L. Dávid; Inorganic Materials 36 (2000) 969

[163] Á. Nemcsics, L. Dobos, F. Riesz; Fizika i Elektrotechnika 112 (2001)108

[164] Á. Nemcsics, M. Schuszter, L. Dobos, Gy. Ballai; Materials Science Engineering B 90 (2002) 67

[165] Á. Nemcsics, J. P. Makai; J. Phys, Condensed Matter 14 (2002) 13299

[166] Á. Nemcsics, J. P. Makai; Semiconductors 37 (2003) 657

[167] Á. Nemcsics, F. Riesz; Phys. Stat. Sol. C 0 (2003) 893

[168] F. M. Ross, J. Tersoff, R. M. Tromp; Phys. Rev. Lett. 80 (1998) 984

[169] F. M. Ross, R. M. Tromp, M. C. Renter; Science 286 (1999) 193

[170] S. Cereda, F. Montalenti; Phys. Rev. B 75 (2007) 195321

[171] F. Montalenti, P. Raiteri, D. B. Migas, H. von Känel, A. Rastelli, C. Manzano, G. Costanini, U. Denker, O. Schmidt, K. Korn, L. Miglio; Phys. Rev. B 93 (2004) 216102

[172] C.-H. Lam; J. Appl. Phys. 108 (2010) 064328

[173] G. Constantini, A. Rastelli, C. Manzano, R. Sonmuang, O. G. Schmidt, K. Kern, H. von Känel; Appl. Phys. Lett. 85 (2004) 5673

[174] Á. Nemcsics, E. Horváth, S. Nagy, L. M. Molnár, I. Mojzes, Zs. J. Horváth; Proc. of 7th Int. Conf. on Advanced Semiconductor Devices and Microsystems, Oct. 12-16, (2008) Smolenice, Slovakia 215

[175] Á. Nemcsics; in: Towards Intelligent Engineering and Information Technology (Studies in Computational Intellignce vol. 243; (Eds.: I. J. Rudas, J. Fodor, J. Kacprzyk) Springer Verlag, Berlin (2009) 557

[176] C. H. Hsu, M. T. Tang, H. Y. Lee, C. M. Huang, K. S. Liang, S. D. Lin, Z. C. Lin, C. P. Lee; Physica B 357 (2005) 6

[177] M. Kang, J-S. Lee, S-K. Sim, B. Min, K. Cho, H. Kim, M-Y. Sung, S. Kim, S. A. Song, M-S. Lee; Thin Solid Films 466 (2004) 265

[178] C. X. Wang, P. Liu, H. Cui, G. W. Yang; Appl. Phys. Lett. 87 (2005) 201913

[179] W. Wang, F. Bai; Appl. Phys. Lett. 87 (2005) 193109

[180] Y. Wang, J. Xu, R. M. Wang, D. P. Yu; Micron 35 (2004) 447

[181] R. S. Wagner: Whisker Technology; Wiley-Interscience, New York (1970)

[182] I. Iván, B. Pécz, S. Kökényesi, I. Mojzes, S. Misák, I. Szabó; Proc. of First Int. Workshop on Semiconductor Nanocrystals, SEMINANO2005, Sept. 10-12, 2005, Budapest, Hungary pp 23-26

[183] Ch. Heyn; PhD Thesis, Hamburg 1994

[184] J. Liu, Z. Wu, X. Mei, H. E. Ruda, K. L. Kavanagh

[185] M. C. Plante, R. R. LaPierre; J. Crystal Growth 310 (2008) 356

[186] B. A. Wacaser, K. Deppert, L. S. Karlsson, L. Samuelson, W. Seifert; J. Crystal Growth 287 (2006) 504

[187] K. Ikejiri, J. Noborisaka, S. Hara, J. Motohisa, T. Fukui; J. Crystal Growth 298 (2007) 616

[188] M. Bukala, M. Galicka, R. Buczko, P. Kacman; Acta Physica Polonica A 112 (2007) 425

[189] D. Leonard, M. Krisnamurthy, C. M. Reaves, S. P. Denbaas, and P. M. Petroff, Appl. Phys. Lett. 63 (1993) 3203

[190] N. Koguchi, S. Takahashi, and T. Chikyow, J. Cryst. Growth, 111 (1991) 688

[191] N. Koguchi, and K. Ishige, Jpn. J. Appl. Phys., 32, 2052 (1993)

[192] K. Watanabe, N. Koguchi, and Y. Gotoh, Jpn. J. Appl. Phys., 39, L79 (2000)

[193] T. Mano, T. Kuroda, S. Sanquinetti, T. Ochiai, T. Tateno, J. Kim, T. Noda, M. Kawabe, K. Sakoda, G. Kido, N. Koguchi, Nano Lett. 5 (2005) 425

[194] Ch. Heyn, A. Stemmann, A. Schramm, H. Welsch, W. Hansen, and Á. Nemcsics, Appl. Phys. Lett., 90, 203105 (2007)

[195] Á. Barna, B. Pécz, and G. Radnóczi, In: Handbook of Microscopy, 3 (1997) 751

[196] Á. Nemcsics, L. Tóth, L. Dobos, Ch. Heyn, A. Stemmann, A. Schramm, H. Welsch, W. Hansen; Superlattices and Microstructures 48 (2010) 351

[197] B. A. Joyce, and D. D. Vvedensky, In: Quantum Dots: Fundamentals, Applications, and Frontiers, Springer, Dordrecht, 1 (2005)

[198] G. Costanini, C. Manzano, R. Songmuang, O. G. Schmidt, and K. Kern, Appl. Phys. Lett., 82 (2003) 3194

[199] J. Marquez, L. Geelhaar, and K. Jacobi, Appl. Phys. Lett., 78 (2001) 2309

[200] G. A. Satunkin, J. Cryst. Growth, 255 (2003) 170

[201] C. Messmer, J. C. Bilello, J. Appl. Phys. 52 (1981) 4623

[202] Z.-Y. Zhou, N. Tian, Z.-Z. Huang, D.-J. Chen, S.-G. Sun, Faraday Discuss. 140 (2008) 81

[203] B. Z. Olshanetsky, V. I. Mashanov, Surf. Sci. 111 (1981) 414

[204] R. Nötzel, L. Däweritz, K. Ploog, Phys. Rev. B 46 (1992) 4736

[205] M. G. Lagally, D. E. Savage, M. C. Tringides, In: Reflection High-Energy Electron Diffraction and Reflection Electron Imaging of Surfaces, NATO ASI Series 188 (1988) 139

[206] Á. Nemcsics, Ch. Heyn, A. Stemmann, A. Schramm, H. Welsch, W. Hansen; Mat. Sci. Eng. B 165 (2009) 118

[207] E. Lendvay, T. Görög, V. Rakovics, J. Cryst. Growth 72 (1985) 616

[208] W. Braun: Applied RHEED; Springer Verlag (1999) Heidelberg

[209] T. Mano, K. Watanabe, S. Tsukamoto, H. Fujioka, M. Oshima, N. Koguchi; J. Cryst. Growth 209 (2000) 504

[210] Z. Gong, Z. C. Niu, S. S. Huang, Z. D. Fang, B. Q. Sun, J. B. Xia; Appl. Phys. Lett. 87 (2005) 093116

[211] B. L. Liang, Zh. M. Wang, J. H. Lee, K. Sablon, Yu. I. Mazur, G. J. Salamo; Appl. Phys. Lett. 89 (2006) 043113

[212] I. Mojzes, T. Sebestyén, P. B. Barna, G. Gergely, D. Szigethy, Thin Solid Films 61 (1979) 27

[213] G. B. Stringfellow, J. Cryst. Growth 27 (1974) 21

[214] M. Zinke-Allmang, L. C. Feldman, W. van Saarloos; Phys. Rev. Lett. 68 (1992) 2358

[215] G. Z. Pan, K. N. Tu; Appl. Phys. Lett. 68 (1996) 1654

[216] G. R. Carlow, M. Zinke-Allmang; Phys. Rev. Lett. 78 (1992) 4601

[217] A. Raab, G. Springholz; Appl. Phys. Lett. 77 (2000) 2991

[218] Á. Nemcsics, Ch. Heyn, A. Stemmann, A. Schramm, H. Welsch, W. Hansen; Mat. Sci. Eng. B 165 (2009) 118

[219] T. Mano, N. Koguchi; J. Cryst. Growth 278 (2005) 108

[220] J. S. Kim, N. Koguchi; Appl. Phys. Lett. 85 (2004) 5893

[221] Á. Nemcsics; J. Cryst. Growth 217 (2000) 223

[222] Á. Nemcsics, L. Tóth, L. Dobos, A. Stemmann; Microel. Reliab. 51 (2011) 927

[223] C. R. M. Wronski; British J. Appl. Phys. 18 (1967) 1731

[224] P. Buffat, J. P. Borel; Phys. Rev. A 13 (1969) 2287

[225] R. R. Couchman; Phil. Mag. A 40 (1979) 637

[226] M. Zhang, M. Y. Efremov, F. E. Schittekatte, A. Olson, A. T. Kwan, S. L. Lai, T. Wisleder, J. E. Greene, L. H. Allen; Phys. Rev. B 15 (2000) 10548

[227] M. B. Cortie, E. vd Lingen; Mat. Forum 26 (2002) 1

[228] S. Q. Sun, Y. Wang, B. K. Tay; J. Phys. Chem. B 106 (2002) 10701

[229] A. Saraei, M. A. Shandiz, S. Sanjabi, Z. H. Barber; J. Phys. Cond Matt. 19 (2007) 216216

[230] M. A. Asoro, J. Damiano, P. J. Ferreira; Microscopy Microanal. 15 (2009) 706

[231] C. Hock, S. Straßburg, S. H. Haberland, B. von Issendorff, A. Aguado, M. Schmidt; Phys. Rev. Lett. 2008;101:023401

[232] V. P. Skipov, V. P. Koverda, V. N. Skokov; Phys. Stat. Sol. A 66 (1981) 109

[233] A. Jiang, N. Awasthi, A. N. Kolmogorov, W. Setyawan, A. Borjesson, K. Bolton, A. R. Harutyunyan, S. Curtarolo; Phys. Rev. B 75 (2007) 205426

[234] J. Sun, S. L. Simon; Therochimica Acta 463 (2007) 32

[235] M. Wautelet, D. Beljonne, J. L. Brédas, J. Cornil, R. Lazzaroni, P. Lecére, M. Alexanre, P. Gillis, Y. Gossuin, R. Muller, A. Ouakssim, A. Roch, D. Duviver, J. Robert, R. Gouttebaron, M. Hecq, F. Monteverde: Nanotechnologie, Oldenbourg Verlag München, (2008)

[236] M. Schmidt, R. Kusche, B. von Issendorff, H. Haberland; Nature 393 (1998) 238

[237] G. A. Breaux, R. C. Benirschke, T. Sugai, B. S. Kinnear, M. F. Jarrold; Phys. Rev.Lett. 91 (2003) 215508

[238] S. Chacko, K. Joshi, D. G. Kanhere; Phys. Rev. Lett. 92 (2004) 135506

[239] Á. Nemcsics, A. Stemmann, J. Takács; Microelectronics Reliability (2011) on line available

[240] Y. Nabetani, T. Ishikawa, S. Noda, A. Sasaki, J. Appl. Phys. 76 (1994) 347

[241] K. Zhang, Ch. Heyn, W. Hansen, Appl. Phys. Lett. 76 (2000) 2229

[242] T. Mano, S. Tsukamoto, N. Koguchi, H. Fujioka, M. Oshima, N. Koguchi, J. Crystal Growth 227-228 (2001) 1069

[243] T. Kuroda, T. Mano, T. Ochiai, S. Sanguinetti K. Sakoda, G. Kido, N. Koguchi, Phys. Rev. B 72 (2005) 205301

[244] S. Hwang, Z. Nin, Z. Fang, H. Ni, Z. Gong, J. Xia, Appl. Phys. Lett. 89, 031921 (2006)

[245] Ch. Heyn, A. Stemmann, A. Schramm, H. Welsch, W. Hansen, Á. Nemcsics, Phys. Rev. B 76 (2007) 075317

[246] Ch. Heyn, D. Endler, K. Zhang, and W. Hansen, J. Crystal Growth 210 (2000) 421

[247] J. A. Venables, G. D. Spiller, and M. Hanbücken, Rep. Prog. Phys. 47 (1984) 399

[248] O. Dehaese, X. Wallart, and F. Mollot, Appl. Phys. Lett. 66 (1995) 52

[249] Phys. Rev. B. 66, 075307 (2002)

[250] Á. Nemcsics, Semicond. 39, 1352 (2005)

[251] T. Hanada, B. Koo, H. Totsuka, T. Yao, Phys. Rev. B 64 (2001) 165307

[252] D. W. Pashley, J. H. Neave, B. A. Joyce, Surf. Sci. 476 (2001) 35

[253] I. Mojzes, T. Sebestyén, P. B. Barna, G. Gergely, D. Szigethy, Thin Solid Films 27 (1979)

[254] T. Mano, K. Mitsuishi, Y. Nakayama, T. Noda, K. Sakoda; Appl. Surf. Sci. 254 (2008) 7770

[255] S. Sanguinetti, M. Abbarchi, A. Vinattieri, M. Zamfirescu, M. Gurioli, T. Mano, T. Kuroda, N. Koguchi; Phys. Rev. B 77 (2008) 125404

[256] K. Kuroda, T. Kuroda, K. Sakoda, K. Watanabe, N. Koguchi, G. Kido; Appl. Phys. Lett. 88 (2006) 124101

[257] J. S. Kim, M. S. Jeong, C. C. Byeon, D. K. Ko, J. Lee; Appl. Phys. Lett. 88 (2006) 241911

[258] Y. Yamagiwa, T. Mano, T. Kuroda, T. Tateno, K. Sakoda, G. Kido, N. Koguchi; Appl. Phys. Lett. 89 (2006) 113115

[259] K. Watanabe, S. Tsukamoto, Y. Gotoh, N. Koguchi; J. Crystal Growth 227 (2001) 1073

[260] R. Viswanatha, S. Sapra, T. Saha-Dasgupta, D. D. Sarma; Phys. Rev. B 72 (2005) 045333

[261] G. Bastard: Wave Mechanics Applied to Semiconductor Heterostructures, Les Éditions de Physique, Les Ulis (1990)

[262] Á. Nemcsics, J. Balázs, B. Pődör, J. Makai, A. Stemmann; Phys. Stat. Sol. C 8 (2011) 2826

[263] Á. Nemcsics, B. Pődör, J. Balázs, J. Makai, A. Stemmann; Ext. Abstr. of 19th Int. Symp. on Nanostructures: Physics and Technology, Ekaterinburg, Russia, June 20-25, (2011) 1

[264] P. Michler, A. Kiraz, C. Becher, W. V. Schoenfeld, P. M. Petroff, L. Zhang, E. Hu, and A. Imamoglu, Science 290 (2000) 2282

[265] O. Benson, C. Santori, M. Pelton, and Y. Yamamoto, Phys. Rev. Lett. 84 (2000) 2513

[266] D. Leonard, M. Krisnamurthy, C. M. Reaves, S. P. Denbaas, P. M. Petroff, Appl. Phys. Lett. 63 (1993) 3203

[267] V. Bressler-Hill, S. Varma, A. Lorke, B. Z. Nosho, P. M. Petroff, W. H. Weinberg, Phys. Rev. Lett. 74 (1995) 3209

[268] W. Yang, H. Lee, T. J. Johnson, P. C. Sercel, A. G. Norman, Phys. Rev. B 61 (2000) 2784

[269] O. Stier, M. Grundmann, D. Bimberg, Phys. Rev. B 59 (1999) 5688

[270] Ch. Heyn, A. Bolz, T. Maltezopoulos, R. L. Johnson, and W. Hansen, J. Crystal Growth 278 (2005) 46

[271] J. Tersoff, F. K. LeGones, Phys. Rev. Lett. 72 (1994) 3570

[272] T. Mano, K. Watanabe, S. Tsukamoto, H. Fujikoa, M. Oshima, N. Koguchi, Jpn. J. Appl. Phys. 38 (1999) L1009

[273] J. M. Lee, D. H. Kim, H. Hong, J. C. Woo, S. J. Park, J. Crystal Growth 212 (2000) 67

[274] T. Mano, T. Kuroda, K. Mitsuishi, M. Yamagiwa, X.-J. Guo, K. Furuya, K. Sakoda, N. Koguchi, J. Crystal Growth 301-302 (2007) 740

[275] T. Mano, T. Kuroda, M. Yamagiwa, G. Kido, K. Sakoda, and N. Koguchi, Appl. Phys. Lett. 89 (2006) 183102

[276] Ch. Heyn, A. Stemmann, T. Köppen, Ch. Strelow, T. Kipp, M. Grave, S. Mendach, W. Hansen; Appl. Phys. Lett. 94 (2009) 183113

[277] Zh. M. Wang, B. L. Liang, K. A. Sablon, and G. J. Salamo, Appl. Phys. Lett. 90 (2007) 113120

[278] Ch. Heyn, A. Stemmann, W. Hansen; Appl. Phys. Lett. 95 (2009) 173110

[279] Ch. Heyn, A. Stemmann, R. Eiselt, W. Hansen; J. Appl. Phys. 105 (2009) 054316

[280] Ch. Heyn, A. Stemmann, W. Hansen; J. Crystal Growth 311 (2009) 1839

[281] Ch. Heyn, Phys. Rev. B 83 (2011) 165302

[282] Ch. Heyn, A. Stemmann, T. Köppen, Ch. Strelow, T. Kipp, M. Grave, S. Mendach, and W. Hansen, Nanoscale Res. Lett. 5 (2010) 576

[283] Ch. Heyn, M. Klingbeil, Ch. Strelow, A. Stemmann, S. Mendach, and W. Hansen, Nanoscale Res. Lett. 5 (2010) 1633

[284] V. Polojärvi, A. Schramm, M. Guina, A. Stemmann, Ch. Heyn; Nanotechnology 22, 105603 (2011)

[285] A. Stemmann, Ch. Heyn, T. Köppen, T. Kipp, and W. Hansen, Appl. Phys. Lett. 93 (2008) 123108

[286] Á. Nemcsics, L. Tóth, L. Dobos, A. Stemmann, W. Hansen, Ch. Heyn; J. Crystal Growth (2011) on line available

# Closing remarks

This essay is an intermediate report on the results of an unfinished and ongoing research, parallel with an active long-term development. The fact, that the continuity of the work could not be interrupted explains the unfinished and perhaps fuzzy appearance of this report.

The most important part of this research is the development of the MBE droplet epitaxial technology, which will probably revolutionise the technology of semiconductor devices. In this field we are enganged in a first line research. It was imperative not to interrupt our research, which would have resulted in losing our pioneering position in this field.

As a parallel activity we worked on establishing the MBE technology in our country by laying the foundation a MBE research laboratory and creating the right technical and staff conditions for further research. This effort, no doubt, very often was hampered by the lack of required financial support.

The author of this report wishes to express his gratitude first of all to both directors, who have founded the Joint MBE Research Laboratory, professors István Bársony and Péter Turmezei for their unbroken effort in this task.

Further to this the author wishes to acknowledge the hard and cooperative work of colleagues and express his thanks for it.

At last but not at least I am thankful to my family for tolerating my hardpressed personality during this hard work.

*The author*

Budapest; September 2011